SYNTHESIS, CHARACTERIZATION, AND MODELING OF NEW MOLECULE-BASED MAGNETS

A Dissertation
Submitted to the Graduate Faculty
of the
North Dakota State University
of Agriculture and Applied Science

By

Christopher Samuel Olson

In Partial Fulfillment of the Requirements
for the Degree of
DOCTOR OF PHILOSOPHY

Major Department:
Materials and Nanotechnology

November 2015

Fargo, North Dakota

North Dakota State University
Graduate School

Title

Synthesis, Characterization, and Modeling of New Molecule-Based Magnets

By

Christopher Samuel Olson

The Supervisory Committee certifies that this ***disquisition*** complies with North Dakota State University's regulations and meets the accepted standards for the degree of

DOCTOR OF PHILOSOPHY

SUPERVISORY COMMITTEE:

Dr. Konstantin Pokhodnya
Chair

Prof. Svetlana Kilina

Prof. Erik Hobbie

Prof. Seth Rasmussen

Prof. Orven Swenson

Approved:

11/17/2015
Date

Erik K. Hobbie
Department Chair

ABSTRACT

The chemical bond and its role as a mediator of magnetic exchange interaction remains an important aspect in the study of magnetic insulators and semiconductors. The M[TCNE] (M = transition metal, TCNE = tetracyanoethylene) class of organic-based magnets has attracted considerable interest since $V^{II}[TCNE]_x$ (x ~ 2) exhibits one of the highest critical temperatures for its class – T_c ~ 400 K – in addition to highly spin-polarized conduction and valance bands (E_g ~ 0.5 eV), thus foreseeing potential spintronic application. The magneto-structural factors underlying this exceptional behavior remain elusive, however, due to the amorphous nature of the material. To address this, a novel synthetic route was utilized to produce new polycrystalline M[TCNE] solids (whose crystal structures have been resolved) with varying transition metal centers (Ni, Mn, Fe) and lattice dimensionality (2D-3D), exhibiting a wide range of T_c (40-170 K). Spectroscopic and magnetometric studies were performed and demonstrate that in 2D $[M^{II}(TCNE)(NCMe)_2]X$ structures (M = Ni, Mn, Fe; X = diamagnetic anion), strong ligand-to-metal transfer of electron density from the organic TCNE radical plays a significant role in the formation of magnetic exchange pathways, while single-ion anisotropy strongly influences the critical temperature and below-T_c spin disorder for magnets in this material class. Additionally, using quantum-computational modeling, magnetic spin-density transfer trends, spin-polarized electronic structures, and electronic exchange coupling constants have been identified and interpreted in terms of 3d-orbital filling and dimensionality of magnetic interaction. These findings offer new perspectives on the stabilization of magnetic order in M[TCNE] solids.

ACKNOWLEDGMENTS

The completion of this dissertation would have been impossible without the support, scientifically and otherwise, of numerous people. I would like to point out their contributions, in no particular order:

I must thank my family and close loved-ones for their patience during this long and selfish pursuit. Their steadfast support, understanding, and value of education paved the road leading to this work's completion. Without them, I would not have reached this stage.

My advisors, Konstantin Pokhodnya and Svetlana Kilina, have cumulatively provided countless hours of discussion and instruction on a vast array of scientific concepts and topics. I thank them for this invaluable time, and for what this time has imparted to me, greatly furthering my development as a thinking person and scientist. Beyond advising and guiding my work, I thank them for providing me opportunities to study, work, and share my research, both nationally and internationally. From the wonderful facilities at NDSU's CNSE where much of this research was carried out, to New Mexico, California, and Austria, these places and the experiences I had within them are indelible to me. That these experiences were also filled with interesting people, ideas, and meaningful activity makes having had them a nearly unbelievable privilege.

I want to thank Kendric Nelson for his friendship and excellent guidance during my initial time at CNSE as an undergraduate. I learned a considerable amount about being a thoughtful and careful researcher through our work together.

Thanks are in order to both Sergei Tretiak at Los Alamos National Laboratory and Vince Lordi at Lawrence Livermore National Laboratory for taking me in with their research groups. Although the work I performed with these groups does not appear in this dissertation, the

opportunity to “get outside the house” scientifically and contribute to new research projects for a few summers was invaluable for my scientific perspective, as well as my skill set.

Thanks to my full supervisory committee, whose names appear above, for taking time to consider this body of work, and for the helpful suggestions given to strengthen it in numerous ways.

Finally, I would like to acknowledge my co-contributors, whose work made much of this study possible. Thanks to: Kendrick Nelson for the synthesis of the precursor materials used in Chapter 4; Chris Heth for the synthesis of the materials studied in Chapter 5, as well as the entire Rasmussen lab for providing us with advice, material resources, and some much needed space on a solvent distillation bench; Peter Stephens and Saul Lapidus for XRD efforts, solving all crystal structures presented in this dissertation; Gregory Halder for additional XRD work and diffraction pattern indexing; as well as Shruba Gangopadhyay and Khang Hoang, both of whom contributed significantly to helping me overcome problems with complex magnetic simulation of the materials presented in Chapter 6.

DEDICATION

To my family, and Kristin.

TABLE OF CONTENTS

LIST OF TABLES

LIST OF FIGURES

1. INTRODUCTION AND MOTIVATION

1.1. Introduction

"Spintronics" is an emerging field of activity in materials science and engineering, and colloquially refers to electronic devices that exploit electron spin – a fundamental quantum mechanical property – in addition to or in place of charge [1-4]. Currently, successful examples of spintronic devices, such as the read-heads in magnetic hard disks, are based on ferromagnetic metal alloys. These devices are designed to exploit the giant magnetoresistance (GMR) and tunneling magnetoresistance (TMR) effects, which in turn describe the spin-dependent scattering of electrons within conductors and thin insulating barriers sandwiched between ferromagnetic layers. The resistance of these devices exhibits a strong dependence on the relative magnetic orientations of the metallic ferromagnetic layers, translating to the selective scattering or transmission of injected spin current based upon the spin polarization of its electrons. This behavior is illustrated in Fig. 1.1. The astounding success of commercialized devices utilizing this effect, particularly in the area of information storage, has made metallic spintronics a nearly ubiquitous aspect of modern life. The storage, transmission, or sensing of information based upon the quantum states of fundamental particles is also a logical conclusion to the aggressive and decades-long march to miniaturization of microelectronic device features, a phenomenon described by the so-called Moore's Law [5,6]. Due to the comparatively long lifetime of the spin state and ease of manipulation by modest fields, spin-based electronics may provide a significant leap in device efficiency, functionality, and scalability.

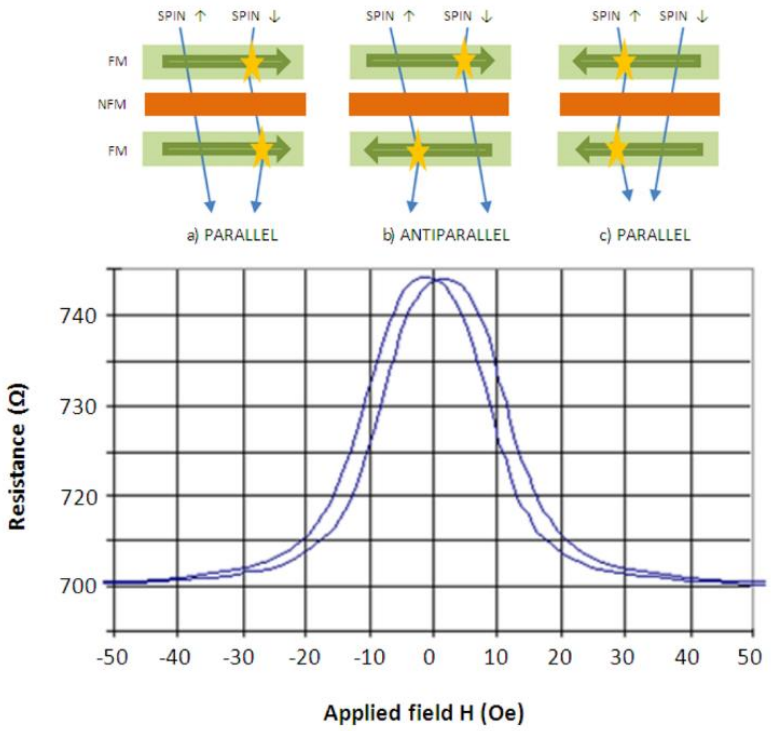

Figure 1.1. Spin-dependent scattering principle of GMR devices. Low resistance to "up" spin (a), High resistance to all spins (b), Low resistance to "down" spins (c) (top): GMR device resistance vs. applied magnetic field, corresponding to the illustrated device states (bottom). (Adapted from [7].)

These devices are expected to afford low-power and non-volatile data storage and processing while further enabling aggressive miniaturization of electronic device features. To exploit the full promise of spintronics technology, however, injection, transport, and detection of spin-polarized carriers in mature semiconductor-based materials and their established technologies is crucial. For example, the promise of silicon spintronics has attracted considerable attention, as devices based upon this concept would immediately benefit from the vast and well-developed body of knowledge surrounding the process engineering and manufacture of silicon-based transistors, and their ubiquity in modern computing platforms [8-10]. A spin-transistor based on silicon may also allow the full integration of data processing and storage functionalities into a single-chip device, vastly reducing computational platform size and energy consumption [11]. However, inefficient injection of spin-polarized current in semiconductors remains one of

the most important fundamental challenges for building semiconductor-based spintronic devices [12].

Recently, interest in molecule-based magnets (MBMs) was enhanced due to the potential use of these materials in novel devices that utilize electron spin to transmit or store data. Recent breakthroughs in the field of organic-based magnetism [13] have shown that molecule-based magnets could potentially overcome some significant issues related to spin polarized carrier injection (i.e. conductivity mismatch [14], interfacial segregation and/or oxidation [15], transition metal agglomeration and/or clustering [16], etc.) that have for many years thwarted efforts to create robust spin injectors using a fully inorganic approach. In addition, the use of molecule-based magnets for the transport of spin polarized current is potentially revolutionary because organic conductors and semiconductors can significantly limit spin dephasing due to their inherently weak spin-orbit coupling [17,18]. Thus, implementation of organic-based magnets as spin polarized current injectors presents an exciting opportunity for incorporating these novel materials into contemporary data processing and communication systems [19].

Numerous experiments on spin polarized current injection into organic semiconductors have been reported [20-26], and attempts to increase injection efficiency across a broad range of material systems remains the subject of ongoing and intense research effort. With respect to molcule-based magnetic materials and their potential technological utilization, the magnet $V[TCNE]_x$ ($x \sim 2$; TCNE = tetracyanoethylene, shown Fig. 1.2) exhibits a combination of properties that are crucial for a spin polarized current injector, especially in the quest for an all organic spintronic device. It magnetically orders above 400 K [27]; exhibits a semiconductor functionality with a DC electrical conductivity $\sigma(T)$ of 10^{-2} to 10^{-4} S/cm at room temperature [28,29]; can be deposited as a thin film on a variety of substrates via chemical vapor deposition

methodology [30,31]; and is reported to be a “half semiconductor” with fully spin-polarized valence and conduction bands [28].

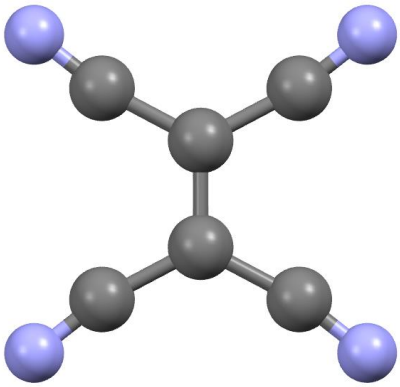

Figure 1.2. The TCNE organic molecule (C – grey; N – purple).

These unique characteristics have recently allowed the demonstration of both hybrid organic/inorganic [29] and all-organic [32] magnetic tunnel junctions (MTJs), as well as proof of spin polarized current injection from a $V[TCNE]_x$ emitter into a GaAs quantum well [33]. However, despite fascinating initial results, the properties of the molecular spin injectors based on the $V[TCNE]_x$ material system severely limit their practicality for use in commercial spintronic devices. For example, the maximum magnetoresistance change for a recently fabricated $V[TCNE]_x$ –based spin valve was found to be ~6% at 100 K, dropping rapidly upon both cooling and warming [29], ultimately limiting the device sensitivity and practical range of uses. Moreover, the lack of experimental data on the relationship between the structural features and the optoelectronic and magnetic properties of molecular magnets creates a challenge towards fabrication of materials with desirable and controllable functionalities. The compound $V[TCNE]_x$ is amorphous and its detailed chemical structure remains elusive after nearly 25 years of intense synthesis effort to crystallize the material. The details of its magnetic structure are likewise not well understood; although, magnetic ordering in this compound is proposed to occur

via strong antiferromagnetic exchange between the 3d transition metal and TCNE anion-radical unpaired spins. These states do not participate in chemical bonding, yet they exhibit a strong direct magnetic exchange. The relationship between this magnetic exchange pathway and the chemical bonding that holds M[TCNE] solids together is yet unclear.

1.2. Scope and Outline

The objective of this dissertation is to establish structure-property relationships within organic-based molecular magnets, targeting structural manipulation and chemical tuning of magnetic properties in a new class of M[TCNE] materials. These efforts are focused via a systematic experimental and computational study of the interplay between chemical composition and structural order, and the effect this interplay has on the ability of organic-based magnets to generate and preserve long-range magnetic ordering.

The two-dimensional layered molecule-based magnets of composition $[M^{II}(TCNE)(NCMe)_2]X$ (M = Ni, Mn, Fe; X = diamagnetic anion) are experimentally identified as a model system to study the impact of transition metal identity and interlayer spacing upon magnetic and spectroscopic behaviors. A new chemical route to obtain polycrystalline powders of the above compounds is leveraged, and several new crystal structures are revealed within this structural family. Correlations are sought between magnetic transition temperatures, obtained via extraction magnetometry, and spin-density transfer between transition metals and the spin-bearing TCNE anion, monitored via infrared and Raman vibrational spectroscopies. Finally, the impact of structural dimensionality on the electronic ground state and magnetic spin coupling strength is investigated computationally and theoretically, enabled by the newly resolved crystal structures of 2D plane and 3D networked Mn^{II}[TCNE]-based magnets.

The dissertation begins with a conceptual and theoretical overview of magnetism from the atomic perspective in Chapter 2. Mean-field models and modern interpretations of magnetic exchange are discussed. The latter half of Chapter 2 is devoted to a review of landmark materials and results in molecular magnetism, and concludes with the discussion of the synthetic route utilized to study the new materials presented in this work.

Chapter 3 begins with a conceptual and theoretical overview of the complementary techniques of Raman and infrared spectroscopy, as well as the related instrumentation. Magnetometry equipment and measurement principles, sample handling and preparation, and computational methodologies are discussed in the concluding portions of Chapter 3.

In Chapter 4, the newly synthesized $[M^{II}(TCNE)(NCMe)_2]SbF_6$ (M=Mn, Fe, Ni) material system is analyzed via a magnetometric and comprehensive vibrational study via Raman and infrared spectroscopies. A new MBM crystal structure and technique to quantify degree of ligand spin-density transfer and direction are presented.

In Chapter 5, the $[Mn^{II}(TCNE)(NCMe)_2]X$ (X=PF_6, AsF_6, SbF_6) material system is considered and the impact of anion size (interlayer distance) on magnetic interactions is discussed, and a thorough investigation of disordered spin dynamics in these materials presented.

In Chapter 6 a comprehensive hybrid density-functional modeling investigation of electronic and magnetic structures was performed using the XRD-resolved crystal structures for the structurally related 2D- and 3D- coordinated molecule-based magnets $[Mn^{II}(TCNE)(NCMe)_2]SbF_6$ and $[Mn^{II}(TCNE)_{1.5}](I_3)_{0.5}$, revealing new information about spin orbital hybridization and magnetic exchange pathways in M[TCNE] materials.

In Chapter 7, conlcusions based upon these results are summarized, and perspective about the implications for magnetic behavior in the broader M[TCNE] class is offered.

2. LITERATURE OVERVIEW

Molecule-based magnets (MBMs) are a class of materials for which the collective response behaviors of individual unpaired electrons – both electron-electron interaction and interactions with external fields – strongly influence the observed global material properties. While these features are common among all magnetic materials, MBMs in particular are set apart by the building-block nature of their construction, where spin-hosts combine to give rise to complex exchange interactions through the overlap of paramagnetic spins, inextricably linking the chemical bond, and all of its transformability, to the magnetic behavior. This feature leads to what is probably the most striking contrast to metallic magnets, whose "sea" of highly delocalized, nearly-free, and roughly independent electrons near the Fermi edge interact to give rise to magnetic phenomena. With this consideration, molecule-based magnets would then require a description of magnetic properties from the perspective of well-localized electronic states.

In this chapter, a theoretical background on the magnetism of the atom will be presented, with later focus on the description of electronic interactions responsible for the emergent magnetic phenomena within insulators. This chapter concludes with overview of some important molecule-based magnetic solids, with special attention given to exceptional TCNE-derived hybrid organometallic magnets, establishing a background and motivation for study of the materials presented in the later chapters of this work.

2.1. Theoretical Concepts in Magnetism

The magnetism of electron must be considered from a quantum mechanical perspective, since a classical material at thermal equilibrium, even in the presence of an externally applied

magnetic field, can exhibit no magnetic moment [34]. Within the quantum mechanical perspective, two principal quantities are responsible for the magnetism of an individual electron: the intrinsic "spin" of the electron, **S**, and the associated orbital angular momentum **L**. A third effect, the change in orbital moment as a response to an externally applied magnetic field, is also a consequence of the quantum nature of the electron and is observed for all classes of matter, even those where the total spin and orbital momentum are zero. The first two effects are responsible for the so-called paramagnetism of materials, and the latter for an effect called diamagnetism. The detailed nature of these effects is considered below.

A single electron in a multi-electron atom is subject to a number of effects inherent to its environment. An electronic Hamiltonian, which corresponds to the total energy of a quantum system Ψ through the relation $H_T|\Psi\rangle = E_T|\Psi\rangle$, contains the sum of dominant effects (formulated as mathematical operators) influencing the particle's quantum electronic states and may be defined simply as

$$H_{\boldsymbol{T}} = H_{\boldsymbol{e-N}} + H_{\boldsymbol{e-e}} + H_{\boldsymbol{dia}} + H_{\boldsymbol{para}} \qquad \text{(eq. 2.1)}$$

The first and second term correspond to the influence of the electron in a spherical potential surrounding the nucleus of the atom, and the Columbic repulsion of the electrons with themselves, respectively. The following terms in order represent the diamagnetic and paramagnetic contributions to total energy. In the absence of multi-center electron-electron correlations giving rise to collective alignment of spins, the magnetic responses of materials are only observable in the presence of an externally applied magnetic field B. The full mathematical Hamiltonian for an atom in an applied external magnetic field can then be defined, with terms in the order of the above:

$$H_{\boldsymbol{T}} = \sum_i \left(\frac{\boldsymbol{p}_i^2}{2m} - \mathbf{A}(\mathbf{r}_\mathrm{i})\right) - \sum_{i<j}\left(\frac{Z_i e^2}{r_{ij}}\right) + \frac{e^2}{8mc^2}\sum_{\boldsymbol{i}}(\mathbf{B}\times\mathbf{r}_\mathrm{i})^2 + \mu_B(\mathbf{L} + g_0\mathbf{S})\cdot\mathbf{B} \qquad \text{(eq. 2.2)}$$

with $\mathbf{B} = \nabla \times \mathbf{A}$ and $\mathbf{A} = -\frac{1}{2}\mathbf{r} \times \mathbf{B}$. The vector quantities $\mathbf{p}_i$, **A**, **B**, **L**, **S**, and $\mathbf{r}_i$ and represent the momentum operator, vector potential, external applied magnetic field vector, angular momentum vector, spin vector, and electron-nuclear distance, respectively. The scalar values e, r_{ij}, m, c, and μ_B and g_0 are the fundamental charge of the electron, electron-electron distance, mass of the electron, speed of light, Bohr magneton, and electronic g-factor, respectively. Scalar forms of the magnetic field, angular momentum vector, and spin vector are given by B, L, and S respectively. Indices i,j run over the total number of electrons present in the system.

In the absence of an external magnetic field vector **B**, Hamiltonian reduces to the energy description of an electron in the central field approximation with inter-electronic repulsion H_0 (i.e. $H_{\boldsymbol{T}} = H_0 + \Delta H_{\mathbf{B}}$ with $\Delta H_{\mathbf{B}} = 0$). Therefore, aside from a small vector potential correction of the electronic kinetic energy, the leading terms may be neglected when considering the response of the system to the magnetic field, and the latter terms $\Delta H_{\mathbf{B}}$ viewed as the dominant perturbations to the total energy of the system. Following second-order perturbation theory, these energy shifts may be approximated for a quantum system in some electronic state $|n\rangle$ by

$$\Delta E_n = \langle n|\Delta H_{\mathbf{B}}|n\rangle + \sum_{n \neq n'} \frac{|\langle n|\Delta H_{\mathbf{B}}|n'\rangle|^2}{E_n - E_{n'}} \qquad \text{(eq. 2.3)}$$

Following this definition and inserting the field-dependent terms from the total Hamiltonian ($\Delta H_{\mathbf{B}}$) one arrives at [35]

$$\Delta E_n = \mu_B \mathbf{B} \cdot \langle n|\mathbf{L} + g_0\mathbf{S}|n\rangle + \sum_{n \neq n'} \frac{\left|\langle n|\mu_B \mathbf{B} \cdot (\mathbf{L} + g_0\mathbf{S})|n'\rangle\right|^2}{E_n - E_{n'}} + \frac{e^2}{12mc^2} B^2 \langle n| \sum_i {r_i}^2 |n\rangle \qquad \text{(eq. 2.4)}$$

The above equation forms the theoretical groundwork enabling further analysis of the diamagnetic and paramagnetic responses of matter in an applied magnetic field from the quantum mechanical perspective of the total system energy.

2.1.1. Diamagnetism

At absolute zero, the magnetization density of a material is given by

$$M(B) = -\frac{1}{V}\frac{\partial E_0(B)}{\partial B} \quad \text{(eq 2.5)}$$

Where V is the total volume of the material and $E_0(B)$ is the ground-state energy in the external magnetic field B. As noted previously, the paramagnetic response is caused by unpaired electron spin, while diamagnetism is a property inherent to all matter. In the case where orbital and spin moments are zero, as happens in the case where all orbitals are doubly-filled by electrons, the quantum ground electronic state of the system $|0\rangle$ when acted upon by the spin and orbital moment operators in the Hamiltonian will yield $\mathbf{L}|0\rangle = \mathbf{S}|0\rangle = 0$. Thus, the change in energy for the atom in the magnetic field will become

$$\Delta E_0 = \frac{e^2}{12mc^2} B^2 \langle 0| \sum_i r_i{}^2 |0\rangle \quad \text{(eq. 2.6)}$$

By defining the magnetic susceptibility as the change in magnetization as a function of applied field, $\chi = \frac{\partial M}{\partial B}$, using the definition above one arrives at the magnetic susceptibility of N atoms in a solid, given by

$$\chi_D = -\frac{N}{V}\frac{e^2}{6mc^2} \langle 0| \sum_i r_i{}^2 |0\rangle \quad \text{(eq. 2.7)}$$

This result is known as the Larmour diamagnetic susceptibility and is present in all forms of matter. The diamagnetic susceptibility is negative and temperature independent, and must be corrected for when analyzing susceptometry measurements, particularly the $\chi T (T \sim 300\ K)$ form, since the measured magnetic susceptibility is a sum of paramagnetic and diamagnetic responses, both multiplied by the factor of the temperature. Typically, this susceptibility is very small (on the order of ~10^{-6} emu/mol), but can become appreciable for chemically complex

species with a large number of atoms. Table 2.1 provides some values for atomic species and chemical bonds found in this work [36].

Table 2.1. Diamagnetic constants for numerous atoms and structures.

Species	χ_D (10^{-6} emu/mol)	Species	χ_D (10^{-6} emu/mol)	Species	χ_D (10^{-6} emu/mol)
V^{II}	-15.0	H	-2.93	F^-	-9.1
Mn^{II}	-14.0	C	-6.00	I^-	-50.6
Fe^{II}	-13.0	N	-4.61	C=C	+5.5 [a]
Fe^{III}	-10.0	P^{5+}	-1.0	-C=N	+0.8 [a]
Co^{II}	-12.0	As^{5+}	-43.0	CN^-	-13.0
Ni^{II}	-12.0	Sb^{5+}	-14.0	CH_3CN	~ -27.8

[a] Diamagnetic susceptibility of chemical bonds in coordination complexes is commonly positive, acting as a correction to total diamagnetic susceptibility tallied from the sum of the individual atomic species. Thus, the total χ_D of a complex is the sum of the atomic contributions, plus the corrections from the chemical bonds present. For example, $\Sigma\chi_D$ for acetylene (H-C=C-H) gives -17.86 emu/mol if counting *only* atomic contributions. The value becomes -12.36 emu/mol upon correcting for the χ_D of the C=C bond, and is very close to the literature value of -12.5 emu/mol [37].

2.1.2. Paramagnetism

The preceding example considers the situation where a multi-electron atom contains a series of electronic levels, all fully (dually) populated by electrons. In the case where unpaired electrons are present, the paramagnetic response will fully dominate the magnetic behavior when an external field is applied. In order to properly discuss the paramagnetism arising from these cases, a discussion of the ground state properties of multi-electron systems with unpaired spins is instructive.

The quantum states of a multi-electron atom or ion, based on the solution of the Schrodinger equation for the hydrogen atom [38], are labeled as n, l, m_l and correspond to a wave function $\psi_i(r,\theta,\phi)$ possessing a spatial distribution dependent upon those quantum numbers. Here, n is the principal quantum number, l is the orbital quantum number, and m_l is typically denoted as the magnetic quantum number. For a given n shell, the orbital quantum

number l is restricted to values between 0 and n-1. Convention states that the designation for the values l = 0, 1, 2, 3, ... , are the letters *s, p, d, f,* ... These correspond to the atomic orbitals familiar from chemistry, and are based on the hydrogenic wavefunction solutions mentioned above.

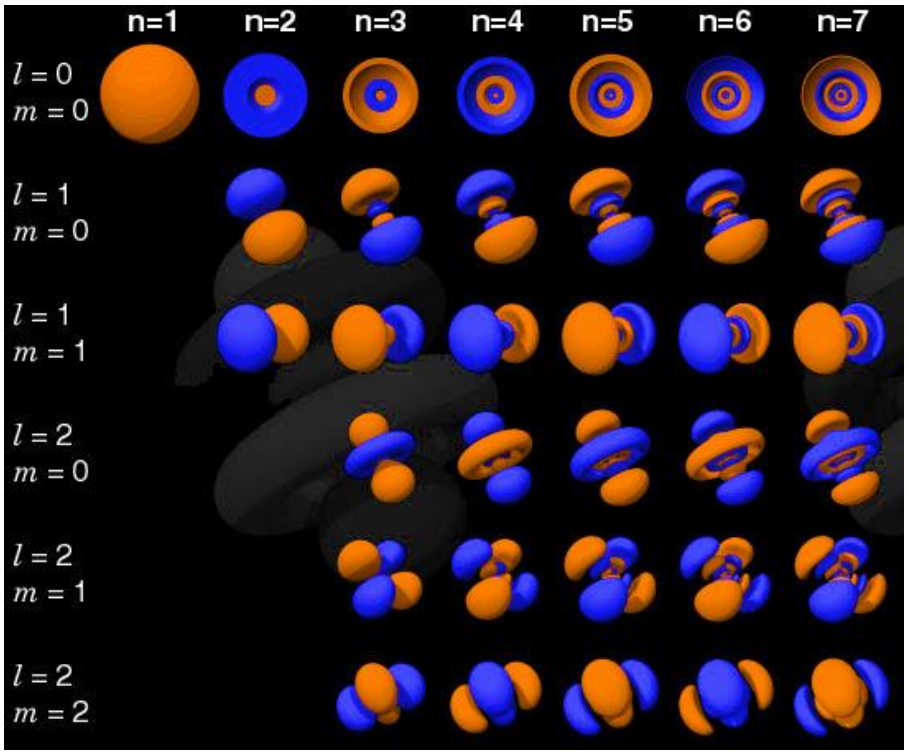

Figure 2.1. Visualization of orbital wavefunctions $\psi_i(r,\theta,\phi)$ with various n, l, and m.

For a given value of l there are $2l + 1$ values possible for the z-projection l_z (l, l-1, l-2, … -l). Further, for each value of l_z there are two spin values possible for m_s of +1/2 and -1/2, corresponding to the possible electron spin orientations for each projection of l. Thus, for a number of n electrons in a shell, there are $0 < n < 2(2l + 1)$ electronic configurations possible. Put another way, the total degeneracy of electronic states a shell is the upper bound on n, or $2(2l + 1)$ since there are two spin orientations for each of the $2l$+1 states of l_z. In practice, this degeneracy is lifted by the Coulomb interactions between electrons, and more rarely spin-orbit coupling, when this effect is a substantial contributor to the total energy in the ground state. Such

is the case for the lanthanide series, due to the well-shielded 4*f* electrons [35]. Nevertheless, after the lifting of the degeneracy, the ground state of the partially filled shell of ions can be described empirically by the so-called Hund's rules. They are stated as follows [34,35,39]

- *Russel-Saunders Coupling*: Given the total spin and angular momentum quantum numbers as the summations $S = \sum m_s$ and $L = \sum l_z$ respectively, the total electronic angular momentum for a partially filled shell is defined as the sum $J = L + S$. It is noted that for a totally filled shell, $J = L = S = 0$, and thus these quantum numbers are able to describe both the open and closed shell cases of atomic electron configurations.
- *Hund's First Rule*: Of the multiple states possible by placing *n* electrons into 2(2*l* + 1) levels of a partially filled shell, the states of minimum energy are those that both maximize the total spin S and remain consistent with the exclusion principle. This condition is met by filling the first $n = 2l + 1$ states with one electron each, so that none of the states is dually occupied and total spin is maximized to the value $S = l + ½$. Upon subsequent filling with *n* electrons, the total spin decreases to $S = l + ½ - 1/n$ by pairing off previously singly-occupied states until the value reaches $S = 0$.
- *Hund's Second Rule*: The total value of the orbital angular momentum L of low-lying states will be maximized in a way that is consistent with Hund's First Rule and the exclusion principle. The electrons fill the empty states in such a way that the first electron placed maximizes $L = \Sigma l_z$. The subsequent electron will fill the next available orbital following the first rule and will give $L = l + (l - 1) = 2l - 1$, and so on. Upon being half-filled with electrons, all values of l_z will have been occupied and $L = |\Sigma\ l_z| = 0$, the precise condition for maximizing S. Further filling begins pairing off the singly occupied

orbitals one-by-one, yielding the same L values given through the initial half-filling procedure.

- *Hund's Third Rule*: Of the $(2L+1)(2S+1)$ number of states possible by the prescription of the first two rules, they may be characterized by the rules of angular momentum addition $J = L \pm S$ according to the occupancy of the states by *n* electrons. For up to a half-filled shell, the coupling rule (in terms of *n*) is written $n \leq 2l+1,\ J = |L-S|$ and past half-filling, the coupling rule becomes $n \geq 2l+1,\ J = L+S$. This rule arises predominantly from the spin-orbit coupling λ where for less than half-filled shells, λ is a positive value, preferring a minimum J, and past half-filling λ becomes negative, maximizing J. In general, Hund's Third Rule applies only in the case of single ions or in materials where partially filled shells are well shielded from external potentials, such as a ligand or crystal-fields. This case is satisfied in practice for those 4*f* orbitals whose orbital filling results in non-zero L, but does not hold for the 3d electrons. For many purposes, the "good" quantum number for 3d-containing coordination materials is in fact S instead of J. The assumption that the L term is nearly zero for transition metal complexes is known as the quenching of orbital momentum, which is related to the crystal-field effects on the ion and is experimentally observed from high-field studies. For generality, in the following J will be the quantum number used unless otherwise specified.

With the practical rules describing the partial filling of electronic states complete, Table 2.2 illustrates the application of these rules for the progressive orbital filling of the $l = 2$ case, which is of utmost importance in the study of magnetism. These states are those of the 3d electrons, belonging to the transition metal series. The last column of the table displays the spectroscopic

naming convention of each multiplet ground state, encoded by the symbol ${}^{2S+1}X_J$ where X = S P D F … according to the assignment L = 0 1 2 3 … and so on.

Table 2.2. Ground states of *d* orbtials, following Hund's rules. (Adapted from [35].)

***d*-orbitals (l = 2)**										
n	l_z **= 2**	**1**	**0**	**-1**	**-2**	***S***	$L = \lvert\Sigma\, l_z\rvert$	***J***		**Term Symbol**
1	↓					½	2	3/2	$J = \lvert L-S\rvert$	${}^2D_{3/2}$
2	↓	↓				1	3	2		${}^3F_2$
3	↓	↓	↓			3/2	3	3/2		${}^4F_{3/2}$
4	↓	↓	↓	↓		2	2	0		${}^5D_0$
5	↓	↓	↓	↓	↓	5/2	0	5/2	J = 5/2	${}^6S_{5/2}$
6	↑↓	↑	↑	↑	↑	2	2	4	$J = L+S$	${}^5D_4$
7	↑↓	↑↓	↑	↑	↑	3/2	3	9/2		${}^4F_{9/2}$
8	↑↓	↑↓	↑↓	↑	↑	1	3	4		${}^3F_4$
9	↑↓	↑↓	↑↓	↑↓	↑	½	2	5/2		${}^2D_{5/2}$
10	↑↓	↑↓	↑↓	↑↓	↑↓	0	0	0	J = 0	${}^1S_0$

If an atom contains a partially filled shell, as discussed and illustrated above, the Hamiltonian terms containing **L** and **S** will in general be non-zero and the H_{para} terms will become contributors to the total system energy. There are two cases to consider. The first is the situation where the angular and spin contributions L and S are non-zero, but their sum according to Hund's Third Rule gives $J = 0$ (such as the ${}^5D_0$ multiplet, from Table 2.2). In the special case where the shell is one electron from being half-filled, the second-order contributions to the energy will survive [35] and this configuration in a magnetic field will possess energy

$$\Delta E_n = \sum_{n\neq n'} \frac{\left|\langle n|\mu_B \mathbf{B}\cdot(\mathbf{L}+g_0\mathbf{S})|n\rangle\right|^2}{E_n - E_{n'}} + \frac{e^2}{12mc^2} B^2 \langle n|\sum_i r_i{}^2\,|n\rangle \qquad \text{(eq. 2.8)}$$

and following again

$$\chi = -\frac{N}{V}\frac{\partial^2 E_0}{\partial B^2} \qquad \text{(eq. 2.9)}$$

the susceptibility of an N-atom ensemble with volume V can be expressed by

$$\chi = -\frac{N}{V}\left[\frac{e^2}{6mc^2}\langle n|\sum_i {r_i}^2|n\rangle - 2{\mu_B}^2\sum_n \frac{\left|\langle 0|\mu_B(\mathbf{L}+g_0\mathbf{S})|n\rangle\right|^2}{E_n - E_0}\right] \qquad \text{(eq. 2.10)}$$

The above shows two dominant terms, the first of which is the previously derived Larmor diamagnetism. The second term is known as the Van Vleck paramagnetism, and has opposite sign of the diamagnetic term, i.e. favors spin moment alignment with the external field. This effect is approximately the same magnitude as the diamagnetic contribution (~10^{-6} emu/mol) for materials of 3d elements.

By far the most important and most common case however is for the nonzero total electronic momentum, or $J \neq 0$ condition. For this case, the leading term of the energy shift will dominate in a way such that all other energy terms may be considered effectively zero. This gives

$$\Delta E_{0,\alpha'} = \sum_{\alpha'}^{2J+1} \mu_B \mathbf{B} \cdot \langle 0, \alpha|\mathbf{L} + g_0\mathbf{S}|0, \alpha'\rangle \qquad \text{(eq. 2.11)}$$

where a change of basis and sum over the $2J+1$ degenerate $J \neq 0$ ground state with $\alpha = 1, \ldots, (2J+1)$ is needed. The $\langle 0, \alpha|\mathbf{L} + g_0\mathbf{S}|0, \alpha'\rangle$ terms must be diagonalized with an appropriate basis to properly solve for the energy shifts. While this procedure is rather involved, it can be stated that the basis that achieves this procedure is the $|JLS, J_z\rangle$ one, where the familiar quantum numbers JLS describe the system in the quantum ground state. Following again [35] it can be written (with $J'_z,\ J_z = -J, \ldots, J$)

$$\langle JLS, J_z|\mathbf{L} + g_0\mathbf{S}|JLS, J'_z\rangle = \langle JLS, J_z|g(JLS)\mathbf{J}|JLS, J'_z\rangle \qquad \text{(eq. 2.12)}$$

Or simply

$$\mathbf{L} + g_0\mathbf{S} = g(JLS)\mathbf{J} \qquad \text{(eq. 2.13)}$$

with

$$g(JLS) = \frac{3}{2} + \frac{1}{2}\left[\frac{S(S+1) - L(L+1)}{J(J+1)}\right] \qquad \text{(eq. 2.14)}$$

The above quantity is known as the Lande g-factor, and describes the degeneracy of the electronic states as lifted in a magnetic field. Finally, the energy shift of a partially filled shell in a magnetic field can be written

$$\Delta E \propto \mu_B \langle JLS, J_z | g(JLS)\mathbf{J} | JLS, J'_z \rangle \cdot \mathbf{B} \propto H_{para}^{J\neq 0} \quad \text{(eq. 2.15)}$$

$$H_{para}^{J\neq 0} = g(JLS)\mu_B \mathbf{J} \cdot \mathbf{B} = -\boldsymbol{\mu}_{JLS} \cdot \mathbf{B} \quad \text{(eq. 2.16)}$$

which has an obvious classical analogy to the energy shift of a magnetic dipole vector $\boldsymbol{\mu}$ in a uniform external field $\mathbf{B}$. In this instance, however, the "dipole" moment $\boldsymbol{\mu}_{JLS} = -g(JLS)\mu_B \mathbf{J}$ represents the collective response of the partially filled $2J+1$ electronic levels of a paramagnet, governed by a spin Hamiltonian $H_{para}^{J\neq 0}$.

2.1.3. The Brillouin Function

The important result above is only valid when the degenerate $2J+1$ electronic levels are lifted in a field and energetically separated by a factor that is large relative to $k_B T$. This is in principle achieved for moderate fields, since the $2J+1$ J_z levels are separated in energy by $g(JLS)\mu_B B$, an important phenomenon known as Zeeman splitting. However, as the field approaches zero, the Zeeman splitting energies will eventually become small relative to $k_B T$. In this limit, a statistical mechanics approach is needed to formulate the magnetization of the degenerate or nearly degenerate ground state. For the following analysis, scalar forms of field and magnetic response are used (assuming a field in the z-direction and isotropic response within the material, so that only one component need be considered).

If the assumption is made that only the lowest $2J+1$ states are thermally populated, the thermodynamic free energy F can be written in terms of the magnetic field B by

$$e^{-\beta F} = \sum_{J_z=-J}^{J} e^{-\beta\gamma B J_z} = \frac{e^{\beta\gamma B\left(J+\frac{1}{2}\right)} - e^{-\beta\gamma B\left(J+\frac{1}{2}\right)}}{e^{-\beta\gamma B/2} - e^{\beta\gamma B/2}} \quad \text{(eq. 2.17)}$$

With $\gamma = g(JLS)\mu_B$ and $\beta = \frac{1}{k_B T}$. Relating the magnetization of *N* atoms in the volume *V* to the free energy is possible through

$$M = -\frac{N}{V}\frac{\partial F}{\partial B} = \frac{N}{V}\gamma J \Omega_J(\gamma \beta JB) \qquad \text{(eq. 2.18)}$$

with

$$\Omega_J(x) = \frac{2J+1}{2J}\coth\left(\frac{2J+1}{2J}x\right) - \frac{1}{2J}\coth\left(\frac{1}{2J}x\right) \quad \gamma\beta JB \to x \qquad \text{(eq. 2.19)}$$

$\Omega_J(x)$ is the well-known Brillouin function, and describes the alignment tendencies of isolated moments subjected to thermal agitation and external magnetic field. Fig. 2.2 [40] illustrates the paramagnetic saturation for various *d* and *f* series ions, possessing different quantum numbers *S*, fit to this function. The measurement of saturation moment and fitting to the Brillouin function is particularly useful to extract information about the spin ground state of materials, or assess material quality, as the saturation value will be very sensitive to magnetic impurities.

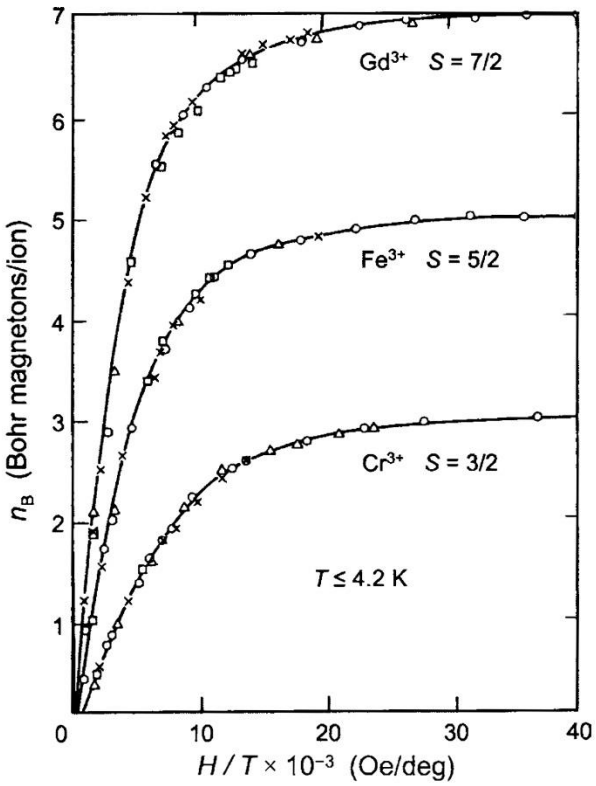

Figure 2.2. Saturation magnetization of various *d* and *f* series ions, fit to eq. 2.19. (Adapted from [40]).

2.1.4. Curie Law

It can be noted that the low temperature and very high field limit, as illustrated above, is typically needed to achieve full magnetic saturation; i.e., all spin states described by J (or S in the case where this is the "good" quantum number), possessing maximum alignment with the external magnetic field. However, the relationship $g\mu_B B/k_B T$, which is the fraction of energy supplied to the system by the external field to the thermal energy, usually satisfies in practice $g\mu_B B/k_B T \ll 1$. For example, $g\mu_B B/k_B \sim 1$ Kelvin even with the relatively large field magnitude B of 1 Tesla (10^4 Oerstead) [35]. In the limit $g\mu_B B \ll k_B T$ the Brillouin function will reduce to $\Omega_J(x) \sim (J+1)x/3J$ and finally the paramagnetic susceptibility in this limit can be written

$$\chi_{Curie} = \frac{\partial M}{\partial B} = \frac{\partial}{\partial B}\left[\frac{N}{V}\gamma J \Omega_J(x)\right] = \frac{N}{V}\frac{(g\mu_B)^2}{3}\frac{J(J+1)}{k_B T} = \frac{C}{T} \qquad \text{(eq. 2.20)}$$

This relation is known as the Curie Law for paramagnetic spins. The Curie constant C is related to the system under study, principally affected by the spin quantum numbers. At room temperature, the paramagnetic susceptibility of unpaired spins typically dwarfs the diamagnetic susceptibility from fully filled shells, with $\chi_{Curie}/\chi_D \sim 500$ [35].

2.1.5. Curie-Weiss Law

The previous discussion illustrates from first-principles the behavior of isolated quantum spins, in the context of ions, subjected to external fields and temperature. These results were expressed through the groundbreaking model of Brillouin, which provides a phenomenological basis for the Curie law. It was shown through derivation of magnetic susceptibilities that exposure of isolated spin systems to an external magnetic field induces an order upon these spins, and that this order is rapidly defeated by thermal agitation, even when the applied field is strong. However, a truly magnetic material will exhibit a *spontaneous* ordering of spins, overcoming thermal fluctuations, persisting in the absence of an external field. The onset of this spontaneous moment is not contained in or described by the previous models as derived. A correction to the Curie law in the form of an "exchange field", which supplements the externally applied one, was first introduced by Weiss [41] to explain the persistence of a magnetic order in zero field. This is done by writing the magnetic field as a sum of the external field and an internal magnetization, possessing some field constant ϑ, as $B_{eff} = B + \vartheta M$ and recalling the magnetization of a paramagnet $M = \frac{N}{V}\gamma J \Omega_J(\gamma \beta J B)$ with the substitution $B \rightarrow B_{eff}$, which then becomes $M' = \frac{N}{V}\gamma J \Omega_J(\gamma \beta J(B + \vartheta M))$. It is easy to see that in the case where the external

applied field $B = 0$ a magnetization persists, as sought. To determine the magnetic susceptibility of a material as before, a simple chain rule is used

$$\chi = \frac{\partial M\prime}{\partial B} = \frac{\partial M\prime}{\partial B_{eff}}\frac{\partial B_{eff}}{\partial B} = \frac{C}{T}\left(1 + \vartheta\frac{\partial M}{\partial B}\right) = \frac{C}{T}(1 + \vartheta\chi) \qquad \text{(eq. 2.21)}$$

Solving this relationship for χ,

$$\chi_{FM} = \frac{C}{T - \vartheta C} = \frac{C}{T - \theta_C} \qquad \text{(eq. 2.22)}$$

This relationship is known as the Curie-Weiss law for ferromagnets, which is a material whose spins all align in the same direction. This relation varies from the Curie law by the Weiss coefficient θ_C having units of temperature. An analogous relationship can be derived for materials where two spin sub-lattices with total spin population *n* are present, each possessing *n/2* spins "up" and *n/2* spins "down", otherwise known as "antiferromagnets"

$$\chi_{AFM} = \frac{C}{T - (-\vartheta)C} = \frac{C}{T + \theta_N} \qquad \text{(eq. 2.23)}$$

In this case, θ_N is the so-called Neel coefficient, which likewise carries units of temperature. The sign of the exchange field then describes the spatial relationship of the spins within a material: while $\vartheta > 0$ is reflected in systems where all spins align in parallel, $\vartheta < 0$ is found for systems whose spins align antiparallel to one another. The relationship collapses to the ideal paramagnetic Curie law when $\vartheta = 0$. Thus, upon measurement of an unknown magnetic material, one may plot the inverse susceptibility $\chi^{-1}(T) \sim T \pm \theta$ against temperature and linearly extrapolate in the paramagnetic limit to the temperature intercept. This is shown schematically in Fig. 2.3

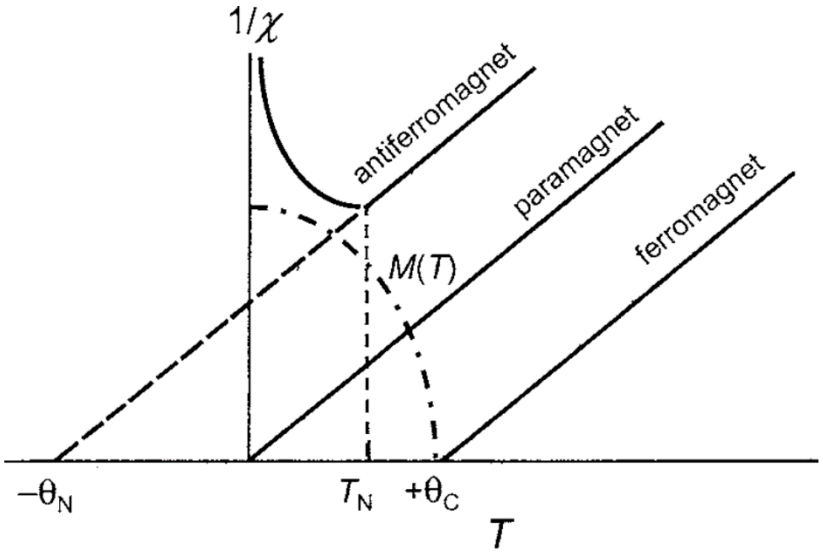

Figure 2.3. Inverse susceptibility $1/\chi(T)$ plotted to reveal Curie or Neel constants from antiferromagnets and ferromagnets, respectively. (Adapted from [40].)

The sign of the coefficient θ then gives the type of interaction within the system below the magnetic transition. Additionally, using the standard Curie law well above the critical ordering temperature T_c one may plot χT $(T \sim 5T_c) \propto C \propto J(J+1)$ to extract information about the spin composition through the Curie constant. The Curie law and the related Curie Wiess law are landmark relationships in the study of magnetism and magnetic materials, and find wide use in characterization due to their simplicity and ease of use.

2.1.6. Exchange Interaction of Electrons: Magnetic Coupling

The exchange field of Weiss and the formulation of the Curie-Weiss law represents the first mean-field approach to describing spontaneous magnetic behavior. However, the nature of the exchange field is not explained, as it is simply presumed to exist in the absence of an external field. An explanation of the exchange field, which relies on the quantum-mechanical nature of electronic orbitals and the competing interactions electrons will experience through the chemical bond, was given by Heisenberg [42]. Instead of collectively averaging the effects of all spins, as

is done in a mean-field context, the Heisenberg exchange Hamiltonian considers the energies of two adjacent and localized spins at sites *i, j* as a function of their relative orientation to one another. The form of the Hamiltonian is

$$H_{\boldsymbol{H}} = -2\sum_{i<j} \mathrm{J}_{ij}\mathbf{S}_i \cdot \mathbf{S}_j \qquad \text{(eq. 2.24)}$$

where J_{ij} is the Heisenberg exchange constant. In a similar fashion to the Weiss exchange field, it is noted that the sign of the exchange constant will govern the relative orientation of the electrons: $\mathrm{J}_{ij} > 0$ will cause electrons to align parallel to one another (ferromagnetic interaction) and $\mathrm{J}_{ij} < 0$ will lead to anti-parallel alignment (anti-ferromagnetic interaction). The orbital wave functions discussed earlier provide a means to discuss the interactions necessary to elucidate the quantum effects leading to a spin-ordered state, described by the exchange constant. A toy model, which is in essence two one-electron atoms in proximity (or one H_2 molecule), can be used to extract these details. The Hamiltonian describing the electron-electron repulsion and electron-nuclear attraction for each of the one-electron atoms is given below.

$$H_{\mathbf{0}} = \frac{p_a^2}{2m} + \frac{p_b^2}{2m} - \frac{Z_a e^2}{r_{a1}} - \frac{Z_b e^2}{r_{b2}} \qquad \text{(eq. 2.25)}$$

The atoms are labeled a and b, while the corresponding electrons from those atoms are listed 1 and 2, respectively. Z_n, r_{ni}, p_a^2, e and m are the nuclear charge on the nth atom, the nuclear-electron distance between the nth atom and its ith electron, the quantum momentum operator, fundamental electrical charge, and electron mass, respectively. This configuration is shown in Fig. 2.4 [40]. In terms of the orbital wavefunctions, two solutions to the above Hamiltonian can

be considered: a localized one where the electrons orbit their respective nuclei, $\psi_L = \psi_a(1)\psi_b(2)$, or an exchanged one, where the atoms swap electrons, $\psi_{EX} = \psi_a(2)\psi_b(1)$

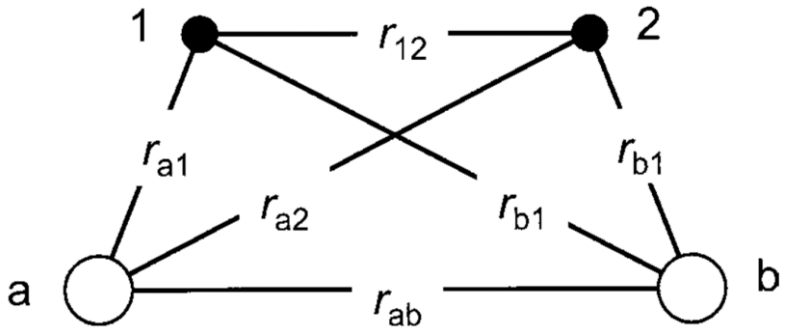

Figure 2.4. Two-nuclei, two-electron toy model system described by eq. 2.25. (Adapted from [40].)

Any wavefunction must obey orthogonality, so the relation $|\langle\psi_L|\psi_L\rangle|^2 = |\langle\psi_{EX}|\psi_{EX}\rangle|^2$ must also hold. This implies the two solutions being related by $\psi_L = \pm\psi_{EX}$ but this condition is not satisfied by each of the solutions as constructed. However, a linear combination of these states will satisfy both the distinguishability and orthogonality required by quantum mechanics. Those solution are given by $\psi_\alpha = \frac{1}{\sqrt{2}}(\psi_L + \psi_{EX})$ and $\psi_\beta = \frac{1}{\sqrt{2}}(\psi_L - \psi_{EX})$.

A third requirement states that the electron wavefunctions be antisymmetric due to the fermionic nature of the particle. This implies that a swap of electrons must be followed by a sign reversal of the wavefunction. Only ψ_β achieves this as written above. To make both linear combinations appropriate antisymmetric solutions, a spin matrix is associated with each: $\psi_{\uparrow\downarrow} = \psi_\alpha\chi_\beta$ prepares anti-parallel orientations of the spins having a total spin $S = 0$, and $\psi_{\uparrow\uparrow} = \psi_\beta\chi_\alpha$ results in parallel ordering of the spins, with $S = 1$. A perturbed Hamiltonian can be constructed which splits the two fundamental interactions into repulsive and attractive terms, respectively. The perturbed Hamiltonian is then written

$$H_{\boldsymbol{P}} = \left[\frac{e^2}{r_{12}} + \frac{Z_a Z_b e^2}{r_{ab}}\right] - \left[\frac{Z_a e^2}{r_{a2}} + \frac{Z_b e^2}{r_{b1}}\right] \quad \text{(eq. 2.26)}$$

and the expectation values of this Hamiltonian can be evaluated by computing $\langle\psi_{\uparrow\downarrow}|H_{\boldsymbol{P}}|\psi_{\uparrow\downarrow}\rangle$, $\langle\psi_{\uparrow\downarrow}|H_{\boldsymbol{P}}|\psi_{\uparrow\uparrow}\rangle$, and $\langle\psi_{\uparrow\uparrow}|H_{\boldsymbol{P}}|\psi_{\uparrow\uparrow}\rangle$, ultimately leading to the energy relation

$$E = K - \mathrm{J}(\tfrac{1}{2} + 2(\mathbf{S}_1 \cdot \mathbf{S}_2)) \quad \text{(eq. 2.27)}$$

with the terms $K = \langle\psi_L|H_{\boldsymbol{P}}|\psi_L\rangle$ (known as the Coulomb integral and related to the attraction terms of the Hamiltonian) and $\mathrm{J} = \langle\psi_L|H_{\boldsymbol{P}}|\psi_{EX}\rangle$ (known as the exchange integral, and corresponding to the repulsive terms of the Hamiltonian). For the configuration of two ½ spins in alignment, $2(\mathbf{S}_1 \cdot \mathbf{S}_2) \rightarrow 1/2$ giving $E_{FM} = K - \mathrm{J}$. For two ½ spins maximally out of alignment then $2(\mathbf{S}_1 \cdot \mathbf{S}_2) \rightarrow -3/2$ yielding $E_{AFM} = K + \mathrm{J}$. In this way, the energy between the parallel and antiparallel orientation of spin can be calculated by subtracting $E_{FM} - E_{AFM} = -2\mathrm{J}$. The lowest energy term, or ground state of the system, is then determined by the sign of the exchange interaction. Recalling the discussion above, $\mathrm{J} > 0$ leads to a positive value for $E_{AFM} - E_{FM}$, indicating a FM ground state. The opposite is true for $\mathrm{J} < 0$, which results in a positive $E_{FM} - E_{AFM}$ relation. The perturbed Hamiltonian gives clues to when the ferro or antiferromagnetic interaction will occur. If the first "repulsive" ${r_{12}}^{-1}$ term in the Hamiltonian is large, which occurs when unpaired spin densities are strongly localized near one another and far from a nuclear site, a ferromagnetic interaction between those spins will be favored. In contrast, when the overlap of the unpaired spins increases yet further and approaches a covalent sharing of electrons between nuclei, such as in bonding or charge-transfer states, an antiferromagnetic ground state will be favored. These situations are illustrated in Fig. 2.5 a and b [40].

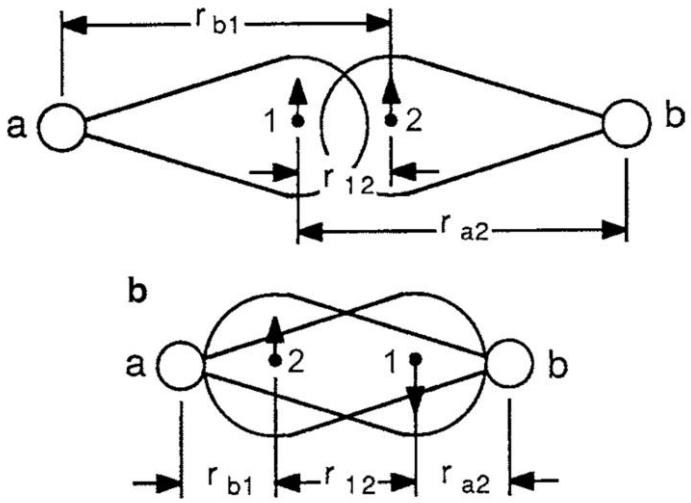

Figure 2.5. Overlap regimes of paramagnetic spins. a) illustrates weak overlapping leading to ferromagnetic ordering, while b) shows strong overlap, favoring antiferromagnetic interactions. (Adapted from [40].)

2.2. Molecule-Based Magnets

Molecule-based magnets (MBMs) are a relatively new class of magnetic materials, in which inorganic and organic ions or molecules holding localized, unpaired electron spin density strongly interact electronically and magnetically via chemical bonds or space [43,44]. Compared to conventional metallurgic and ceramic magnets – such as transition and rare earth metals and their perovskites, oxides, and fluorides, usually fabricated via high-temperature metallurgical or ceramics methodology [38,45,46] – the main benefits of MBMs are usually associated with their light-weight, mechanical flexibility, tunable color or transparency, low-temperature processing, solubility, and compatibility with polymers and other classes of molecular materials [47]. These interesting and potentially advantageous materials properties are principally achieved by the use of organic linkages to bridge metal centers, in contrast to the structural architectures of the "hard" magnetic materials mentioned above. This general composition allows the design of

molecule-based magnetic materials to benefit significantly from the field of coordination chemistry, from which a vast number of metal-ligand coupling configurations can be explored.

2.2.1. Prussian Blue and its Analogs

Cyanometallate compounds, such as Prussian Blue and its analogs, are an interesting starting point to consider 3d-spin coupling interactions through organic linkages in molecule-based magnets. Chemically, Prussian Blues are commonly formulated as $A_xM[M'(CN)_6]z•nH2O$, where A is an alkali metal cation, and M, M' are transition metals. Prussian Blues possess transition metal centers octahedrally coordinated by six CN bridges, resulting ideally in a face-centered cubic structure and are thus structurally similar to transition metal oxides. As in hard oxide magnets, the octahedral ligand field splits the five degenerate 3d l_z states into three lower energy t_{2g} symmetry states (d_{xy}, d_{xz}, d_{yz}) that each point away from the vertices of the ligand octahedron and two higher energy levels of e_g symmetry (d_z^2 and $d_{x^2-y^2}$) that align directly along these vertices. Additionally, they often possess defects in the cubic lattice due primarily to $[M(CN)_6]^{n-}$ vacancies [48,49], allowing water molecules to bind to unbridged metal sites. For some members of this family, the interstitial cubic voids in the crystal contain a charge-balancing alkali cation A^+ left by the aqueous solution of an $[A][M(CN)_6]$ salt. Some of these structural features are illustrated in Fig. 2.6 [50].

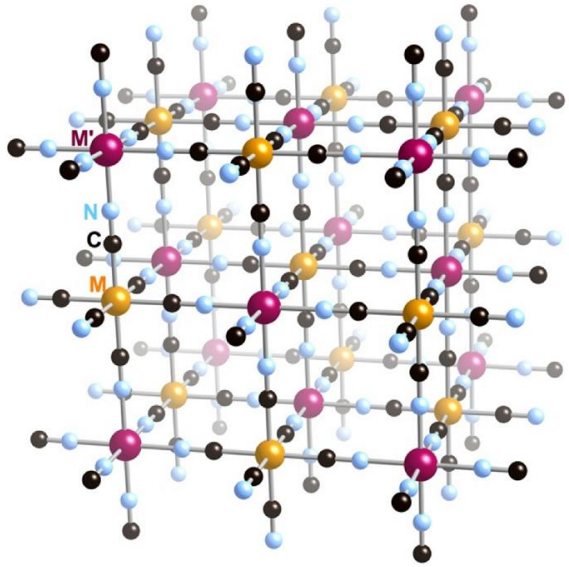

Figure 2.6. Idealized bimetallic Prussian Blue. (Adapted from [50].)

Prussian Blue itself is formulated $Fe^{II}_4[Fe^{III}(CN)_6]_3 \bullet 14H_2O$ and was first structurally characterized in 1972 [51]. It was found later to order as a ferromagnet with T_c = 5.6 K with spin structure resolved by neutron diffraction [48]. The spin occupation of the 3d orbital on transition metal centers significantly impacts the resulting properties of magnetic interaction in Prussian Blue and its analogs. For example, within the cubic $Fe^{II}_4[Fe^{III}(CN)_6]_3$ lattice, the high-spin Fe^{II} ions are structurally mediated by both the cyanide ligand and a diamagnetic low-spin Fe^{III} center; a structural shorthand with electron configurations for the transition metal is written $Fe^{III}(t_{2g}^3e_g^2)$ – NC – $Fe^{II}(t_{2g}^6e_g^0)$ – CN – $Fe^{III}(t_{2g}^3e_g^2)$. The schematic spatial and electron configuration just described is illustrated in Fig. 2.7 [49]. The previously mentioned studies found significant Fe^{II} spin delocalization onto the high-spin iron, though the total spin coupling pathway between Fe^{II} species was determined to be ~10 Å in length, suppressing a strong overlap of paramagnetic spins and thus robust magnetic coupling.

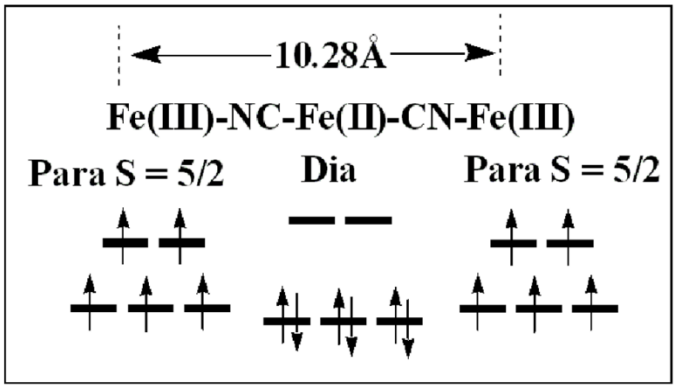

Figure 2.7. Electronic configuration for Prussian Blue. (Adapted from [49].)

Strategies were sought to enhance the spin coupling by fully populating the crystal with high-spin metallic species to shorten distance between spin hosts and enhance overlap of paramagnetic orbitals through the cyano bridge. This was later achieved by the synthesis of the bimetallic Prussian Blue analog $CsMn^{II}[Cr^{III}(CN)_6]$, which was found to order as a ferrimagnet with $T_c \sim 90$ K, proving this strategy useful as a means to enhance magnetic coupling strength [52].

Compared to oxide magnets, the diverse properties of the ligands in molecule-based magnets, in addition to the transition metal identity and its spin-configuration, play a key role in the stabilization of the magnetic ground state. For example, in contrast to the sole π orbitals responsible for the mediation of superexchange in transition metal oxides, the cyano ligands in Prussian Blues possess relatively delocalized π bonding and unoccupied π^* antibonding states that extend spatially across the ligand, in addition to an asymmetric metal bonding through both carbon and nitrogen, illustrated in Fig. 2.8 a-c, adapted from [50]. The asymmetry of the ligand binding to metal sites creates two distinct ligand-field environments, i.e.$[M(CN)_6]$ and $[M'(NC)_6]$, and impacts the octahedral crystal field splitting energy (Δ_0) between the t_{2g} and e_g

manifolds, typically yielding low-spin and high-spin electron configurations from the carbon- and nitrogen-side complexation of metals, respectively.

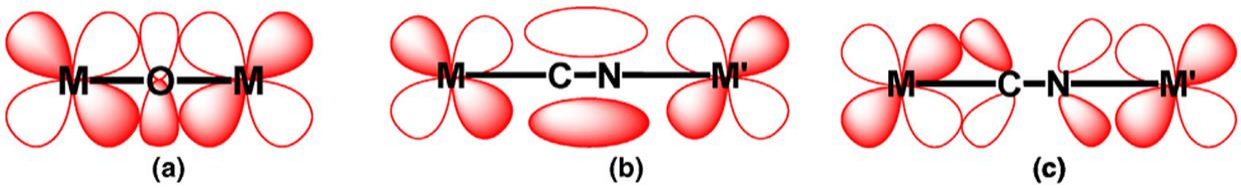

Figure 2.8. *d*-orbital overlap mediated by diamagnetic *p*-orbitals. a) *d-p-d* ferromagntic exchange in metallic oxides (orthogonal orbital phase), b) ferromagnetic and c) antiferromagnetic *d-p-d* exchange through CN *p* orbitals in Prussian Blue materials. (Adapted from [50].)

Furthermore, the cyanide ligand is a weak and σ-donor, yielding covalent bonding with metals, while simultaneously a moderate π-acceptor, enabling electron donation from metal to the empty π^* ligand states. Therefore, spin transfer from the metal species can occur through both σ and π charge-transfer mechanisms via a M(d_z^2)-NC(p_z) mixing of σ symmetry, or M(d_{xz}, d_{yz})-NC(p_x, p_y) interaction of π symmetry. M-CN mixing is expected to be much weaker in contrast to the M-NC type due to the comparatively small spin density distributed over the carbon atoms in hexacyanometalate salts [53,54]. By exploiting the back-bonding properties of the cyanide ligand through targeting more diffuse, relatively high-energy 3d t_{2g} orbitals characteristic of early transition metals, enhancement of metal-metal spin coupling was sought in this material class [49]. Using this approach, a bimetallic Prussian Blue analog containing V^{II} and Cr^{III} species was synthesized and shown to order magnetically with T_c ~ 376 K [55]. In fact, using a variety of early transition metals (typically V, Cr, and Mn) in a number of compositions, several reported materials in this class were developed with T_c > 100 K [56-60]. In addition to the exhibiting relatively high T_c, Prussian Blue analogs have been shown to possess properties desirable for the formation of functional devices, such as thermal and optical control of magnetism [61-70].

2.2.2. M[TCNE] Molecule-Based Magnets

The preceding examples illustrate the flexibility available to rationally optimize or tune the magnetic or electronic properties of molecule-based magnets. Through judicious choice of transition metals present in precursor materials, a T_c increase of nearly 70x was achieved within the Prussian Blue class of materials. While understanding the electronic properties of the organic moiety was shown to be of tremendous benefit, ultimately the cyanide ligand acts as a spectator in the stabilization of magnetic order, as it carries no spin density of its own. It was conceivable that a metal-organic framework containing paramagnetic spins on both a transition metal (3d) and an organic radical ligand (π or π^*) would order magnetically, and in turn create an entirely new class of hybrid magnet. To achieve this, tetracyanoetythlene (TCNE) was sought as a ligand for molecule-based magnets synthesis. Structurally similar to ethylene with four hydrogens each replaced by a cyano group, it is known to readily undergo single electron reduction, resulting in the population of a π^* orbital [71]. This delocalized, singly occupied π^* orbital was visualized in for the $TCNE^{\bullet-}$ radical fragment by neutron diffraction on a single crystal of the $Bu_4N^+[TCNE]^{\bullet-}$ material (Bu_4N = tetrabutylammonium) [72,73], illustrated in Fig. 2.9.

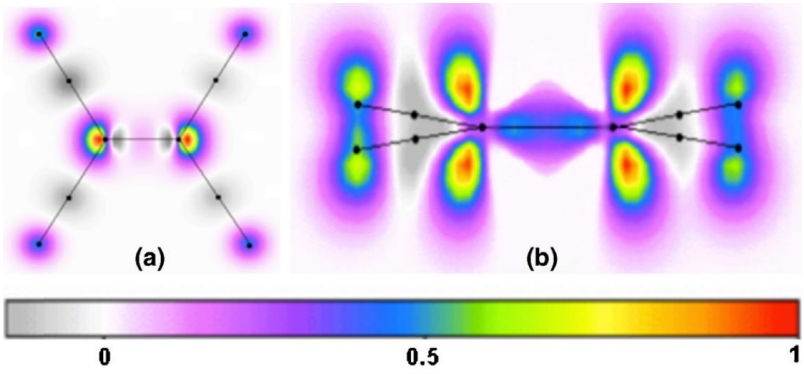

Figure 2.9. Distribution of π^* spin on the $TCNE^{\bullet-}$ radical fragment of $Bu_4N^+[TCNE]^{\bullet-}$ crystal, determined by single crystal neutron diffraction. Views perpendicular (a) and parallel (b) to the molecular plane. Units of $\mu_B/Å^2$ on scale. (Adapted from [50].)

The radical $S = ½$ spin was found to delocalize across the molecule, with the major components of ~33% on each of the central carbons belonging to the C=C double bond and ~13% of spin on each nitrogen from the cyano group. In addition to the spin-host capabilities of the molecule, the D_{2h} molecular symmetry of $TCNE^{\bullet-}$ provides a much greater flexibility as a "building block" for magnetic network coordination than the cyanide ligand alone.

An organic-based magnet utilizing spins on both a metal center and a p-orbital radical for coupling was first achieved in 1985 by Miller and colleagues through the discovery of $[Fe^{III}(C_5Me_5)_2]^+[TCNE]^{\bullet-}$ [74]. Structurally, this magnet and several of its solvates form ionic molecular crystals that spatially order in chain-like stacks consisting of the $[TCNE]^{\bullet-}$ ($S = ½$) radical and the decamethylferrocene cation (also possessing $S = ½$). This crystal arrangement lacks covalent bonding between the metal center and organic spin host, and is considered structurally zero-dimensional. Fig. 2.9a illustrates this crystalline motif.

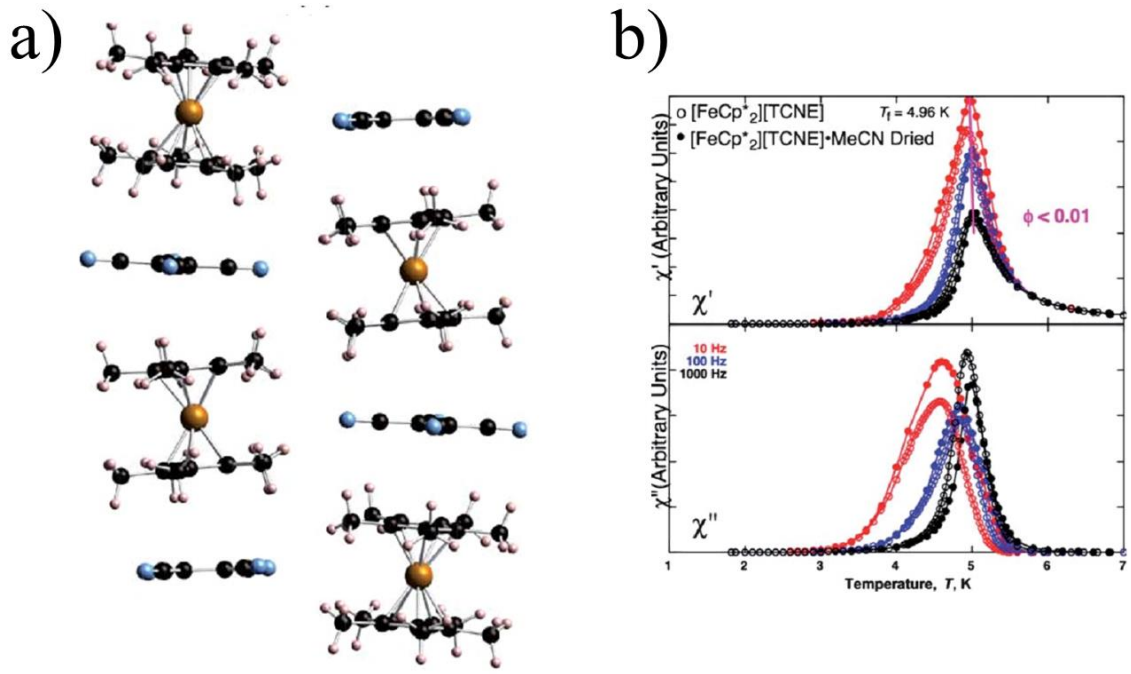

Figure 2.10. Crystal structure (a) and magnetic ordering (b) of $[Fe^{III}(C_5Me_5)_2]^+[TCNE]^{\bullet-}$. (Adapted from [75].)

Unexpectedly, $[Fe^{III}(C_5Me_5)_2]^+[TCNE]^{\bullet-}$ was found to order magnetically as a ferromagnet (T_c ~ 5 K) despite lacking a clear exchange pathway for spin electron overlap (Fig. 2.9b). Later, the compound $[Mn^{III}(C_5Me_5)_2]^+[TCNE]^{\bullet-}$ was synthesized and found to have T_c ~ 9 K [76], due presumably to an enhancement of cation spin density with respect to the iron compound ($[Mn^{III}(C_5Me_5)_2]^+$, S =1), in accord with a typical mean-field prediction of enhancement of transition temperature through increase of spin magnitude, i.e. $T_c \propto S(S+1)$ [77]. Currently, the mechanism for spin coupling, and ultimately the appearance of measurable magnetic order, is still poorly understood in this structural class of magnet. Spin correlation is thought to arise predominantly due to a interchain $[Fe^{III}(C_5Me_5)_2]^+ \ldots [TCNE]^{\bullet-}$ exchange, though these one-dimensional couplings cannot fully explain the appearance of a bulk three-dimensional transition required for magnetic ordering [78]. Excited-state facilitated magnetic exchange along these quasi-1D "chains", in addition to an interchain dipolar coupling between them has been speculated, though some evidence from first-principles modeling has been put forward in support of this mechanism [74,77,78].

Enormous interest in M[TCNE] compounds was subsequently developed due to the discovery of the first organic-based ferromagnet, with this interest accompanied by significant efforts to synthesize new members of the M[TCNE] class of materials. In the intervening time, a large number of materials have been synthesized and characterized magnetically and structurally. M[TCNE] complexes have come to represent one of the most interesting classes of MBMs, possessing numerous compositions and structures such as inorganic polymer chains [76], two-dimensional layers [79-81] where M^{II} sites are coordinated by $TCNE^{\bullet-}$ and solvent ligands (e.g. MeCN [82,83]; H_2O [84]), three-dimensional networks [85], and amorphous solids [27]) with a

wide range of magnetic ordering temperatures T_c. Some important members of this family are considered below.

2.2.3. $[Mn^{III}(TPP)][TCNE]$ Magnets

[Mn(TPP)][TCNE] (TPP = *meso*-tertraphenylporphyrin) is an organic ferrimagnet exhibiting a canted 1D chain structure of alternating $D^+A^-D^+A^+$ (D = Mn^{III}(TPP), A = TCNE) moieties, with the TCNE molecule bound in a *trans*-μ-N-σ configuration to each [Mn(TPP)] site [86], shown in Fig. 2.10. Saturation magnetization studies on this class of 1D chain compounds suggest an antiferromagnetic ordering below T_c between the spin-bearing S = 2 $[Mn^{III}(TPP)]^+$ and S = 1/2 $TCNE^{\bullet-}$ components through direct-exchange between 3d Mn^{III} - d_z^2 and $TCNE^{\bullet-}$- π* orbitals, ultimately resulting in an enhanced T_c (~ 8-28 K) relative to the structurally 0D $[Mn^{III}(C_5Me_5)_2]^+[TCNE]^{\bullet-}$. The discovery of this material further illustrated the rational procedure to enhance magnetic ordering via the direct coupling of the spin bearing ligand to the metal site. The [Mn(TPP)][TCNE] parent compound may be synthetically modified by precursor chemistry to include substituents on the phenyl rings in addition to inclusion (or subsequent thermolytic removal) of interstitial solvent molecules. This action led to significant structural differences between polymorphs in this species by causing a tilting of the metalloporphyrin ring with respect to the TCNE molecule, a result which has recently enabled an experimental magneto-structural correlation, investigating the role of orientational dependence of d_z^2-π* overlap on magnetic behavior [77,87,88]. The direct overlap of paramagnetic orbitals, and subsequent stabilization of long-range magnetic order, was thus demonstrated again as a crucial aspect in design of magnetic materials with improved T_c.

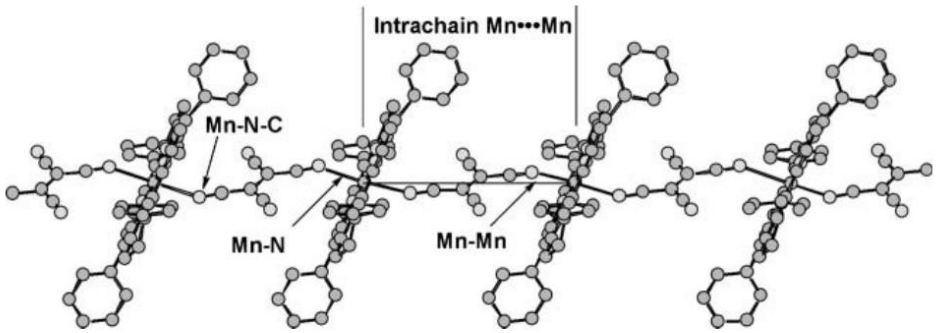

Figure 2.11. Isolated chain structure of [Mn(TPP)][TCNE]. (Adapted from [87].)

2.2.4. $V^{II}[TCNE]_x$ ($x \sim 2$)

Some of the most important properties of this material as a candidate for technological application were discussed in Chapter 1. Despite the amorphous nature of the $V[TCNE]_x$ compound (synthesized both in solution and via chemical vapor deposition), significant effort has successfully elucidated some details of the local or short-range structural features of $V[TCNE]_x$ materials and films. Initially, magnetic saturation and infrared absorption studies suggested the 3d metal ions exhibit a 2+ valence state and are octahedrally coordinated by a minimum of four nitrogen atoms from the $TCNE^{\bullet-}$ moiety, with the radical ligand intact throughout the material, possibly facilitating a disordered 3D networked structure. These structural factors were subsequently confirmed by *K*-edge extended X-ray absorption fine structure experiments on chemical vapor deposition grown $V[TCNE]_x$ films revealing that the V ions indeed exhibit a 2+ valence state and are coordinated by 6.04 ± 0.25 nitrogen atoms of $TCNE^{\bullet-}$ at room-temperature with an average distance of ~2.08 Å [89]. These $TCNE^{\bullet-}$ ligands form six σ-type coordination bonds due to an axial overlap of metal 4*s*, 4*p*, $3d_z^2$ and $d_{x^2-y^2}$ orbitals with hybrid (*s*-*p*) orbitals of the ligand (σ-donation). Since $TCNE^{\bullet-}$ has four coordination

sites, it bridges M^{II} ions and vice versa, forming a network-like coordination compound supporting the proposed network-like structure of $V[TCNE]_x$ [89]. For $x = 1.5$ [85] all four $TCNE^{\bullet-}$ nitrile groups are coordinated, while in case of $x \sim 2$ (as it is in $V[TCNE]_x$) only ~3 out of the 4 $TCNE^{\bullet-}$ nitrile groups, on average, should be coordinated [90]; therefore, $TCNE^{\bullet-}$ ions may experience a statistically different environment resulting in an apparent lack of long range order, in part to V^{II} vacancies.

2.2.5. Magnetic Behavior and Electronic Structure of $M^{II}[TCNE]_x$ (M = V, Fe) Films

In the case of early 3d transition metals such as V^{II} or Ti^{II}, the half-filled non-bonding 3d t_{2g} manifold should be expected to be close to the Fermi edge, separated from the unoccupied antibonding e_g manifold by the crystal field parameter $\Delta_o = 10Dq \sim 2$ eV. Conversely, for M = Cr, Mn, Fe, Co, Ni both 3d t_{2g} and e_g manifolds become populated, which may result in their reduced overlap with ligand π* states. This conventional chemical bonding scheme for the occupied density of states was recently confirmed by resonant photoemission, positioning the V^{II} 3d t_{2g} manifold at -1.0 eV, as well as π and singly occupied π* $TCNE^{\bullet-}$ related orbitals at -3.5 and -2.5 eV, respectively [91-93] (Fig. 2.12, red). In contrast, the Fe^{II} 3d-derived states of the recently grown films of $Fe[TCNE]_x$ appear at much higher binding energy of ~4.5 eV (Fig. 2.10, black), while derived mainly from the $TCNE^{\bullet-}$ π and singly occupied π* orbitals have energies similar to those in $V[TCNE]_x$ at ~3.0 and ~1.7 eV vs. Fermi level, respectively [94].

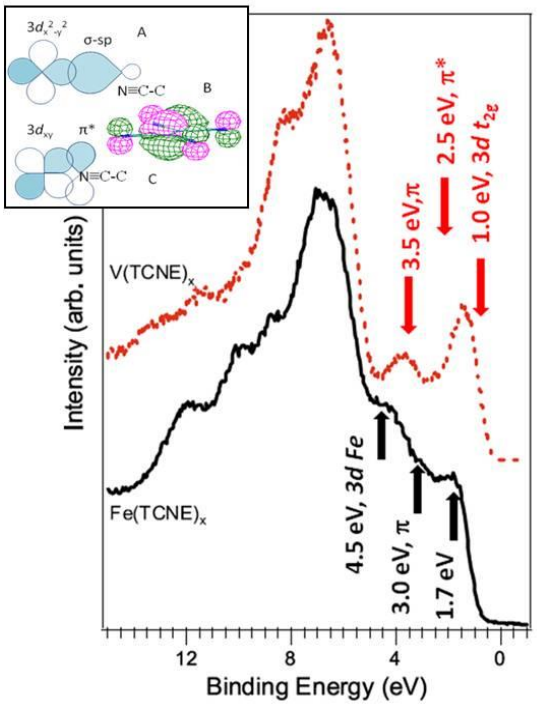

Figure 2.12. XPS spectra of $Fe^{II}[TCNE]_x$ and $V^{II}[TCNE]_x$ (x ~2) thin films (Adapted from [94]). Inset: modes of 3d-π* orbital overlap; a) σ-donation, b) $TCNE^{\bullet-}$ π* orbital, c) π-backbonding.

Due to a small (~0.6 eV) crystal field parameter Δ_o the 3d t_{2g} and e_g states are not fully resolved. The unoccupied electronic structure (with a positive binding energy) was also probed by x-ray absorption, X-ray magnetic circular dichorism and near-edge X-ray absorption fine structure, but no rigorous determination of the chemical origin or spin polarization of the lowest unoccupied state was made. It is postulated that the lowest unoccupied state is from a Coulomb split π*, or a π*+U_C state (where U_C is the Hubbard correlation energy) at +0.5 eV with e_g* at +1.3 eV, expected from the Coulombic exchange interaction of the half-filled π* band with the M 3d electronic states.

2.3. Origins of Magnetic Exchange in M[TCNE] MBMs

Magnetic studies of M[TCNE] magnets [30,95-98] suggest that ordering results from strong antiferromagnetic (AFM) exchange between unpaired spins residing on the M 3d orbitals

(S = 1/2 – 5/2) and delocalized unpaired p electrons (S = ½) residing on the π* molecular orbital of $TCNE^{\bullet-}$. This approach, first formulated by Miller and Epstein in 1988, explains relatively well the magnetic behavior of several TCNE based magnets [99]. Following the bonding scheme and traditional superexchange definition, it is conceivable that the $TCNE^{\bullet-}$ π* singly occupied orbital directly overlaps with M 3d spins, or it may provide a superexchange pathway for such interaction. As mentioned above, neutron scattering studies of $TCNE^{\bullet-}$ demonstrated that ~1/8 of the unpaired electron density resides on each C≡N group of $TCNE^{\bullet-}$ [72], and it is plausible that there exists a weak hybridization between the lone pair and π* molecular orbitals in coordinated $TCNE^{\bullet-}$.

In 1993 Tchougreeff and Hoffman proposed that the ferrimagnetic ground state of $V[TCNE]_x$ arises due to weak electron hopping between the V^{II} 3d and π* orbital of $TCNE^{\bullet-}$ [100]. Recently a double-exchange model, in which electron hopping between metal and ligand facilitates metal 3d-to-$TCNE^{\bullet-}$ magnetic exchange, was also put forth [101]. The idea of electron density transfer from metal to ligand is well known and is used, for example, to describe C≡O bond weakening in metal carbonyls [102]. Since backbonding produces a transfer of electron density from metal to ligand, it could also be key in describing the semiconductor transport of $V[TCNE]_x$. Recent characterization efforts have sought to highlight the ground electronic state of the $V[TCNE]_x$ magnet, in hopes to find the key features underlying its exceptional electronic and magnetic properties. Kortright et al. [93] hypothesized that the metal-to-ligand charge-transfer between electrons on the V 3d t_{2g} manifold and π* orbital of $TCNE^{\bullet-}$ mediate a strong antiferromagnetic interaction in $V[TCNE]_x$; however, XAS and XMCD results do not provide direct evidence of this effect. In contrast, Tengstedt *et al*. [91], acquiring and analyzing very similar spectra of the spin resolved unoccupied electronic structure, but using a

ligand field multiplet calculation to fit the acquired data, concluded that the V^{II} 3d ground state consists of a 60% $3d^3$ and 40% $3d^4\underline{L}$ ($\underline{L}$ = hole on $TCNE^{\bullet-}$ ligand) filling. This implied that there exists a hybrid state with substantial ligand to metal charge transfer, in contrast to Kortright's findings.

2.3.1. Electronic Structure Calculations of M[TCNE] Magnets

Uncertainty of the detailed electronic contributions to the magnetic ground state in M[TCNE] MBMs, as illustrated above, has been a primary motivator for theoretical treatment of their electronic interactions. The early example of unexpected ferromagnetic ordering in the $[Fe^{III}(C_5Me_5)_2]^+[TCNE]^{\bullet-}$ compound generated broad interest in a computational elucidation of the magnetic coupling, thought best to be achieved through quantum chemistry approaches due to the molecular nature of its spin hosts and the availability of XRD crystal structures. Density functional theory (DFT) is widely used and efficient theoretical framework to evaluate electronic properties and structures of large molecular systems and crystals, through pure DFT functionals such as LDA have been shown to provide incorrect descriptions of d-orbital energies and their spatial localization while producing spuriously small band gaps for insulating materials [103-105]. This is particularly problematic for 3d-containing magnetic insulators in the M[TCNE] family. Hybrid density functional approaches such as B3LYP have been found to overcome many of these pathologies via the inclusion of some portion of exact Hartree-Fock electronic exchange interaction, and have since been employed heavily in the simulation of M[TCNE] electronic and magnetic properties.

For the organic ferromagnet $[Fe^{III}(C_5Me_5)_2]^+[TCNE]^{\bullet-}$, initial experimental studies of the magnetic behavior were mechanistically inconclusive, and competing explanations for ferromagnetic order were proposed. A virtual electron transfer from through a mixing of ground

and excited states [74], and a spin polarization driven coupling where positive spin on the Fe^{III} center negatively polarizes cyclopentadienyl π orbitals, stabilizing a positive π* spin on the $TCNE^{\bullet-}$ moiety [106] were thought. Spin-unrestricted density functional theory calculations utilizing the hybrid B3LYP functional initially suggested that a spin polarization mechanism was responsible, via a natural orbital analysis of reduced $[M^{III}(C_5Me_5)_2]^+[TCNE]^{\bullet-}$ (M= Fe, Mn, Cr) model complexes. Additionally, magnetic exchange coupling constants *J* reasonably close to experimentally derived ones were calculated through a broken-symmetry approach, fitting a Heisenberg Hamiltonian (eq. 2.24) with energy gap between ferro- and antiferromagnetic configurations of $[M^{III}(C_5Me_5)_2]^+$ and $TCNE^{\bullet-}$ spins (see eq. 2.27 and following discussion). However, the lack of spatial overlap of orbitals in the ground state made the interpretation of broken-symmetry magnetic couplings unclear, and the proposed excited-state contribution to the magnetism could not be evaluated. This was later overcome by Miller and colleagues [78]. Informed by previous DFT simulation, complete active space calculation involving the 3d and π* electrons on each spin-bearing moiety of a reduced model system stabilized a triplet state in accord with the experimentally observed ferromagnetism. Additionally, this state was found to possess a through-space d_{xz} - π* orbital hybridization, validating a broken broken-symmetry approach to magnetic coupling estimation used in the same study and previously. In accord with the ground state, magnetic coupling within the molecular spin host's quasi-1D "chains" (see Fig. 2.9a) was found to be ferromagnetic, while both antiferro- and ferromagnetic couplings between moieties of different chains ($[Fe^{III}(C_5Me_5)_2]^+$ to $[Fe^{III}(C_5Me_5)_2]^+$, etc.) were predicted, but with magnitudes on the order of error in their evaluation. Thus, the hybrid DFT and active-space simulations proved invaluable in unraveling the details of the unusual magnetic ground state in this molecular crystal.

Structure-properties correlations have also been investigated computationally via experimentally derived model systems. Recently, simulations were performed on reduced 1D chain [Mn^{III}(TPP)][TCNE] model complexes to investigate the role of orientational dependence of d_z^2 - π^* overlap and magnetic coupling constants on spatial canting and rotation of the $TCNE^{\bullet-}$ moiety with respect to the Mn^{III}(TPP) ring. Experimental results have shown an enhancement of the Weiss coupling constant θ with dihedral angle reduction between these moieties [77,107]. Simulations utilizing B3LYP were found to reproduce these coupling tendencies while producing reasonable magnetic coupling constants [87,108-111], confirming the sensitivity of 3d-π^* overlap to structural changes, as well as the antiferromagnetic spin coupling within its linear 1D structural chains. This further demonstrates the utility of theoretical tools to enhance understanding of the impact of local crystal morphology on electronic structure and magnetism.

In contrast to the examples above, which have typically utilized reduced model fragments of M[TCNE] crystals, recent efforts have been made to investigate the band structure and spin polarized density of states from full structures of M[TCNE] magnets, using periodic boundary conditions and various DFT approaches [112-116]. The aforementioned calculations were performed utilizing the local spin density functional LSDA+*U*, where *U* is a Hubbard-like "Coulomb repulsion" term added to some of the diagonal elements of DFT's Kohn-Sham matrix, expressed in the basis of localized atomic orbitals. For M[TCNE] calculations the *U* term was added for both the d-shells of metal ions and p-shells of carbon and nitrogen atoms to ensure the convergence of calculations to a spin-polarized ground state [33,117,118]. However, as discussed above, the LDA approach often fails for 3d-electron containing materials, predicting a metallic ground state for ferrous iron [119], in contrast to the experimentally observed insulating

state. Similar discrepancies have been observed when the LSDA functional was used for modeling the electronic structure of the two-dimensional layered $[Fe^{II}(TCNE)(NCMe)_2]Fe^{III}Cl_4$ MBM [117,118], whose crystal structure is shown in Fig. 2.10a.

To overcome this drawback, the now widely used hybrid functional B3LYP [120] was implemented to model the spatial and electronic structure of M[TCNE] (M = V, Nb) [113,116]. Since $V[TCNE]_x$ is amorphous and Nb[TCNE] compound was not structurally characterized [121], a hypothetical M[TCNE] (M = V, Nb) crystal structure was proposed on a basis of the available experimental data on V^{II} local coordination environment [89] and the isolated $TCNE^{\bullet-}$ ion geometry [122]. Despite this limitation, the computations nonetheless revealed a strong metal-ligand interaction. The magnitude and sign of the magnetic exchange parameters, obtained using a broken-symmetry DFT approach, revealed a ground state AFM coupling between the V^{II} ions and the $TCNE^{\bullet-}$ ligands in all crystallographic directions in accord with the observed high T_c. However, the authors pointed out that this qualitative agreement with experimental results provides only indirect support for the structure model adopted for calculations. Moreover, the essential character of the magnetic ground state was not fully investigated, leaving open the question about the relationship between charge transfer, spin hybridization, and magnetic ordering in $V[TCNE]_x$.

2.4. New $[M^{II}(TCNE)(NCMe)_2]X$ (M = Fe, Mn, Ni, X = PF_6, AsF_6, SbF_6) Magnets

Uncertainty of the electronic structure ultimately responsible for the magnetic ground state, combined with the lack of long range spatial ordering in $V^{II}[TCNE]_x$ prepared via numerous methods leaves open many basic questions about structure-properties correlations in networked M[TCNE] magnets. Despite a number of successful attempts to resolve the crystal structures of various M[TCNE] complexes, few synthetic routes have been available that

simultaneously provide the flexibility to alter transition metal identity and/or structural lattice dimensionality and topology, while producing crystalline material. As was illustrated by the example of Prussian Blue and its analog structures, such synthesis flexibility is crucial for the pursuit of an experimentally rigorous composition- and structure-function investigation for MBMs, and is likewise needed within the M[TCNE] class.

Recently, the discovery of a new structural type of M[TCNE] magnet was reported [81]. The material was synthesized via the reaction of TCNE and $FeCl_2$ with acetonitrile solvate in dichloromethane CH_2Cl_2:

(1) $2[Fe(\mu\text{-}Cl)_2(NCMe)_2] + TCNE \rightarrow [Fe^{II}(TCNE)(NCMe)_2]Fe^{III}Cl_4\,(s) + 2MeCN$

The product $[Fe^{II}(TCNE)(NCMe)_2]Fe^{III}Cl_4$ is insoluble in dichloromethane, and a polycrystalline solid was subsequently crashed out of reaction solution. This complex was found to possess a quasi-2D structural motif of positively charged $(MeCN)_2\text{-}Fe^{II}(\mu_4\text{-}TCNE^{\bullet-})$ slabs with charge-balancing and non-magnetic $Fe^{III}Cl_4$ anions trapped between layers, illustrated in Fig. 2.11a. Magnetically, it was found to order as an Ising Ferrimagnet with $T_c \sim 90$ K [81,118]. The evident reduction of TCNE to the $TCNE^{\bullet-}$ radical, whose presence is necessary for both structural formation of M[TCNE] MBMs and stabilization of their high-T_c magnetic ordering, was rigorously investigated by performing similar chemistry in aceotonitrile (MeCN) solvent [123]. The layered 2D compound $[Fe^{II}\{C_4(CN)_8\}(NCMe)_2]$ was produced which was found to possesses neutral $(MeCN)_2\text{-}Fe^{II}(\mu_4\text{-}[C_4(CN)_8]^{2-})$ slabs where $[C_4(CN)_8]^{2-}$ results from a σ-dimerization of two $TCNE^{\bullet-}$ radicals, illustrated in Fig. 2.11b. This material was found to be a much weaker magnet, exhibiting $T_c \sim 8$ K, presumably due to a long Fe^{II} superexchange path through a diamagnetic $[C_4(CN)_8]^{2-}$ linkage. The multi-step reaction sequence was proposed for this unusual dimerized structure to be:

(1) $3[Fe^{II}(\mu\text{-}Cl)_2(NCMe)_2] + 2MeCN \rightarrow 2[Fe^{II}(\mu\text{-}Cl)_2(Cl)(NCMe)]^- + [Fe^{II}(NCMe)_6]^{2+}$

(2) $2[Fe^{II}(\mu\text{-}Cl)_2(Cl)(NCMe)]^- + 2TCNE \rightarrow 2Fe^{III}Cl_3 + 2TCNE^{\bullet-} + MeCN$

(3) $[Fe^{II}(NCMe)_6]^{2+} + 2TCNE^{\bullet-} \rightarrow [Fe^{II}\{C_4(CN)_8\}(NCMe)_2]$ (s) + 4MeCN

(4) $2Fe^{III}Cl_3 + n MeCN \rightarrow [Fe^{III}Cl_4]^- + [Fe^{III}Cl_2(NCMe)_n]^+$

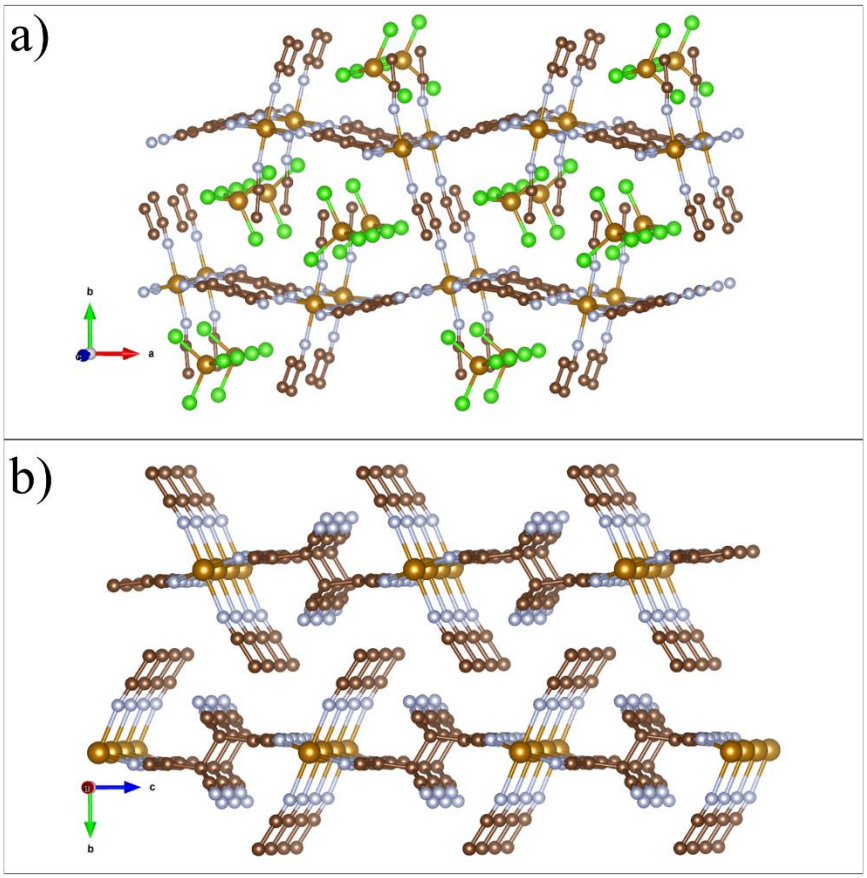

Figure 2.13. The 2D layered magnets $[Fe^{II}(TCNE)(NCMe)_2]Fe^{III}Cl_4$ (a) and $[Fe^{II}\{C_4(CN)_8\}(NCMe)_2]$ (b). Hydrogen omitted for clarity.

Within step 2, the reduction of TCNE to $TCNE^{\bullet-}$ occurs only due to the sufficient reduction potential of the $FeCl_2$ acetonitrile solvate. Thus, isostructural materials based on other transition metal solvates (i.e. Mn, Co) could not be achieved through this route. The formation of the $[Fe^{II}\{C_4(CN)_8\}(NCMe)_2]$ networked structure was thus explained by the availability of reduced TCNE in a 2:1 ratio to an acetonitrile solvate of metal. Equation 3 above is also

significant beyond explaining the formation of the $[Fe^{II}\{C_4(CN)_8\}(NCMe)_2]$ magnet. This reaction step suggests that a $M^{II}(NCMe)_6$ solvate in the presence of the $TCNE^{\bullet-}$ radical in solution may in general lead to formation of networked compounds, possibly possessing interesting magnetic properties. By removing redox chemistry and introducing these ions directly, it is conceivable that a number of transition metals may be used to form $[M^{II}\{C_4(CN)_8\}(NCMe)_2]$ or $[M^{II}(TCNE)(NCMe)_2]X$ complexes. The latter is a promising synthetic target as the $[Fe^{II}(TCNE)(NCMe)_2]Fe^{III}Cl_4$ material exhibits both high transition tepmerature for its class and is polycrystalline, enabling structure determination. Obtaining the $[M^{II}(TCNE)(NCMe)_2]X$ complex could be acheived through a generalized synthesis scheme as follows:

(1) $[M^{II}(NCMe)_6]X_2 + Bu_4N[TCNE] \rightarrow [M^{II}(TCNE)(NCMe)_2]X\,(s) + 4MeCN$

This reaction scheme fulfills many synthetic requirements necessary for rigorous exploration of structure/composition relationships:

i. Exploration of the orbital filling by varying the transition metal in structurally similar magnets through variation of the precursor $[M^{II}(NCMe)_6]X_2$ affords the opportunity to explore the impact of electronic structure on magnetic and spectroscopic characteristics.

ii. Changing anion X volume between 2D $[M^{II}(TCNE)(NCMe)_2]X$ layers may introduce structural perturbations that provide a way to evaluate the impact of layer topology or interlayer coupling upon magnetism.

iii. The crystal structures of structurally related M[TCNE] magnets provide a model system to explore rigorously the details of enhanced magnetic coupling in this class of materials through first-principles modeling. These models provide insights into electronic and magnetic ground states not possible from experimental probes.

Thus, the above synthetic scheme should enable a systematic study of composition- and structure-properties analysis by variation of transition metal center and interlayer spacer. In the following chapters, these approaches are presented and findings discussed.

2.5. Conclusion

In this chapter, a fundamental review of magnetism, in addition to milestone materials and results in MBM research was presented. The current state of understanding regarding the electronic, magnetic, and structural properties of the crucially important $V[TCNE]_x$ material was highlighted. New Fe[TCNE]-based materials and the synthetic insights afforded by their detailed reaction chemistry analysis were discussed. Finally, a new synthetic route to obtain a wide variety of $[M^{II}(TCNE)(NCMe)_2]X$ structured magnets was proposed, and opportunities to conduct systematic studies targeting composition and structure with this new route were highlighted.

3. METHODS

3.1. Introduction

In this chapter, the spectroscopic, magnetometric, and computational methods used extensively for material characterization and analysis in this thesis are discussed. First, a basic theoretical overview of vibrational transitions in solids is presented, and the complementary techniques of confocal Raman scattering and infrared absorption spectroscopy highlighted. Next, spectroscopic equipment overviews and sample preparation methods are reviewed. Magnetometry is subsequently discussed in terms of measurement equipment used, complementing the discussion of basic magnetic phenomena in Chapter 2. Magnetic sample preparation and handling is illustrated, in addition to explanation of all magnetic measurement protocols used in subsequent chapters. Finally, a brief discussion regarding computational approaches to simulate the electronic structure of M^{II}[TCNE] MBMs is presented.

3.2. Vibrational Spectroscopy

Conceptually, spectroscopic techniques represent the measurement of response properties via matter's interaction with electromagnetic radiation of various energies and intensities. These techniques are extremely useful as a means to probe the vibrational, rotational, and electronic states of materials, providing key information about composition, chemical bonding environment, and electronic structure [124]. Both Raman and infrared (IR) excitations can be utilized for vibrational spectroscopy, but are achieved through different physical processes. In IR probes, a direct absorption of low-energy photons (typically in the range E = 0.005 - 0.5 eV) results in vibrational and rotational energy level excitation through shift in the molecular dipole. In Raman, matter is illuminated by an intense, monochromatic light source (typically by laser

with photon in the visible energy band) which causes excitation into a virtual "vibronic" state. This virtual state possesses a vanishingly short lifetime, and a non-emissive photon of lower or higher energy than the source is quickly scattered, leaving the matter in a higher (Stokes scattering) or lower (anti-Stokes scattering) energy vibrational level respectively. This process is achieved through perturbation of the matter's polarizability field, a quantity that relates the dipole moment to the excitation field. These techniques provide complementary vibrational information by virtue of the modes activated by each process. See Fig. 3.1, adapted from [125].

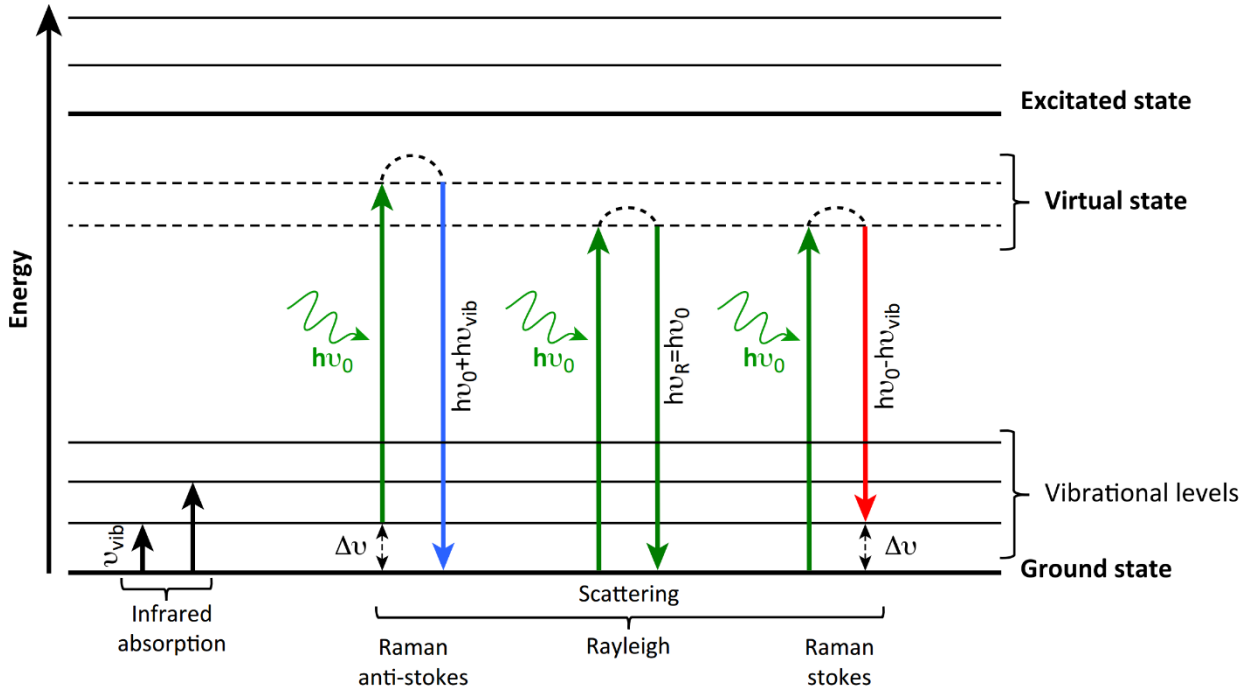

Figure 3.1. Jablonski diagram for vibrational and Raman excitations. (Adaped from [125].)

For M[TCNE]-based materials, probing the ligand vibrational states was expected to yield valuable information related to the properties listed above. It is known that the TCNE molecule (or molecular moiety in the case of M[TCNE] complexes) possesses both Raman and IR active modes, necessitating a comprehensive study by both techniques. These results are presented in the subsequent chapters. What follows is the basic theoretical background,

equipment outline, measurement method overview and sample preparation description and for each approach.

3.2.1. Vibrational Transitions

The transition from ground to excited states can be written succinctly in the language of quantum mechanics [126]. Here the probability of transition from level *j* to level *i* is usually written as the square of the transition matrix element

$$[H]_{ij} = \langle \Phi_i | H | \Phi_j \rangle \qquad \text{(eq. 3.1)}$$

where *H* is some operator acting upon the quantum system. In general, the total wavefunction of the system contains vibrational, rotational, and electronic portions. Assuming that the total wavefunction is separable into these portions allows them to be considered individually. Only the vibrational part Φ_i is used since rotational degrees of freedom are quenched in most solids, and electronic transitions are not probed. Since vibrational excitations involve the motion of nuclei by definition, the potential energy landscape created due lattice or chemical bond dynamics must be considered. For small displacements, the harmonic approximation works a means to decouple a many-body potential-energy landscape into an analytically solvable one coordinate expression. Mathematically the harmonic approximation is a Taylor expansion of the excitation operator H in terms of the normal coordinates Q_k of the nuclei, giving

$$H = (H)_0 + \sum_k \left(\frac{\partial H}{\partial Q_k}\right)_0 Q_k + \frac{1}{2}\sum_{k,l}\left(\frac{\partial^2 H}{\partial Q_k \partial Q_l}\right)_0 Q_k Q_l + \ \ldots \qquad \text{(eq 3.2)}$$

keeping only the linear terms and using the definition for the quantum mechanical transition, the above is written

$$[H]_{ij} = (H)_0 \langle \Phi_i | \hat{\mathbf{I}} | \Phi_j \rangle + \sum_k \left(\frac{\partial H}{\partial Q_k}\right)_0 \langle \Phi_i | Q_k | \Phi_j \rangle \qquad \text{(eq. 3.3)}$$

It should be noted that the normal coordinate Q_k can always be related to the Cartesian coordinate system through a transformation: $Q_k = \sum_{i=1}^{3N} l_{ik}\tilde{d}_i$ where the index runs over the expected 3N Cartesian coordinates for N atomic centers, while $\tilde{d}_i$ represents the mass-weighted Cartesian coordinates and l_{ik} are the coefficients of the coordinate transformation matrix [127]. This representation is used for convenience, bypassing the need for many equations for each Cartesian component. Within the harmonic approximation, the vibrational wavefunctions are represented by the product of harmonic oscillators associated with the normal coordinates Q_k in the vibrational quantum number v_k^i state such that

$$\Phi_i = \prod_k \Phi_{v_k^i}(Q_k) \qquad \text{(eq. 3.4)}$$

From this general consideration, the vibrational transition selection rules can be determined straightforwardly by the properties of the quantum harmonic oscillator, giving

$$\left\langle \Phi_{v_k^i}(Q_k) \middle| \Phi_{v_k^j}(Q_k) \right\rangle = \begin{cases} 0 \text{ for } v_k^i \neq v_k^j \\ 1 \text{ for } v_k^i = v_k^j \end{cases} \qquad \text{(eq. 3.5)}$$

and

$$\left\langle \Phi_{v_k^i}(Q_k) \middle| Q_k \middle| \Phi_{v_k^j}(Q_k) \right\rangle = \begin{cases} 0 \text{ for } v_k^i = v_k^j \\ \sqrt{v_k^j + 1}\, c_{v_k} \text{ for } v_k^i = v_k^j + 1 \\ \sqrt{v_k^j}\, c_{v_k} \text{ for } v_k^i = v_k^j - 1 \end{cases} \qquad \text{(eq. 3.6)}$$

with

$$c_{v_k} = \sqrt{\frac{\hbar}{4\pi v_k}} \qquad \text{(eq. 3.7)}$$

Importantly, this leads to two general selection rules. First, the gross selection rule $\left(\frac{\partial H}{\partial Q_k}\right)_0$ terms must be non-zero, requiring the involvement of the normal coordinate in the excitation event. The quantum transition selection rules arise from the terms $\left\langle \Phi_{v_k^i}(Q_k) \middle| \Phi_{v_k^j}(Q_k) \right\rangle$ and

$\left\langle \Phi_{v_k^i}(Q_k) \middle| Q_k \middle| \Phi_{v_k^j}(Q_k) \right\rangle$. The latter term shows that only discreet transitions of $v_k^j \pm 1$ are allowed for any vibrational excitation. The realization of these transitions differ for IR and Raman excitation events as they are governed by different physical processes, and thus different excitation operators *H*. How each of these operators transforms with respect to a coordinate system also dictates which modes are active in either spectroscopic technique, as discussed below.

3.2.2. Symmetry Selection

In addition to the transition selection rules, symmetry selection rules greatly simplify the prediction of vibrational properties of molecules [128]. Molecular structures can be described in terms of a set of spatial operations on nuclear centers that, after application, produce an exact copy of the molecule or material fragment (such as a unit-cell for crystal lattices). Large and highly disordered molecules (like proteins) typically lack these simple rules, where only an "identity" operation – the equivalent of multiplying all atomic coordinates by one – leaves the structure unchanged. For high-symmetry species, an assignment of a so-called "point-group" can be made. This group contains a set of symmetry operations (reflections, translations, rotations), and "irreducible-representations", which are the fundamental symmetry elements composing the point-group. For example, the TCNE molecule belongs to the D_{2h} point group. The character table of this point group is listed below [129].

Table 3.1. Symmetry character table for the D_{2h} point group.

D_{2h}	E	C_2 (z)	C_2 (y)	C_2 (x)	i	σ (xy)	σ (xz)	σ (yz)	linear, rotations	quadratic
A_g	1	1	1	1	1	1	1	1		x^2, y^2, z^2
B_{1g}	1	1	-1	-1	1	1	-1	-1	R_z	xy
B_{2g}	1	-1	1	-1	1	-1	1	-1	R_y	xz
B_{3g}	1	-1	-1	1	1	-1	-1	1	R_x	yz
A_u	1	1	1	1	-1	-1	-1	-1		
B_{1u}	1	1	-1	-1	-1	-1	1	1	z	
B_{2u}	1	-1	1	-1	-1	1	-1	1	y	
B_{3u}	1	-1	-1	1	-1	1	1	-1	x	

Within a molecule of a specific point-group and neglecting anhomonicity, the only accessible vibrational modes are those whose symmetries match those of the irreducible representations within that group. These symmetries are found along the leftmost column. Thus, seven symmetries are possible for any vibrational wavefunction from a D_{2h}-type molecule (excluding the "quiet" A_u mode, vide infra). The various symmetry operations of a point-group are listed in the top row. The final columns illustrate how the irreducible representations transform along the Cartesian coordinate system. The values in the table body illustrate how an object acted upon by a given symmetry operation behaves with respect to that action; symmetric (1) or anti-symmetric (-1) behavior is expected from this point group for any reflection, translation, or rotational operation.

Recalling the integral from above

$$\langle \Phi_i | H | \Phi_j \rangle \qquad \text{(eq. 3.8)}$$

it contains three elements: the excited vibrational state Φ_i, the operator H, and the ground vibrational state Φ_j, each with a symmetry possible from the irreducible representation of the

molecular point group. For the integral to be non-zero, it can be stated that the direct product of the symmetry elements

$$\Gamma_{\Phi_i} \otimes \Gamma_H \otimes \Gamma_{\Phi_j} \quad \text{(eq. 3.9)}$$

must be of a totally-symmetric type (typically listed by A_g or A_{1g}) [130]. For vibrational modes, the Γ_H symmetry transforms according to the components of the excitation operator H. For vector operators, these are the canonical Cartesian components (x, y, z). For tensor operators of rank two, these are the components α_{lm} (l,m = x, y, z). From the character table above, the modes transforming along the x, y, and z coordinates are the B_{1u}, B_{2u}, and B_{3u} modes, respectively. These modes are active in excitations that involve perturbation along these coordinates alone. Similarly the A_g, B_{1g}, B_{2g} and B_{3g} modes respond to excitations that transform along multiple coordinates axes (l,m = x, y, z). The following illustrates the physical processes distinguishing the vector-operator and tensor-operator vibrational modes.

3.2.3. Infrared Absorption

A vibrational transition may be considered through the dipole moment operator defined by

$$\mu_g = \sum_h q_h d_h \quad \text{(eq. 3.10)}$$

where d is a distance from the molecule center of mass and q is an effective charge on the h^{th} atomic fragment of the molecule. In Cartesian coordinates, the index sums over the typical components (g = x, y, z). The intensity of the IR transition can be related to the spatial dipole moment through the magnitude of its vector components

$$I_{ij} \propto [\mu_x]_{ij}^2 + [\mu_y]_{ij}^2 + [\mu_z]_{ij}^2 \quad \text{(eq. 3.11)}$$

where the transition between the i^{th} to j^{th} vibration level is component-wise considered and averaged over all molecule orientations. From this definition, it is clear that a dipole moment must exist for an IR active mode to have a nonzero intensity. By applying substitution of $H \rightarrow \hat{\mu}$ in eq. 3.3, the gross selection rule becomes $\left(\frac{\partial \mu}{\partial Q_k}\right)_0 \neq 0$ illustrating the requirement for a change in dipole moment with respect to normal (or Cartesian) coordinate for this transition to occur. The term $\left\langle \Phi_{v_k^i}(Q_k) \middle| \Phi_{v_k^j}(Q_k) \right\rangle$ must also be considered. This term is always zero for IR transitions due to the change in vibrational quantum number $v_k^i \neq v_k^j$ for a discreet vibrational excitation event. It is also clear from eq. 3.11 that the dipole operator is a vector with components in the canonical Cartesian coordinates. It is therefore expected that this operator will cause vibrations whose symmetry transforms along x, y, or z coordinates, such as the B_{1u}, B_{2u}, and B_{3u} modes from the D_{2h} point group above. These modes then are said to be "IR active".

3.2.4. Raman Scattering

In contrast to the infrared transitions, the Raman scattering occurs through the perturbation of the polarizability field of a material by an electric field E. The dipole moment neglecting a constant and higher-order terms can be written

$$\boldsymbol{\mu} \approx \alpha \bullet \mathbf{E} \qquad \text{(eq. 3.12)}$$

where α is the polarizability tensor. Relating the leading term to the dipole vector components gives

$$\begin{bmatrix} \mu_x \\ \mu_y \\ \mu_z \end{bmatrix} = \begin{bmatrix} \alpha_{xx} & \alpha_{xy} & \alpha_{xz} \\ \alpha_{yx} & \alpha_{yy} & \alpha_{yz} \\ \alpha_{zx} & \alpha_{zy} & \alpha_{zz} \end{bmatrix} \bullet \begin{bmatrix} E_x \\ E_y \\ E_z \end{bmatrix} \qquad \text{(eq. 3.13)}$$

and corresponding transition integral $\langle \Phi_i | \hat{\alpha} | \Phi_j \rangle$ with

$$[\alpha_{lm}]_{ij} = (\alpha)_0\langle\Phi_i|\hat{\mathbf{I}}|\Phi_j\rangle + \sum_k \left(\frac{\partial\alpha_{lm}}{\partial Q_k}\right)_0 \langle\Phi_i|Q_k|\Phi_j\rangle \quad \text{(eq. 3.14)}$$

and

$$I_{ij} \propto [\alpha_{lm}]_{ij}^2 \quad \text{(eq. 3.15)}$$

Again the gross selection rule illustrates the change in polarizability required for a transition event, $\left(\frac{\partial\alpha_{lm}}{\partial Q_k}\right)_0 \neq 0$. In the Raman process, the initial excitation does not occur strictly between vibrational levels as it does in the IR method. Therefore, unlike in IR absorption events, the leading term from eq. 3.14 $\langle\Phi_i|\hat{\mathbf{I}}|\Phi_j\rangle$ does not always become zero. Here, there is no change in vibrational levels after excitation, meaning that the scattered photon returns the excited body into the same vibrational energy level it excited from, with no momentum transfer. This is called Releigh scattering, and it may always be present in the Raman process. The term $\langle\Phi_i|Q_k|\Phi_j\rangle$ again defines the selection rules for the vibrational excitation. After exciting into the virtual states through shifts in the polarizability field, the system returns with $v_k^i = v_k^j \pm 1$. The $v_k^i = v_k^j + 1$ solution describes the "Stokes" scattering event, where the scattered photon is shifted downward in energy concomitant with the energy transfer to the material resulting in an excited vibrational state. Similarly, the $v_k^i = v_k^j - 1$ solution describes the "anti-Stokes" scattering, where an excited vibrational state transfers energy to the scattered photon and the system is relaxed to the ground vibrational state.

In general, the Stokes line will be stronger than the anti-Stokes line under ambient conditions, since to observe the latter a large portion of the excited vibrational states must be thermally populated. See Fig. 3.1 for illustration of these processes. Finally, since the polarizability tensor transforms with two spatial components (*l*,*m* = x, y, z), from the character table and rules discussion above, it can be defined that those symmetry modes whose

representations transform to second-order in the Cartesian coordinates are Raman active. For the D_{2h} example above, those modes are the A_g, B_{1g}, B_{2g}, and B_{3g} ones.

3.3. Spectroscopic Instrumentation and Sample Preparation

3.3.1. Fourier Transform Infrared Spectroscopy

The FTIR (Fourier transform infrared spectroscopy) technique provides the ability to rapidly acquire vibrational absorption spectra across a broad range of frequencies through interferometry, in contrast to using dispersive element to scan wavelengths in a discreet fashion. The interferogram is created by a modified Michelson Interferometer, where a beam splitter transmits 50% of a polychromatic beam intensity to both a stationary and moving mirror, each lying perpendicular to one another at a distance L from the beam splitter. The displacement of the non-stationary mirror by Δx creates a constructive/destructive interference at different frequencies in the recombined beam due to the difference in optical path length $L+\Delta x$ between the original and reflected beams. The full spectrum from the polyatomic source is thus modified by the moving mirror and sent through the sample, creating a new set of broadband spectra for each mirror position. Each of these unique spectra individually possess the sample absorption information. The resulting spectrum is the interferogram I(x,ν), where x is the sliding mirror positon and ν is the wavenumber related to the light frequency by $\nu = 1/\lambda$ (Fig. 3.2). Generally, it can be related to the frequency information $S(\nu)$ it contains by

$$I(\Delta x) = S(\nu)[1 + cos(2\pi\nu\Delta x)] \qquad \text{(eq. 3.16)}$$

where the trigonometric term describes the constructive and destructive interference properties and $S(\nu)$ is a constant that depends only on frequency [131]. A discreet Fourier transform of this interferogram allows the frequency function to be resolved in order to

reconstruct the full spectrum. This creates two significant advantages. First, instead of using a monochromatic light source and modifying the grating period of a dispersive element to obtain individual frequencies, a large number of frequencies are collected for each data point in the FTIR spectrum. This is known as the multiplex- or Fellgett-advantage [132]. A multiplexed measurement will have a significant signal to noise ratio improvement over one where a scanning dispersive element is utilized. Multiplex approaches disperse measurement noise over all frequencies of a given scan. Second, rapid data acquisition is achieved through high-speed motion of the interferometer mirror, enabling high measurement throughput.

Infrared spectroscopy was performed with a Bruker Vertex 70 FTIR spectrometer. The spectrometer was equipped with a nitrogen purging valve joined to the sample chamber to reduce atmospheric contamination by CO_2 and H_2O. A step-scan interferometer, extended range (10,000 - 450 cm^{-1}) KBr beam splitter, and cryogenic liquid nitrogen cooled mercury cadmium telluride detector (wide band, 400 cm^{-1} cutoff, a.k.a. “MCT-B”) were installed [21]. Spectral scans were performed between 450cm^{-1} and 4000 cm^{-1}. Initial background measurements are performed after purging the sample cavity. These backgrounds are subtracted from the final scans. Spectra possess peak positon error of less than ~1 cm^{-1}. Samples were prepared by a press-pellet method in inert atmosphere, where a small amount of sample is gently ground into a spectroscopic grade KBr powder with mortar and pestle, after which the powder/sample matrix loaded into a disk-like collar and mechanically compressed between two stainless steel anvils. To maintain material integrity and prevent atmospheric oxidation or hydration, samples were transported under nitrogen blanket between the inert synthesis glovebox and purged sample chamber of the Vertex 70.

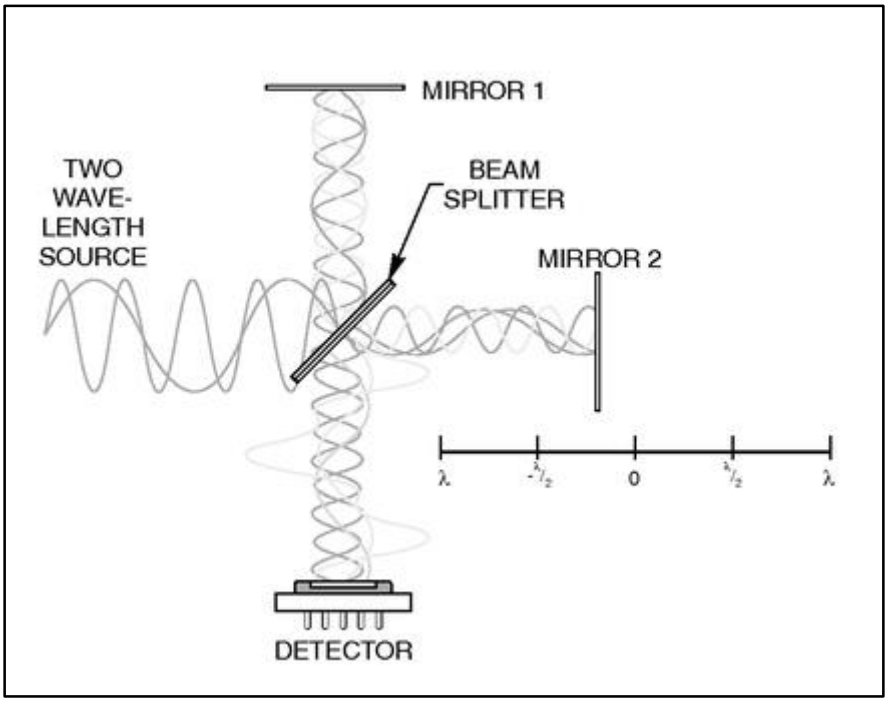

Figure 3.2. Schematic of infrared interferometer operation and geometry.

3.3.2. Confocal Raman Microscopy

Confocal Raman spectroscopy is a powerful and easy to use technique that couples a coherent excitation source, CCD detector, and dispersive gratings or optics to elements of an optical microscope. The integration of microscopy capabilities with the Raman spectrometer allows for extremely high spatial resolution of sampled area via the microscope objective imaging power. Selection of microscopic excitation points within a sample provides flexibility to find locations that may have the strongest response, as well as enabling sample surface profiling, useful especially for thin-film samples. In addition to x-y scanning, depth profiling in the z direction may be achieved by adjusting the focal plane of the objective optics within a sample volume [133]. The schematic principle of confocal Raman operation is shown in Fig. 3.3 [134]. The illustration contains the key elements of the basic device: the excitation source, the beam splitter, the photodetector, and the pinhole apertures. Scattered Raman signal from the focal

plane enters the pinhole aperture and is typically sent to a dispersive grating element or lens and projected onto a CCD detector. This is schematically shown in the center illustration of Fig. 3.3

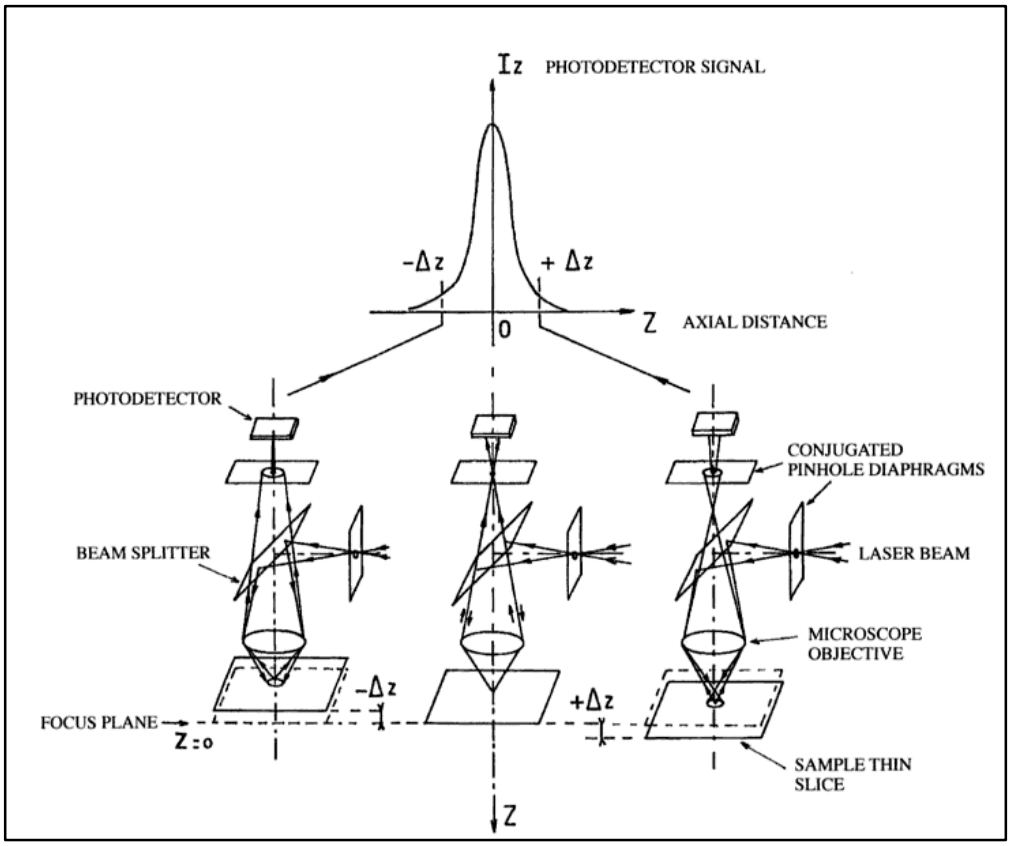

Figure 3.3. Schematic of confocal Raman microscopy instrumentation and operation principles.

However, out of plane scattering will occur if the excitation volume extends outside of the focal volume, an effect which is always present. Above and below focal plane scattering is illustrated in the leftmost and rightmost illustration respectively. Here, the crucial role of the pinhole aperture is noted, as it rejects scattering events that lie outside of the focal plane. The topmost illustration shows the relative intensities of the correspondent spatial excitations as they arrive at the photodetector or dispersive element.

Confocal Raman spectroscopy was performed using a LabRAM Aramis Horiba Jobin Yvon Confocal Raman Microscope equipped with a CCD detector, utilizing 532 and 785 nm

coherent excitation sources. The spectra were obtained in the 400-3500 cm^{-1} spectral range with ~1 cm^{-1} resolution. To avoid air exposure and oxidation of the sample materials, the polycrystalline powders were prepared inside the N_2 glove box and placed inside a ring of degassed high-vacuum grease on a microscope slide. A second slide was placed over the grease ring, sealing the sample from external atmosphere upon sample transport. The sample configuration is shown in Fig. 3.4.

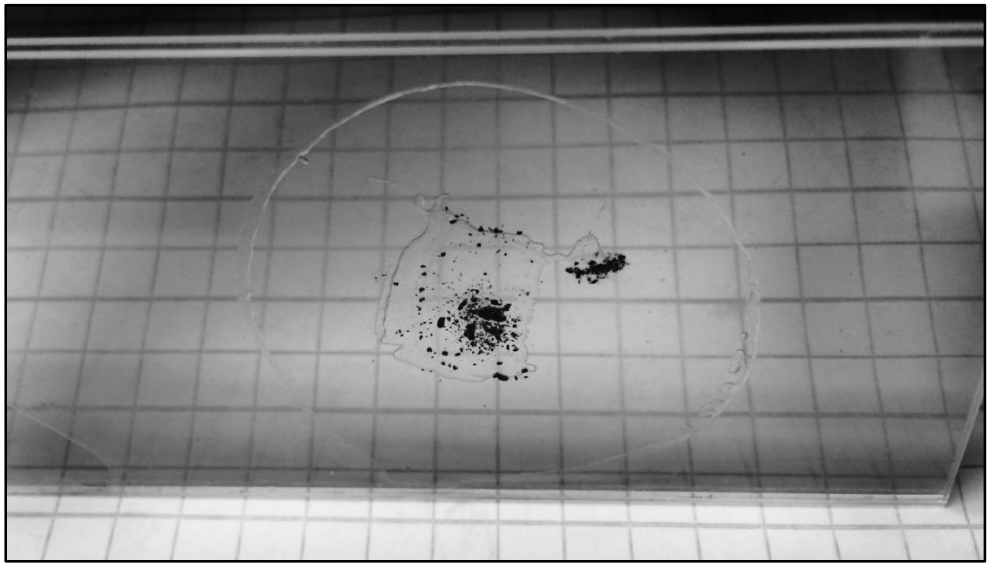

Figure 3.4. Air-free sample preparation for confocal Raman microscopy.

3.4. Magnetometry

3.4.1. Instrumentation and Measurement Principles

Measurement of intrinsic magnetic material response properties as a function of applied external magnetic field and temperature allows the determination of a wide range of responses useful for sample characterization. Critical behavior at or near the thermodynamic magnetic ordering transition reveals a wealth of information regarding spin coupling strength, dimensionality, order, and dynamics. In addition, paramagnetic spin composition may be

assessed through summation of spin-bearing species' moment values far from the magnetic transition (if present). Primarily, molar magnetic susceptibility χ (static: ~M/H, dynamic: $\sim\partial M/\partial H$, where M – magnetization, H – external magnetic field) and molar magnetization M in a variety of measurement protocols are needed to fully investigate a sample's behavior. Static or "DC" measurement protocols evaluate magnetization through induction due to sample motion, while dynamic "AC" measurements probe in-phase and out-of-phase response properties as a weak magnetic field is dynamically oscillated across the sample. A Quantum Design Physical Property Measurement System (PPMS) equipped with a 9 Tesla superconducting magnet and ACMS coil set was used to perform all magnetic measurements. The ACMS detection coils allow the subsequent execution of AC and DC measurements without equipment change. The ACMS detection coil schematic is shown in Fig. 5a, and the full PPMS dewar setup with the ACMS hardware installed is illustrated in Fig. 5b.

The ACMS coil set sits concentrically within the PPMS superconducting magnet and provides a dynamic field of up to 15 Oe at frequencies ω = 10-10,000 Hz [19].

To perform AC susceptibility measurement, a material is centered in the sample volume near one of two detection coil sets of opposite polarity (+/-), and the drive coil is pulsed producing a transient magnetic field. A digital signal processor evaluates the voltage induced within the detection coils by dynamic magnetization $\partial M \sim \partial H \chi_{AC}$ of the sample for a finite period following field pulsing. This process is repeated multiple times to construct an average dynamic susceptibility response profile. An identical measurement is performed in each pole of the two detection coils and finally within the calibration coil set. The waveforms defined by the driving field pulse and the dynamic magnetization response measured following the pulse are subtracted to extract the in-phase (χ') and out-of-phase (χ'') magnetic susceptibility $\chi_{AC} = \chi' - i\chi''$.

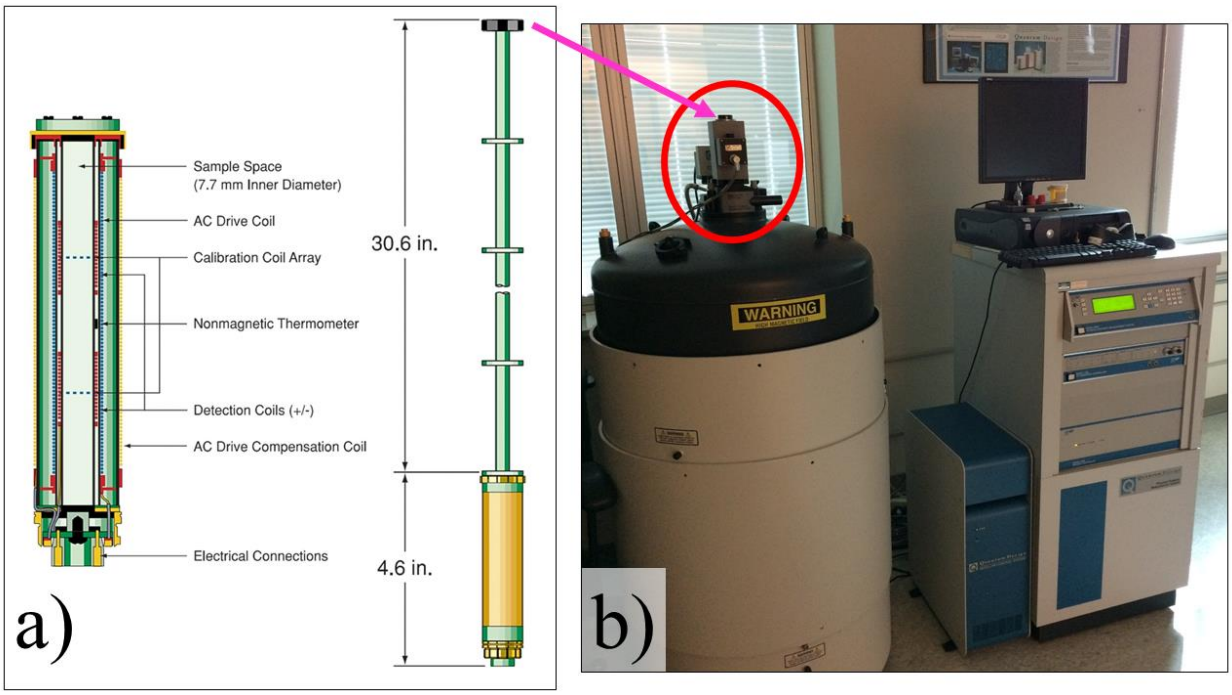

Figure 3.5. Schematic of ACMS detection/drive coil insert (a) and full PPMS+ACMS experimental setup (b).

In contrast to AC methods, DC mode measurement directly measures the magnetization of a sample. DC magnetization measurement is based on Faraday's law of induction. It is evaluated within the ACMS by recording the amplitude of current induced in the detection coil by the moving magnetic field produced by a sample's magnetic moment. A DC servo motor moves a magnetized sample at a rate of ~100 cm/sec through the set of detection coils repeatedly, producing an accurate, low-noise magnetization measurement. This approach is commonly denoted "extraction magnetometry" [135].

3.4.2. Sample Preparation

Similar to the sample-preparation for spectroscopic characterization discussed above, the air-sensitive nature of magnetic M^{II}[TCNE] powders requires the application air-free techniques

to magnetometry. The air-free sample holders used for PPMS characterization and illustration for sample loading is shown in Fig. 3.6.

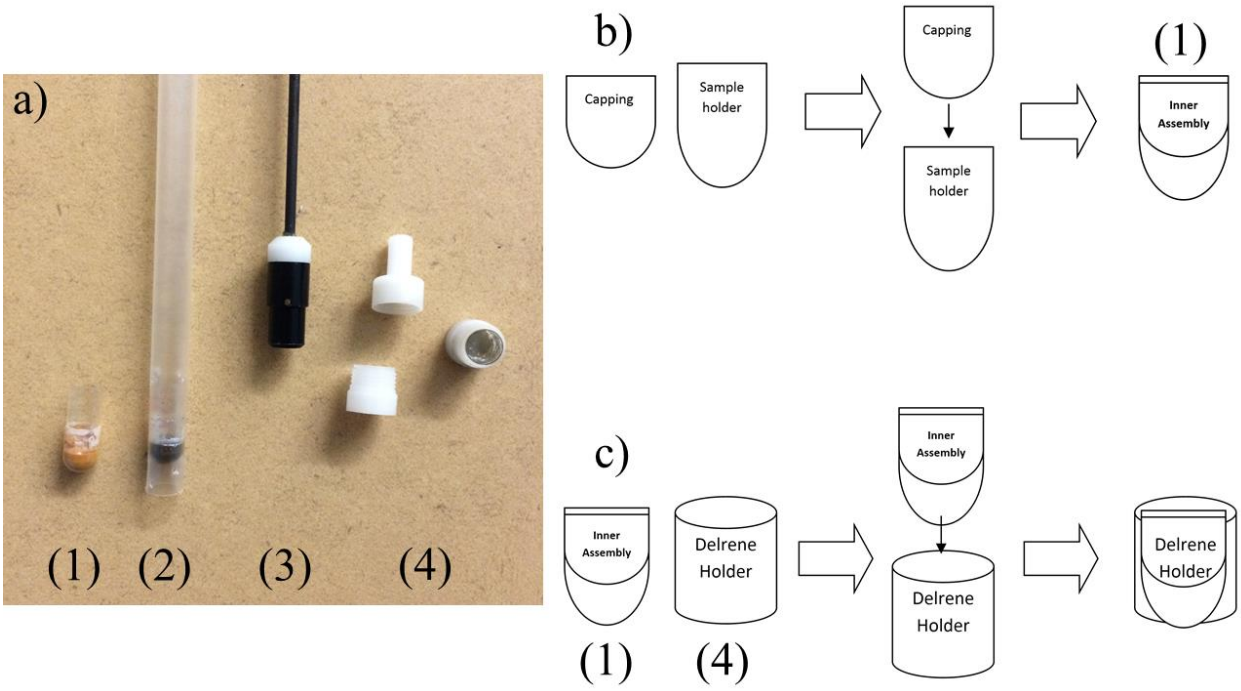

Figure 3.6. Air-free magnetometry samples (a, 1-4) and and sample holder assembly diagrams (b, c).

Within a nitrogen dry box, magnetic powders are carefully loaded and weighed in gel-cap holders (Fig. 3.6a, 1). After weighing into the long end of the gel-cap, the short end is rimmed with degassed grease previously held at -40 atm. for ~48 hours. The short end is inserted into the long sample holding side to complete assembly, illustrated in Fig. 3.6b. The gel-cap is subsequently loaded into a straw of calibrated length, which is perforated to prevent sample slippage (Fig. 3.6a, 2). Finally, straw/gel-cap assembly attached to a holding rod and inserted into the PPMS-ACMS sample-holding sleeve. The PPMS-ACMS sample volume is subsequently purge-cycled to remove all remnant atmosphere. Exquisitely air-sensitive samples (such as V^{II}[TCNE] materials) require extra consideration. For these samples, the straw method will not provide sufficient atmospheric protection during transport. Within the nitrogen glovebox, the V^{II}

samples are loaded into the gel-cap as described above, and the sealed gel-caps subsequently loaded into delrin buckets (Fig. 3.6a, 4). The threads of the delrin bucket are greased, and the top holder is joined to the bucket. The greased outer thread of the assembled delrin bucket is then wrapped with teflon tape. This process is illustrated in Fig. 3.6c. The sample is transported under nitrogen to the PPMS sample volume, where the bucket assembly is attached to the sample rod under a positive pressure nitrogen blanket, and rod-bucket assembly is inserted into the PPMS-ACMS and subsequently purged.

3.4.3. Magnetometry: Measurement Protocols

In this work, several magnetometric measurement schemes were used to evaluate material properties. These protocols are detailed in the following.

- $\chi(T)$ (Static - DC) − Measurement of sample molar static susceptibility (emu/mol) as a function of temperature with a small ~kOe magnetic field applied. This allows for two modes of analysis:
    - Determination of the Weiss temperature constant θ (K) from the linear extrapolation of the relation $1/\chi(T) \propto (T-\theta)$ typically taken at $T > T_c$ and illustrates the mode of remnant spin coupling present, if any, in the high-temperature limit ($\theta < 0$ – antiferromagnetic, $\theta = 0$ – ideal paramagnet, $\theta > 0$ – ferromagnetic) [136].
    - Determination of the Curie constant $\chi T(T) = C$ (emu K/mol) $\approx 0.125 g^2 \sum_i S_i(S_i + 1)$; in the paramagnetic limit $T > T_c$ this value nominally represents the spin-only values of the magnetic species possessing spin S_i [137]. Deviations from this value suggest gyromagnetic ratio g ≠ ~2.00 (common for anisotropic transition

metals in octahedral ligand field [40]), the persistence of weak short-range spin-coupling, or paramagnetic impurity.

- *M(T)* − Magnetization as a function of temperature is studied in three distinct regimes: field cooled (FC), zero-field cooled (ZFC), and remnant (r) type measurements are considered. These measurements combined reveal information about the thermal demagnetization properties, as well as irreversibility/disorder characteristics of the magnetic transition.
    - $M(T)_{ZFC}$ − The sample is warmed above critical temperature, and cooled slowly to ~2 K in a carefully calibrated zero field environment. A small field ~50 Oe (or field greater than coercively of the magnet) is subsequently applied, and the magnetization is measured upon warming to room temperature.
    - $M(T)_{FC}$ − With the ~50 Oe (or greater) external field still applied, the magnetization is measured upon cooling through the magnetic transition. A bifurcation at the point of maximum magnetization reveals an irreversibility in the spontaneous magnetic order, either due to the presence of significant frozen spin disorder or domain wall pinning below the transition, or the propagation of spontaneous moment in three dimensions with direction along the applied field upon cooling through the transition.
    - $M(T)_r$ − The magnetic material is warmed above the transition temperature and an external field greater than the coercive magnetization field of the sample is applied. The sample material is cooled through the transition to ~2 K and the magnetization is measured as a function of temperature upon warming after

removing the external field. The intercept of the leading edge slope of this curve with the temperature axis represents the critical temperature.

- *M(T,H)* − Variation of magnetic field while measuring the total moment reveals information about the nature of the spin ordering and anisotropy present in the sample. Two protocols are used:
    - *M(T,H_{hist})* − The sample is cooled well below T_c and the magnetization is measured as a function of external magnetic field, cycled between +H and –H. This reveals hysteretic behavior of the collective magnetic moment and coercive and remnant magnetization values may be extracted.
    - *M(T,H_{sat})* − Far below T_c, the magnetization is probed as a function of applied field (with H_{max} between 6-9 T). Saturation is observed when the slope of magnetization in the high field limit approaches zero. The saturation magnetization is the Briolloun function in the high-field limit, with value $M_s = Ng\mu_B S_{eff} \approx 1.117*10^4 S_{eff}$ (emu Oe/mol) where S_{eff} is the effective spin in the magnetically ordered state of the material [138]. For example, ferrimagnetically coupled high spin Mn^{II} (S = 5/2) to the $TCNE^{\bullet-}$ radical (S = 1/2) in the $[Mn^{II}(TCNE)(NCMe)_2]SbF_6$ magnet gives ($5/2 - 1/2 = S_{eff} = 2$).
- *M(t)* − Isothermal magnetic remanence is a useful measurement protocol to examine the slow spin relaxation dynamics of a disordered magnet. Here, a sample is field cooled through the spin-glass transition and held for a wait time t_w. With the temperature constant, the magnetic field is switched off at t_i and total magnetization is measured as a function of time *t* until a significant portion of the remnant magnetization has dissipated

at t_f. Fitting of this curve reveals characteristic spin relaxation times useful in characterizing spin-glasses below the disorder transition temperature.

- $\chi(T, \omega)$ (Dynamic) − AC susceptometry allows the dynamic or time-dependent electron spin response properties of a magnetic material to be probed with an oscillating magnetic field in a broad range of frequencies ω across a thermal span of interest *T*. The total dynamic magnetic response is given by the complex vector relation $\chi_{AC} = \chi' - i\chi''$
    - $\chi'(T,\omega)$ − The portion of the dynamic susceptibility which follows the driving field with zero phase lag ($\theta = 0$). This quantity is related to the slope of the static susceptibility when the frequency of the driving field approaches zero.
    - $\chi''(T,\omega)$ − The portion of the dynamic susceptibility which lags behind the driving field with a relative phase shift of $\theta = \pi/2$. This quantity reveals dissipative processes within the sample, and is highly sensitive to thermodynamic phase changes.

3.5. Computaitional DFT Modeling

As discussed in Chapter 2, the simulation of electronic and magnetic properties by utilizing density functional theory (DFT) is widely used for description of magnetic and electronic properties of M[TCNE] materials. When performing a DFT simulation on a chemical structure, one essentially solves the so-called Kohn-Sham equations self-consistently for a given spatial configuration of electrons, corresponding to a unique electron density. Two main considerations have a significant impact upon the quality of the solution obtained: a so-called "density functional" must be chosen which will properly account for the nature of electron-electron exchange and correlation effects, and the mathematical form of the basis functions by which the single-electron Kohn-Sham orbitals are expanded.

For M[TCNE] materials, basis functions must spatially account for topologically simple organic p orbitals, the relatively complex features of the highly localized transition metal 3d orbitals, as well as any molecular orbital hybrids that may form from their interaction. Localized basis sets based on a linear combination of atomic orbitals are a convenient choice for describing the density profiles of molecules or selected fragments of larger crystal structures due the their simplicity and significant flexibility. Slater-type orbitals (STOs) mimic the eigenfunctions of the hydrogen atom closely and are a natural choice for the atomic basis functions, but are numerically difficult to evaluate. Linear combinations of Gaussian-type orbitals (GTOs), however, provide a good approximation of STOs and their numerical evaluation is highly efficient. Localized basis functions built from GTOs possess additional flexibility in that one has the choice to assign the number of basis functions included per atomic orbital, as well as the possibility to add diffuse and polarization functions, according to chemical intuition. Recent simulations on reduced [Mn(TPP)][TCNE] model systems have suggested only weak dependence of magnetic exchange constants on basis set size, once polarization functions were included [88], however, and were most significantly impacted by choice of functional.

For the DFT simulation of full crystal structures utilizing periodic boundary conditions, basis functions that resemble electronic waves subject to periodic potentials are the natural choice. Plane-wave basis functions that exhibit the same periodicity of the crystal lattice are often chosen to solve the Kohn-Sham equations in these instances [139]. However, this basis contains a considerable drawback: recreation of rapid spatial variation of orbitals near nuclei, as is found in covalent bonds or highly localized 3d orbitals, requires a large number of high-frequency plane waves. This problem is worsened by the orthogonality requirements between valence and core electrons, which itself creates rapid fluctuation of valence orbitals near nuclei,

further increasing the demands for large numbers of high frequency plane-wave basis functions and reducing computational efficiency. This drawback can be overcome by the use of pseudopotentials, which screen out the core effects on valence electrons, smoothing out their behavior in a small radius close to the nuclei [140]. The total energy of a system modeled with a plane wave basis will rapidly converge with increasing the energy cutoff, and thus the number of plane-waves used. In magnetic systems, spin coupling constants are commonly evaluated via minute energy deltas between the allowed spin configurations of the system under study. Thus, a properly converged calculation obtained by a sufficiently large plane-wave energy cutoff is crucial to extract information about magnetic behavior within periodic systems modeled with plane-wave basis sets.

Beyond the basis set choice, the nature of the density functional itself is expected to have the largest impact on the electronic and magnetic structures of a DFT model system. The M^{II}[TCNE] MBM remains a very challenging electronic system to simulate, due to the presence of partially occupied *d*-orbitals of the transition metals, which similarly to transition metal oxides results in significant correlation effects and a variety of spin configurations in a limited energy region [141,142]. As was shown in the literature [143,144] and discussed in Chapter 2, the implementation DFT hybrid functionals (e.g., B3LYP or PBE0) in electronic structure modeling affords much better prediction of band gaps and magnetic properties of M[TCNE] than standard local or semilocal approximations to the exchange-correlation (XC) energy, such as LSDA and GGA functionals, or even LSDA+*U*, where the Hubbard repulsion term *U* has to be empirically tuned for a specific compound [145]. The success of hybrid functionals originates from reductions in the self-interaction error otherwise present in either LDA or GGA, which is most important in describing the electronic structure of narrow band and/or localized open shell

systems. However, short-range qualities in a system may have different requirements on the theoretical methods than long-range features. In fact, in metallic systems, the nonlocal exchange interaction has an unphysical and extremely slow spatial decay [146] as incorrectly described by common hybrid functionals [147]. For MBMs, the magnetic coupling is a very important property, while it is extremely sensitive to electron correlation effects [148].

While standard hybrid functionals typically provide a significant improvement in values of magnetic couplings over GGA and LDA approaches to many molecular systems, they often overestimate these values as compared to experimental data [147]. To this end, screened exchange functionals, or the range-separated type, have been shown to overcome limitations of standard hybrid functionals, as they smooth out the inconvenient physical/numerical behavior of the exact exchange in a given range by varying amounts of Hartree-Fock exchange for short-range and long-range interactions [149]. Tested for a broad set of organic diradicals and transition metal dinuclear complexes for which accurate experimental data are available, it was shown that both short-range corrected HSE and long-range corrected LC-wPBE range-separated hybrid functionals provide a significant improvement in estimating magnetic couplings, as compared to standard hybrids such as the well-known B3LYP [147]. Since HSE was developed with periodic systems in mind, for the present study of the Mn[TCNE] crystals the range-separated hybrid exchange-correlation (XC) functional HSE06 [150] is implemented, in which a fractional portion of the short-range Perdew-Burke-Ernzerhof (PBE) functional is replaced by the same amount of an exact HF exchange according to the construction

$$E_{XC}^{HSE} = \alpha E_X^{HF,S}(\omega) + (1-\alpha)E_X^{PBE,S}(\omega) + E_X^{PBE,L}(\omega) + E_C^{PBE} \qquad \text{(eq. 3.17)}$$

where ω is a parameter which controls the range-separation of electron-electron interaction between the short-range (S) and long-range (L) terms of the Coulomb kernel with a screening

parameter of $\omega = 0.10$ Å^{-1} and HF exchange portion $\alpha = 0.25$. This functional was utilized in the commercial software program VASP version 5.2.1, which was used to carry out all simulations of electronic and magnetic structure.

3.5.1. Computational Resources

All simulations were performed on Carver, a IBM iDataPlex system consisting of 1202 compute nodes with 32 Gb/s of point-to-point bandwidth. This computational system is housed at the National Energy Research Scientific Computing Center, a DOE Office of Science User Facility supported by the Office of Science of the U.S. Department of Energy under Contract No. DE-AC02-05CH11231.

3.6. Conclusion

Spectroscopic, magnetometric, and computational methods form the major components of characterization efforts in this work. These methods in turn are discussed in a combination of theoretical and practical contexts, illustrating basic material response phenomena, equipment principles of operation, sample creation and handling, and computational modeling considerations and approaches. This discussion clarifies and outlines the techniques applied in the following chapters.

4. MAGNETISM AND CHARGE TRANSFER IN NEW TWO-DIMENSIONAL M[TCNE] (M = Mn, Fe, Ni) MATERIALS

4.1. Introduction

The infrared spectroscopy of TCNE $\nu_{C\equiv N}$ stretching modes is widely used for characterization of the M[TCNE] class of magnets [151], [97]. However, the sign and magnitude of the $\nu_{C\equiv N}$ shift relies on a delicate balance between σ-type donation and π*-backbonding working in opposite directions, thus making correlation between the spectroscopic shift and magnetic exchange hard to identify. In contrast, the frequency of the Raman active totally symmetric $\nu_{C=C}$ stretching mode is solely dependent on the electron density on the anti-bonding π* orbital. Due to its significant spin-density distribution across the C=C double bond, π* charge transfer either toward the metal or ligand will strongly affect the C=C bond order, and thus vibrational energy. Hence, the electron density on the π* orbital (monitored via a shift of the $\nu_{C=C}$ mode with respect to its frequency in the TCNE free radical) could work as a measure of the metal-to-ligand charge transfer and, therefore, exchange interaction. While the vibrational spectra of neutral TCNE [152] as well as its anion-radical [153] were widely studied and the band assignment was proposed, the information about Raman response of TCNE complexes is limited to weak charge transfer [154] or π-dimerized [155] compounds.

Recently, the spectroscopic study of TCNE Raman response enhanced by the interaction with Cu surface was reported. The obtained spectra were assigned to the tricyanovinyl alcoholate, suggesting that the electrochemically generated TCNE anions were immediately oxidized [156].

In this report a systematic study of vibrational (both infrared and, for the first time, Raman)

properties of the family of new TCNE-based magnets of $[M^{II}(TCNE)(NCMe)_2]SbF_6$ (M = Mn (**1**), Fe (**2**), Ni (**3**)) composition in conjunction with their magnetic behavior is presented. The vibrational properties of the isolated $TCNE^{\bullet-}$ anion (in paramagnetic tetrabutylammonium tetracyanoethenide, $Bu_4N[TCNE]$) and recently characterized 2-D layered magnet $[Fe^{II}(TCNE)(NCMe)_2]FeCl_4$ (**4**) [81,157] are reported for comparison. The crystal structure of **1** and a powder x-ray diffraction pattern of **2** (found to be isostructural to **1)** is also reported. Comparison with the previously known structure of **4** [81,157] enables more rigorous interpretation of magnetic properties of the newly synthesized compounds (**1**-**3**). It is concluded that there is a linear correlation between the $\nu_{C=C}$ (a_g) frequency of the TCNE ligand and its formal charge Z, revealing that about 20% of π^* the electron density in all studied compounds is transferred to the metal ion.

4.2. Experimental Details

Preparation of compounds **1**-**3** was performed according to the synthesis procedures described below:

A total of 1 equiv of $Bu_4N[TCNE]$ dissolved in a minimum amount of CH_2Cl_2 was added to a stirred slurry of 1 equiv of $[M(NCMe)_6](SbF_6)_2$ (M = Mn, Fe, Ni) in CH_2Cl_2 in a nitrogen box. After stirring for 24 h, the precipitate was filtered, washed with CH_2Cl_2, and dried in vacuo for 2 h (95%). The results of elemental analysis for all studied materials are presented in the Table 4.1 Compound **4** was synthesized according to the procedure in [83].

Table 4.1. Elemental analysis of compounds **1-3**.

	$[Mn(TCNE)(MeCN)_{2.6}]SbF_6$ 0.40 CH_2Cl_2		$[Fe(TCNE)(MeCN)_{2.2}]SbF_6$		$[Ni(TCNE)(MeCN)_{2.8}]SbF_6$ 0.10 CH_2Cl_2	
	Calc.	**Found**	**Calc.**	**Found**	**Calc.**	**Found**
C	25.09	24.90	24.32	24.28	25.74	26.22
H	1.36	1.55	1.32	1.37	1.59	1.79
N	16.42	16.52	16.75	16.67	17.44	17.02

This simple metathesis synthetic route (chemical eq. 1) was chosen to avoid contamination from species with different oxidation states (metal or ligand related, in case of a redox route) that could alter the properties and complicate the analysis of the product material.

(1) $[M(NCMe)_6](SbF_6)_2 + Bu_4N[TCNE] \rightarrow [M(TCNE)(MeCN)_2]SbF_6$ (s) + $Bu_4N[SbF_6]$ + 4MeCN

The simplicity of this synthetic route also allows use of the same anion (SbF_6) for all compounds and thus allows the reactions to be carried out under identical conditions. All studies were performed on powder samples that were loaded, transferred, and measured in a drybox under inert conditions (<1 ppm H_2O and O_2). Elemental CNH analyses were performed on-site with a LECO CHNS-932 analyzer calibrated against sulfamethazine and ethylenediamine tetraacetic acid. The samples were loaded into tin capsules inside the drybox with each sample analyzed in triplicate to ensure an accurate determination.

Thermo-magnetic studies were completed with a Quantum Design (QD) Physical Properties Measurement System (PPMS) using the ACMS options for measurement of the magnetization and AC susceptibility as a function of applied field and temperature, as previously described [158]. Infrared spectra (400 to 4000 cm^{-1}) were obtained on a Bruker Vertex FT-IR spectrometer as KBr pellets or Nujol mulls. Unpolarised Raman spectra were obtained in 75-

3100 cm $^{-1}$ spectral range with ~1 cm^{-1} resolution using a LabRAM Aramis Horiba Jobin Yvon Confocal Raman Microscope equipped with a CCD utilizing 532 and 785 nm coherent excitation sources. A linear baseline was fitted directly to the corrected Raman spectra. To avoid air exposure, powder samples were placed between two glass slides glued inside the N_2 glove box. No changes due to oxidation were observed in the Raman spectra within ~30 min. To prevent decomposition due to overheating, the laser power was kept below 2 mW (×10 objective, ~20 μm diameter laser spot diameter).

A high-resolution synchrotron X-ray powder diffraction pattern of **1** was collected at the X16C beamline at the National Synchrotron Light Source at Brookhaven National Laboratory. X-rays of wavelength 0.6999 Å were selected using a Si(111) channel cut monochromator. After the sample, the diffracted beam was analyzed with a Ge(111) crystal and detected by a NaI scintillation counter. Wavelength and diffractometer zero were calibrated using a sample of NIST Standard Reference Material 1976, a sintered plate of Al_2O_3.

The X-rays (20.44keV, 0.6066 Å) available at the 1-BM beamline at the Advanced Photon Source at Argonne National Laboratory were used in combination with a Perkin-Elmer amorphous silicon area detector to record room temperature diffraction patterns for capillary-loaded samples of **1**, **2** and **4**. The raw images were processed using Fit-2D [159]. The sample-to-detector distance (800.679 mm) and tilt of the image plate relative to the beam were refined using a LaB_6 standard. Lattice parameters for **2** were determined by Le Bail analysis within GSAS.

4.3. Results and Discussion

4.3.1. Crystal Structure

All magnetic materials were synthesized as powder samples with varying degrees of crystallinity, and, therefore, identification of their crystal structures is a non-trivial task. The elemental analysis results fit well into the proposed formula $[M(TCNE)(NCMe)_2]SbF_6 \cdot xCH_2Cl_2$ *y*MeCN, where *x* and *y* vary for different compounds. IR spectroscopy confirms the presence of apically coordinated MeCN, as well as metal coordinated TCNE anions through the presence of two sets of $\nu_{C\equiv N}$ stretching modes of b_{1u} and b_{3u} symmetry (vide infra). When comparing representative XRD patterns for **1** and **2** with that for **4** (with a known 2-D structure), a resemblance is clearly observed (Fig. 4.1).

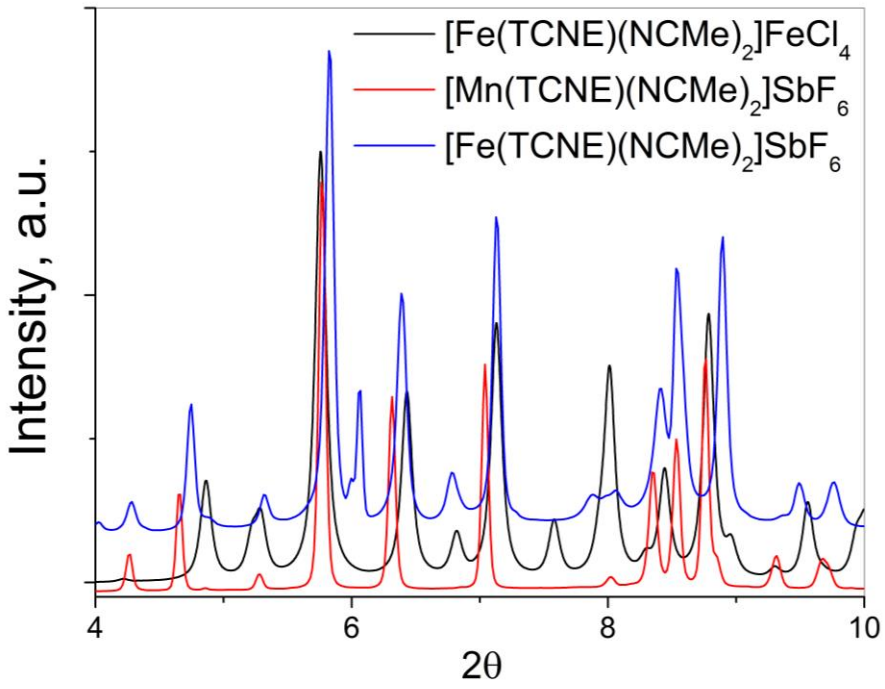

Figure 4.1. 2θ XRD patterns of the **1** (red), **2** (black), and **4** (blue) magnets.

The indexing of **1** was performed in TOPAS Academic. This indexing revealed an orthorhombic cell, with *a* =7.1924(2) Å, *b* =16.2938(5) Å and *c* =14.9429(4) Å. The crystal structure of **1** was determined, in *Cmcm*, with the use of charge flipping as implemented in Superflip. From this initial structure, TOPAS Academic was used to perform Rietveld refinements in order to improve the fits and refine bond lengths and angles, shown in Fig. 4.2.

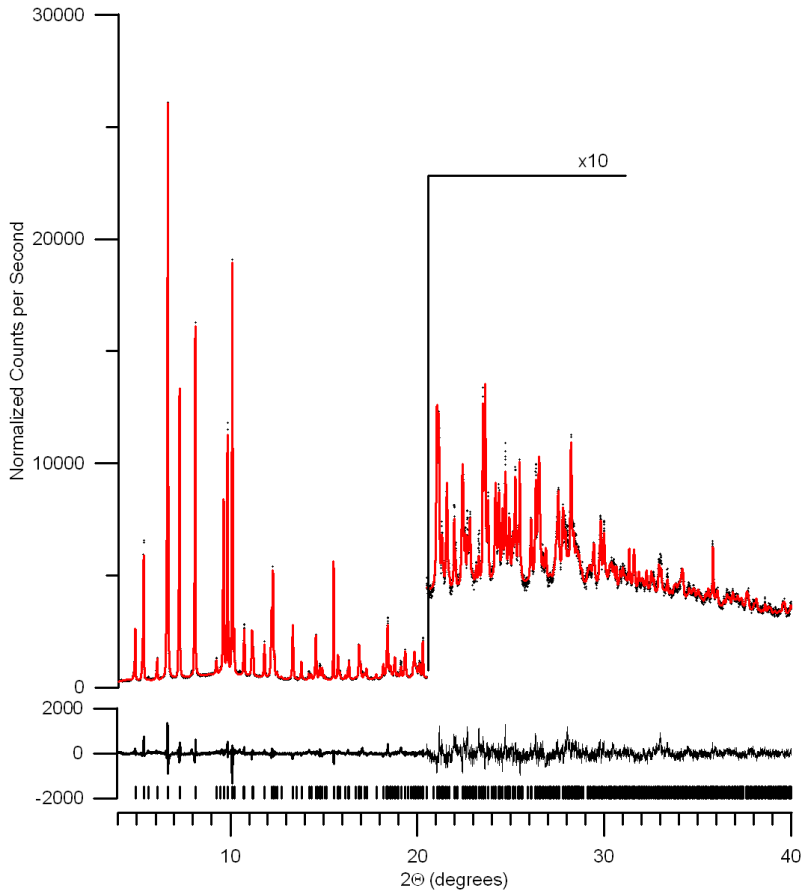

Figure 4.2. The pattern from the Rietveld refinement of **1**. The points are the data, the solid line is the calculated pattern from the refinement, and the difference between the two is shown on the same scale below the main plot.

This analysis revealed that, similar to **4**, the structure of **1** consists of buckled layers of $Mn^{II}(\mu_4\text{-}TCNE^{\bullet-})$, with a Mn-CN distance of 2.234(8) Å and an interlayer separation of 8.25 Å (Fig. 4.2). There are no covalent bonds between layers, as each Mn is axially terminated by two NCMe units, with a Mn-N distance of 2.206(6) Å. The octrahedral environment of the Mn is

slightly distorted with the 90° preferred N-Mn-N angles altered to values of 87.1(7)° and 89.4(8)°, with corresponding complement angles. The TCNE has a central C=C bond distance of 1.30(1) Å and a C-CN distance of 1.477(6) Å. The SbF_6 counter-ion occupies the voids between these layers. This new crystal structure is illustrated in Fig. 4.3. In order to model rotational disorder in SbF_6, the fluoride atoms were refined using anisotropic thermal parameters.

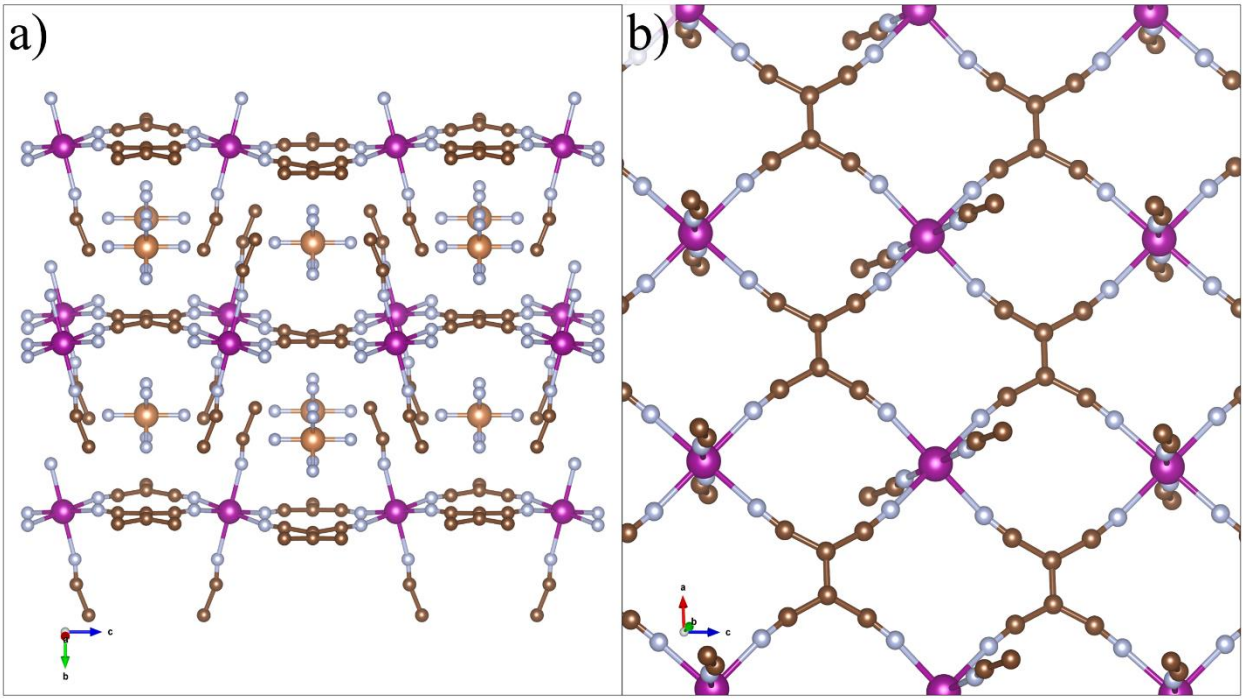

Figure 4.3. The resolved crystal structure of **1**. (a) Three layers, viewed perpendicular to the **c-b** plane. (b) A single $Mn^{II}(\mu_4\text{-}TCNE^{\bullet-})$ 2D plane viewed within the **a-c** plane.

When comparing representative XRD patterns for **1** and **2**, a resemblance is clearly observed, especially in the low-angle region Analysis of the XRD data confirmed that the compounds are isostructural, with refined lattice parameters for **2** of *a* =7.1366(7) Å, *b* =16.2715(13) Å and *c* =14.6495(14) Å (Fig. 4.3).

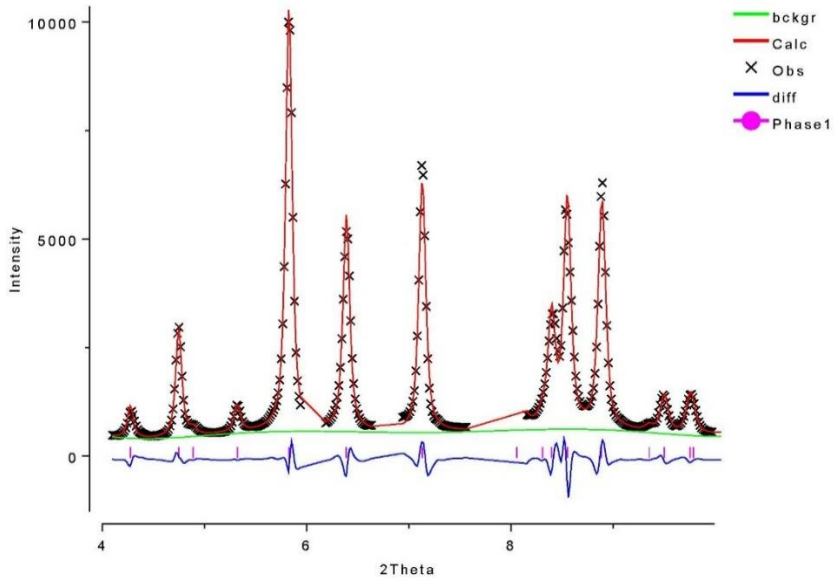

Figure 4.4. Le Bail fit to the PXRD pattern of **2** at 293 K (orthorhombic, *Cmcm*). Minor impurity reflections from unreacted starting material were omitted from the refinement and prevented reliable analysis beyond 10° 2θ.

4.3.2. Magnetic Transitions

The values of the magnetic susceptibility for M = Mn (**1**), Fe (**2**), Ni (**3**) at 300 K (represented as χT) of 4.89, 3.53 and 1.41 emu K/mol respectively, are in accord with the sum of contributions expected from high-spin octahedral M^{II} and $TCNE^{\bullet-}$ anion-radical (with weak spin-orbit coupling for M = Fe and Ni). The temperature dependencies of the in-phase, $\chi'(T)$, and out-of-phase, $\chi''(T)$, components of the complex AC susceptibility for **1**, **2,** and **3** exhibit peaks at T_{max} = 96, 67 and 20 K (in $\chi'(T)$), respectively (Fig. 4.5). The increase of $\chi''(T)$ below 70, 100, and 29 K for **1**, **2**, and **3**, respectively, is indicative of presence of remanent magnetization implying onsets of magnetic transitions. Magnetic behavior of **2** and **3** are very similar to that observed for **4** [15] and $[Ni(TCNE)(MeCN)_2]BF_4$ [9], while **1** demonstrates a much broader feature consisting of two components. The T_{max} temperatures in both $\chi'(T)$ and $\chi''(T)$ of all studied materials gradually increase with increasing frequency indicating the presence of time

dependent relaxation processes. Interestingly, the normalized frequency shift of T_{max} per frequency (ω) decade, $\phi = \Delta T_{max} / [\, T_{max}\, \Delta(\log\omega)]$, is 0.033 (calculated for more resolved low-temperature peak at 50 K), 0.007, 0.034, and 0.001 for **1**, **2**, **3**, and **4,** respectively. The compounds **1** and **3** have ϕ exceeding 0.01 that is characteristic of spin glass-like materials [19], while compounds **2** and **4** have values that are characteristic of non-disordered systems.

The complex shape of **1** and **3** $\chi(T)$ dependencies could be an indication of the presence of a substantial portion of an amorphous phase in the sample (solvent molecule variation or/and partial loss of N-coordinated MeCN) in addition to a polycrystalline phase that demonstrates well resolved XRD patterns. Thus, adjustment of the metal 3d orbital filling by varying the transition metal in isostructural magnets causes significant changes of their ordering temperatures T_c. Interestingly, the absolute value of metal ion spin does not seem to directly affect T_c, since it is almost 30% lower for **1** (S=5/2) than for **2** (S=2). It is conceivable to assume that in this case the details of the M[TCNE] nitrile group orbital overlap and related ligand-to-metal and metal-to-ligand charge transfers have a more profound effect on the superexchange and, consequently, the ordering temperature.

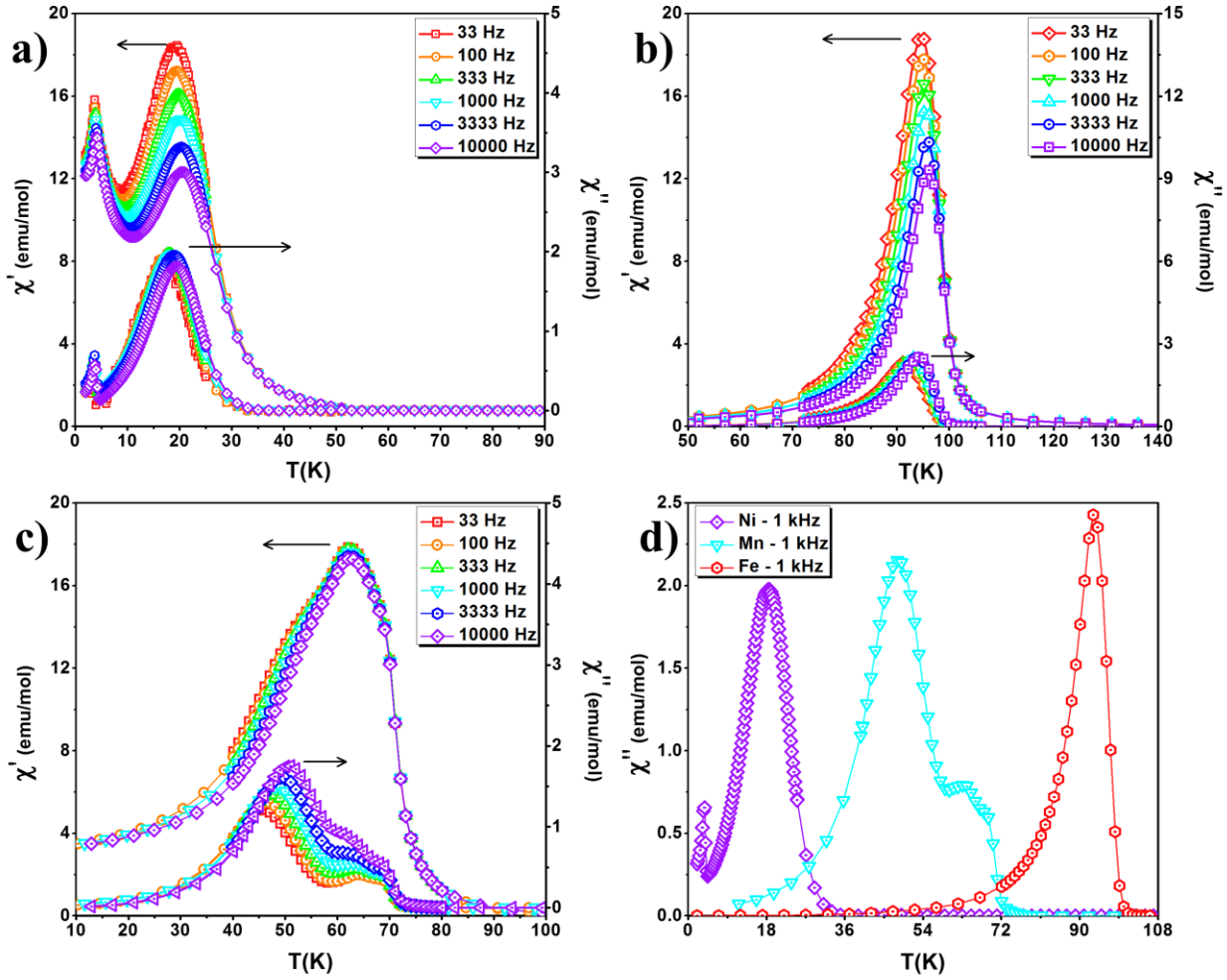

Figure 4.5. The in-phase $\chi'(T)$ and out-of-phase $\chi''(T)$ components of the complex AC susceptibility for **1** (Ni^{II}, a), **2** (Fe^{II}, b), **3** (Mn^{II}, c), and $\chi'(T, \omega = 1{,}000$ Hz) for **1-3** (d).

4.3.3. Spectroscopic Charge Transfer Evaluation

The TCNE reduction places electron density in the antibonding π^* LUMO localized over the central sp^2 carbon atoms (~1/2 e) and the terminal nitrogen atoms of the nitrile groups (~1/8 e on each) [160]. The population of the antibonding π^* orbital lowers the C≡N and C=C bonds orders causing a red shift of the corresponding stretching modes. Indeed, the peaks for $\nu_{C\equiv N}$ and $\nu_{C=C}$ of $TCNE^0$ appear at 2235 (a_g), 2262 (b_{3u}), 2228 (b_{1u}) [8] and 1569 cm^{-1} (a_g) [161], respectively, while the corresponding peaks for isolated $TCNE^{\bullet-}$ are red shifted to 2195, 2186,

2148, and 1420 cm^{-1}, respectively (Fig. 4.6) [162]. Interestingly, the Raman active totally symmetric $\nu_{C\equiv N}$ a_g mode is much less sensitive to the molecular charge, demonstrating an only 40 cm^{-1} red shift upon one electron reduction. It has been shown that in organic π^* radical systems the frequency of C≡N stretching modes is linearly related to the charge on the radical. Chappell *et al.* reported a linear plot of $\nu_{C\equiv N}$ of TCNQ salts vs. the degree of charge transfer [163].

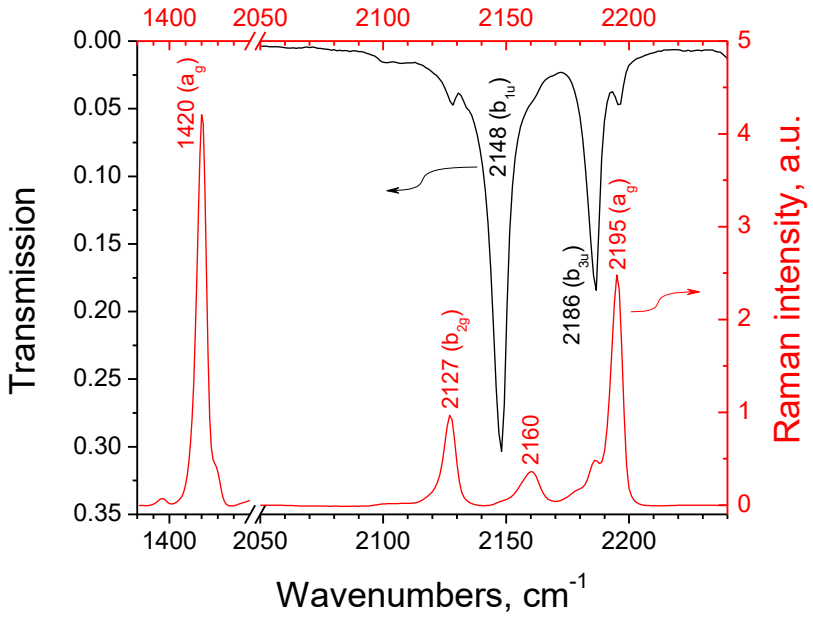

Figure 4.6. Characteristic vibrational modes of the $TCNE^{\bullet-}$ radical anion in the $Bu_4N[TCNE]$ molecular crystal from 1400 – 2400 cm^{-1}; infrared (black) and Raman (red).

Recently Stires *et al.* proposed a similar approach to determine the donor-acceptor charge transfer in TCNE complexes with methyl-substituted benzenes using the CH_2Cl_2 solution spectra of $TCNE^0$ and electrochemically synthesized $TCNE^{\bullet-}$ and $TCNE^{2-}$ [164]. Plotting $\nu_{C\equiv N}$ frequency vs. the formal TCNE charge, Z, the linear expressions can be readily obtained.

$$Z = [2256.8-\nu_{C\equiv N}\ (b_{3u})]/65.5\ [e] \qquad \text{(eq. 4.1)}$$

$$Z = [2218.5-\nu_{C\equiv N}\ (b_{1u})]/72.5\ [e] \qquad \text{(eq. 4.2)}$$

Using $\nu_{C=C}$ (a_g) frequencies [8] a similar correlation can be proposed ($R^2 = 0.999$):

$$Z = [1571-\nu_{C=C} (a_g)]/154.5 \text{ [e]} \quad \text{(eq. 4.3)}$$

It should be noted that $\nu_{C=C}$ (a_g) frequency is much more sensitive to the charge on TCNE with respect to that of $\nu_{C\equiv N}$ modes in accord with the π^* electron density distribution. Thus, the electron density on the π^* orbital (monitored via the shift of $\nu_{C=C}$ mode) could work as a very valuable indicator of the charge redistribution due to $TCNE^{\bullet-}$ coordination in the M[TCNE] magnets and can be directly related to the magnetic exchange.

The Raman spectra of all studied compounds **1**-**4** are shown in Fig. 4.7a. They are very similar and resemble the spectrum of $TCNE^{\bullet-}$ anion in Bu_4N[TCNE] with totally symmetric $\nu_{C=C}$ and $\nu_{C\equiv N}$ modes which dominate in intensity at 1440-1450 cm^{-1} and 2230-2250 cm^{-1} regions, respectively. The spectrum of **1** is much better resolved, most probably due to the higher portion of crystalline material in the product. The totally symmetric ν_{C-CN} at 515 cm^{-1} and two deformation modes at 478 and 150 cm^{-1} as well as two b_{2g} modes at 1295 and 2170 cm^{-1} can be readily identified.

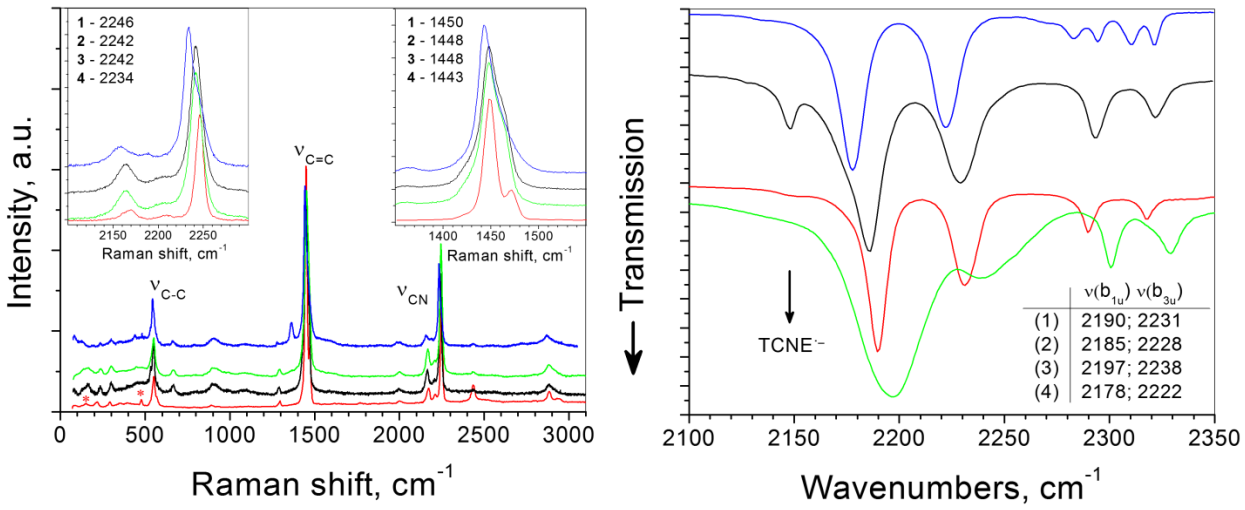

Figure 4.7. Raman (left) and infrared (right) spectra in the $\nu_{C\equiv N}$ region of the compounds **1** (red), **2** (black), **3** (green) and **4** (blue). The detailed Raman spectra in the region of stretching $\nu_{C\equiv N}$ and $\nu_{C=C}$ modes are shown in the left and right insets, respectively.

The blue shift of the a_g $\nu_{C=C}$ mode with respect to its position in the Raman spectrum of $TCNE^{\bullet-}$ anion (as well as all other a_g modes) suggests π^* orbital depopulation due to a substantial ligand-to-metal charge transfer (LMCT). Similar blue shift of the $\nu_{C\equiv N}$ modes is observed in the IR spectra of all studied magnets (Fig. 4.7b). Using the equations (1-3), the formal charge on $TCNE^{\bullet-}$ ligand, Z, was evaluated (Table 4.2). The shift values of the $\nu_{C=C}$ modes are practically the same for all compounds, implying that about 20% of charge from the π^* orbital of $TCNE^{\bullet-}$ is engaged in bonding with 3d orbitals of the metal ions. This is in accord with the conclusion of de Jong *et al.* regarding the hybrid ground state in $V[TCNE]_2$ [7]. In contrast, the shifts of both $\nu_{C\equiv N}$ (b_{3u}) and $\nu_{C\equiv N}$ (b_{1u}) modes differ for different metals with a formal Z value ranging from 0.29 for **3** to 0.56 for **4**. As mentioned above, 3d metal-to-TCNE bonding is predominantly a *σ*-type electron donation from the nitrogen-localized lone-pair electrons (:N≡C-) of the nitrile group on TCNE into empty (or partially empty) 4*p* and 3d orbitals of M^{II} ion.

Table 4.2. The frequencies of $\nu_{C=C}$ (a_g), $\nu_{C\equiv N}$ (b_{3u}), and $\nu_{C\equiv N}$ (b_{1u}) modes for compounds **1-4**, and ligand-to-metal charge transfer evaluation using equations 1-3.

	ν_{CC} (a_g) cm^{-1}	$Z(a_g)$[a] |e|	ν_{CN} (b_{3u}) cm^{-1}	$Z(b_{3u})$[b] |e|	ν_{CN} (b_{1u}) cm^{-1}	T_c K	$Z(b_{1u})$[c] |e|	$\Delta\nu(\sigma)$ cm^{-1}	$\|Z\|(\nu_{CN})$[d] |e|
Mn (**1**)	1450	0.78	2231	0.39	2190	67	0.39	22	0.71
Fe (**2**)	1448	0.80	2228	0.44	2185	96	0.46	25	0.81
Ni (**3**)	1448	0.80	2238	0.29	2197	20	0.30	32	0.75
$FeCl_4$ (**4**)	1443	0.83	2222	0.53	2178	89	0.56	25	0.91

[a] calculated using equation (3);
[b] calculated using equation (1);
[c] calculated using equation (2);
[d] average of $Z(b_{3u})$ and $Z(b_{1u})$ after subtraction of $\Delta\nu(\sigma)$ (see text).

Since the lone pair wave function is weakly anti-bonding with respect to N≡C bond, this σ-type coordination causes a blue shift of $\nu_{C\equiv N}$ stretching modes compared to those in isolated $TCNE^{\bullet-}$ [165]. It should be noted that the electron-rich Ni is more electronegative than less electron-rich Fe and Mn; therefore, in **3** the metal-ligand bond strength and the corresponding frequency of the $\nu_{C\equiv N}$ mode are expected to be higher than in **1** or **2** [166]. Since the TCNE $\nu_{C\equiv N}$ mode's frequency shift due to σ-type coordination was not reported in the literature [8], for evaluation purposes the $\nu_{C\equiv N}$ mode shift $\Delta\nu(\sigma)$) (Table 4.2) for σ-coordinated MeCN in **1-4** with respect to its position in a free MeCN solvent molecule [167] is used. Subtracting these values from the frequencies of both $\nu_{C\equiv N}$ (b_{3u}) and $\nu_{C\equiv N}$ (b_{1u}) modes and applying again the formula (1) and (2), the new values of the formal TCNE charge after averaging are shown as $|Z|(\nu_{C\equiv N})$ in Table 4.2. There is a reasonable agreement between $Z(a_g)$ and $|Z|(\nu_{C\equiv N})$, suggesting that both $\nu_{C=C}$ and $\nu_{C\equiv N}$ modes are good for the degree of LMCT evaluation. However, the standard deviation in Z value derived from the $\nu_{C\equiv N}$ modes position (10%) is four times larger than that

for $\nu_{C=C}$ modes, presumably due to uncertainty in σ-coordination contribution, structural defects related line broadening (MeCN loss), etc.

It is interesting to note that the stronger metal-TCNE bond does not necessarily translate into higher T_c. In **3**, the metal-TCNE bond is the strongest among all studied compounds, while its T_c is only 20 K. In octahedral Ni^{II}, two unpaired spins occupy anti-bonding e_g orbitals which most probably are orthogonal to the partially occupied π* orbital of $TCNE^{\bullet-}$ resulting in ferromagnetic (FM) coupling between these spins. Indeed, for the $[Ni(TCNE)(NCMe)_2]BF_4$ magnet, a very close analog of **3**, it was shown that the saturated magnetization is 72% higher than anticipated assuming AFM interaction [9]. However, Raman study has shown that there is a substantial LMCT, and, presumably, some t_{2g}/π^* orbital mixing. Most probably, in both these compounds there is a competition of AMF and FM couplings resulting in lower T_c and non-collinearity of Ni^{II} and $TCNE^{\bullet-}$ magnetic sublattices [9]. Obviously, in $V[TCNE]_x$ this competition does not exist, which could be one of the reasons of the above room temperature T_c observed in this material.

The backbonding should suppress FM coupling, moving π* spin density away from the metal. The less pronounced LMCT effect for **2** with respect to **1** and especially for **4** could be an indication of some backbonding that correlates with higher T_c. Moreover, the preliminary Raman results for a new magnet $[Mn^{II}(TCNE)_{1.5}](I_3)_{0.5}$ **(5)** [85] have shown that the $\nu_{C=C}$ peak is shifted down to 1430 cm^{-1}, corresponding to less than 0.09 |e| LMCT. The shape of the magnetic transition in this material is very similar to that in $[M(TCNE)(NCMe)_2]SbF_6$ magnets. However, the T_c of this new magnet **5** is 170 K, which is more than 2.5 times higher than in **1**, suggesting a much higher backbonding effect in accord with the assumption above. It should be noted that the crystal structure of **5** is fully 3D with each Mn coordinated to six TCNE ligands, which by itself

may be a reason for the higher T_c; this is explored extensively in Chapter 6. In general, there are structural factors (e.g., anion size, weak interplane interaction, solvent loss, etc.) that could influence T_c but have little effect on the degree of LMCT. Thus, monitoring Z by Raman spectroscopy may provide very useful information, allowing understanding of the peculiarity of the super-exchange interaction in M[TCNE] magnets and establishing the structure-magnetic property correlations in this class of magnetic material.

4.4. Conclusions

The Raman frequency of the totally symmetric $\nu_{C=C}$ vibrational mode of the $TCNE^{\bullet-}$ radical is solely dependent on the π* electron density localized on the two central carbon atoms, and should be very sensitive to a metal-ligand π* electron density transfer in both directions. The MBMs $[M^{II}(TCNE)(MeCN)_2]SbF_6$ (M = Mn, Fe, Ni) were synthesized and an air-free experimental technique was developed allowing for collection of Raman and IR spectra of these materials. The frequencies of the Raman $\nu_{C=C}$ mode for all compounds are substantially higher (> 20 cm^{-1}) than those for isolated $TCNE^{\bullet-}$. This is indicative of a significant ligand-to-metal π* electron density transfer, and may suggest that previous MCD experiments [18] concluding a V^{II} 3d ground state consisting of 60% $3d^3$ and 40% $3d^4\underline{L}$ ($\underline{L}$ = hole on $TCNE^{\bullet-}$ ligand) states is correct. For all $[M^{II}(TCNE)(MeCN)_2]SbF_6$ materials, spectroscopic estimations give approximately 20% of a $3d^4\underline{L}$ component assuming that the Raman shift is linear with π* electron density. A wide range of T_c was observed upon substitution of the transition metal identity (Mn - 70 K; Fe - 90 K; Ni - 29 K), but these changes do not correlate with a spectroscopic shift in π* density, suggesting magnetocrystalline anisotropy may play a

dominating factor in the magnetic transition characteristics in this material series. Finally, the crystal structure of the new $[Mn^{II}(TCNE)(MeCN)_2]SbF_6$ molecule-based magnet was reported.

5. MAGNETIC TRANSITIONS TWO-DIMENSIONAL MN[TCNE] MATERIALS

5.1. Introduction

The two dimensional $[Mn^{II}(TCNE)(MeCN)_2]SbF_6$ represents an interesting model system to explore magnetic transitions in a two dimensional lattice lacking strong magnetocrystalline anisotropy due to the L=0 state of the high spin, S=5/2 Mn^{II} metal. Theory predicts that for systems with strictly 2D magnetic interaction, T_c becomes finite only if the magneto-crystalline or dipolar type anisotropy is introduced [168]. For instance, the stable homogeneously magnetized state is observed in $[Fe(TCNE)(NCMe)_2]FeCl_4$ [83,157] due to a strong Fe^{II} ion anisotropy enabling the magnetic ordering at T_c = 90 K within the $Fe^{II}(\mu_4\text{-}TCNE^{\bullet-})$ ferrimagnetic Ising plane with an easy axis perpendicular to the plane. Conversely, the dipolar interaction between ferromagnetic layers was proposed to explain the stabilization of a 3D magnetic ordering at T_c = 20 K in the layered hybrid compounds $Cu_2(OH)_3(n\text{-}C_mH_{2m+1}CO_2)\bullet zH_2O$, which contain a significantly less anisotropic Cu^{II} ion [169]. To elucidate the role of interlayer dipole magnetic coupling, the synthesis and characterization of $[Mn(TCNE)(NCMe)_2]X$ complexes (X = PF_6, AsF_6, SbF_6) was carried out. In these compounds, isotropic Mn^{II} ions strongly couple magnetically with ligands forming $Mn^{II}(\mu_4\text{-}TCNE^{\bullet-})$ layers, thus allowing the interlayer distance to be controlled by the size of the diamagnetic anions. If dipole–dipole magnetic coupling ($\propto 1/r^3_{i,j}$, where $r_{i,j}$ is a distance between two dipoles) between Mn^{II} ions mainly facilitates a long-range magnetic ordering between adjacent layers, substantial changes of magnetic properties might be expected upon modulation of interlayer spacing. Finally, it was shown that a re-entrant spin-glass transition is characteristic of all members of this series. This behavior was studied and interpreted in terms of the dynamic spin-relaxation and slow isothermal decay of the magnetized state at low temperature. The implications of interlayer-spacing modulation on the static and

dynamic magnetic behavior of the newly synthesized $[Mn(TCNE)(NCMe)_2]X$ complexes (X = PF_6, AsF_6, SbF_6) are reported herein.

5.2. Experimental Details

All $[Mn(TCNE)(NCMe)_2]X$ (X = PF_6, AsF_6, SbF_6) complexes were synthesized via reaction of $[Mn(NCMe)_6]X_2$ with $Bu_4N[TCNE]$ in CH_2Cl_2 according to the procedures described elsewhere [82,97]. Elemental analysis results were consistent with the expected products. All studies were performed on polycrystalline powder samples that were loaded, transferred, and measured in a dry glove box under inert conditions (<1 ppm H_2O and O_2).

Thermo-magnetic studies were completed with a Quantum Design (QD) Physical Properties Measurement System (PPMS) using the ACMS options for measurements of the magnetization and AC susceptibility as a function of applied field and temperature, as previously described [158]. Infrared spectra (400 to 4000 cm^{-1}) were obtained on a Bruker Vertex FT-IR spectrometer as KBr pellets or Nujol mulls. Unpolarized Raman spectra were obtained in 75-3100 cm^{-1} spectral range with ~1 cm^{-1} resolution using a LabRAM Aramis Horiba Jobin Yvon Confocal Raman Microscope equipped with a CCD utilizing 532 and 785 nm coherent excitation sources. A linear baseline was fitted directly to the corrected Raman spectra. To avoid air exposure, powder samples were placed between two glass slides glued inside the N_2 glove box. No changes due to oxidation were observed in the Raman spectra within ~30 min. To prevent decomposition due to overheating, the laser power was kept below 2 mW (×10 objective, ~20 μm diameter laser spot diameter).

High resolution synchrotron X-ray powder diffraction patterns of $[Mn(TCNE)(NCMe)_2]PF_6$ and $[Mn(TCNE)(NCMe)_2]AsF_6$ were collected at the X16C beamline at the National Synchrotron Light Source at Brookhaven National Laboratory. X-rays of

wavelength 0.6999 Å were selected using a Si (111) channel cut monochromator. The diffracted beam was analyzed with a Ge (111) crystal and detected by a NaI scintillation counter. Wavelength and diffractometer zero were calibrated using a sample of NIST Standard Reference Material 1976, a sintered plate of Al_2O_3.

TOPAS-Academic [130,170,171] was used to index and refine the crystal structure. The structure of $[Mn(TCNE)(NCMe)_2]SbF_6$ [82] was used as an initial model for the Rietveld refinement with the appropriate replacement of the anion. The refinements required strongly anisotropic thermal parameters for the F atoms, implying substantial rotational disorder of the anions.

5.3. Results and Discussion

5.3.1. Crystal and Vibrational Structure

From the high resolution powder X-ray patterns, it was found that $[Mn(TCNE)(NCMe)_2]PF_6$ (**6**) and $[Mn(TCNE)(NCMe)_2]AsF_6$ (**7**) are isostructural to the previously reported $[Mn(TCNE)(NCMe)_2]SbF_6$ (**1**) magnet [82]. Their crystal structures consist of orthorhombic unit cells containing corrugated layers of octahedral Mn^{II} cations bound to equatorial μ_4-$TCNE^{\bullet-}$ anion-radicals and axial MeCN ligands (Fig. 5.1).

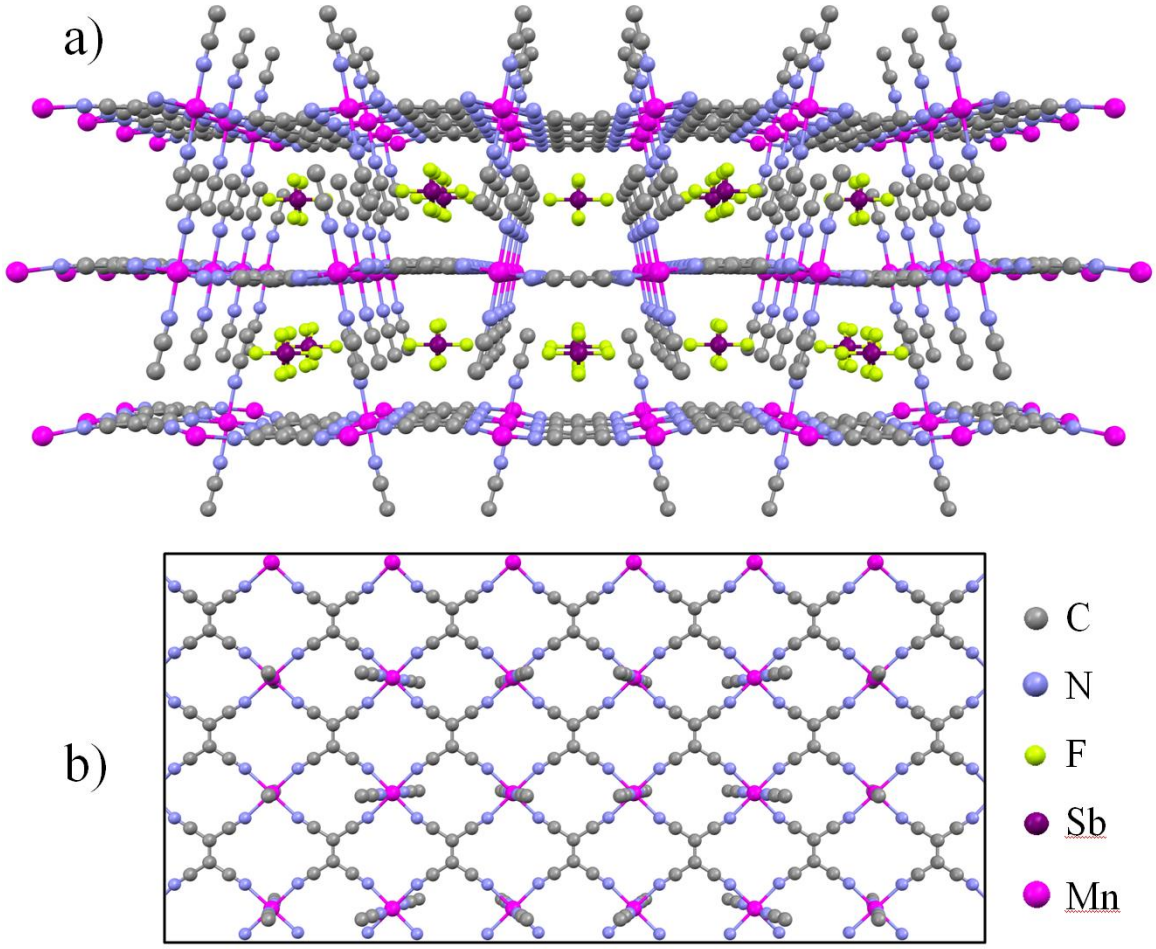

Figure 5.1. X-ray structure of $[Mn(TCNE)(NCMe)_2]SbF_6$ projected along the cell axis ***a*** (a – multiple layers, facing ***b*-*c*** plane) and ***b*** (b – single layer, facing ***a*-*c*** plane), illustrating the corrugated two-dimensional layer structure. Hydrogen atoms are not shown for clarity.

The non-coordinating counter anion is located between the Mn[TCNE] sheets, with the space between these Mn[TCNE] layers increasing from 7.94 Å to 8.16 Å due to an increase of the anion size from PF_6^- to SbF_6^-. Additionally, the canting angle between the equatorial planes of adjacent Mn atoms increases with the size of the counter anion. Values for these and others important structural parameters are listed in Table 5.1.

Table 5.1. Selected structural and spectroscopic parameters for $[Mn(TCNE)(NCMe)_2]X$.

Compound	***6***	***7***	***1***
Space group	*Ccmm*	*Ccmm*	*Cmcm*
Lattice constant *a* (Å)	15.877	16.036	7.192
Lattice constant *b* (Å)	7.142	7.159	16.294
Lattice constant *c* (Å)	14.994	14.972	14.943
Mn-Mn intra-plane along *a* (Å)	7.142	7.159	7.192
Mn-Mn intra-plane along *c* (Å)	7.497	7.486	7.471
Mn-Mn inter-plane along *b* (Å)	8.705	8.780	8.905
Interlayer spacing along *b* (Å)	7.94	8.02	8.15
MnN_4-TCNE dihedral angle (°)	9.16	9.81	11.47
$\nu_{C\equiv N}$ b_{1u} (cm^{-1})	2193	2192	2190
$\nu_{C\equiv N}$ b_{3u} (cm^{-1})	2235	2234	2231
$\nu_{C\equiv N}$ a_g (cm^{-1})	2247	2248	2246
$\nu_{C=C}$ a_g (cm^{-1})	1447	1448	1449

The FTIR and Raman measurements have revealed two IR active (b_{1u} and b_{3u}) as well as two totally symmetrical (a_g) Raman active $\nu_{C\equiv N}$ and $\nu_{C=C}$ stretching modes of μ_4-$TCNE^{\bullet-}$, respectively (Table 5.1). No significant frequency shifts were expected due to the isostructural character of the studied magnets; however, a tendency toward a slight (< 5 cm^{-1}) softening of $\nu_{C\equiv N}$ IR active modes with the increase of canting angle is observed, which suggests a small change in Mn-N≡C orbital overlap. In contrast, the $\nu_{C=C}$ stretching mode frequencies of **6-7**, **1** have shown only small shifts within the experimental error. The frequency of the a_g C=C stretching mode in the isolated $TCNE^{\bullet-}$ anion is ~1420 cm^{-1}, suggesting that 22 ± ~1 % of the $TCNE^{\bullet-}$ π* orbital is transferred to Mn in **6** and **7** in accord with the charge transfer reported

previously for **1** [82]. The observed insensitivity of the C=C Raman response to anion size modulation indicates no variation in the degree of charge transfer in the series [82].

5.3.2. Magnetic Characteristics

Magnetic susceptibility in the 5-300 K range for **1** was plotted as $\chi T(T)$ and $\chi^{-1}(T)$ [$\propto (T - \theta)$] (Fig. 5.2). At 300 K, χT equals 4.92 emu·K/mol, exceeding the expected sum of the spin-only values for octahedral Mn^{II} and $TCNE^{\bullet-}$ (4.75 emu·K/mol), thus suggesting that metal-ligand magnetic coupling persists above the room temperature. In accord with strong coupling, a linear fit of $\chi^{-1}(T)$ in the range between 125 and 250 K revealed a Weiss constant θ of ~110 K, suggesting the presence of magnetic transition below this temperature.

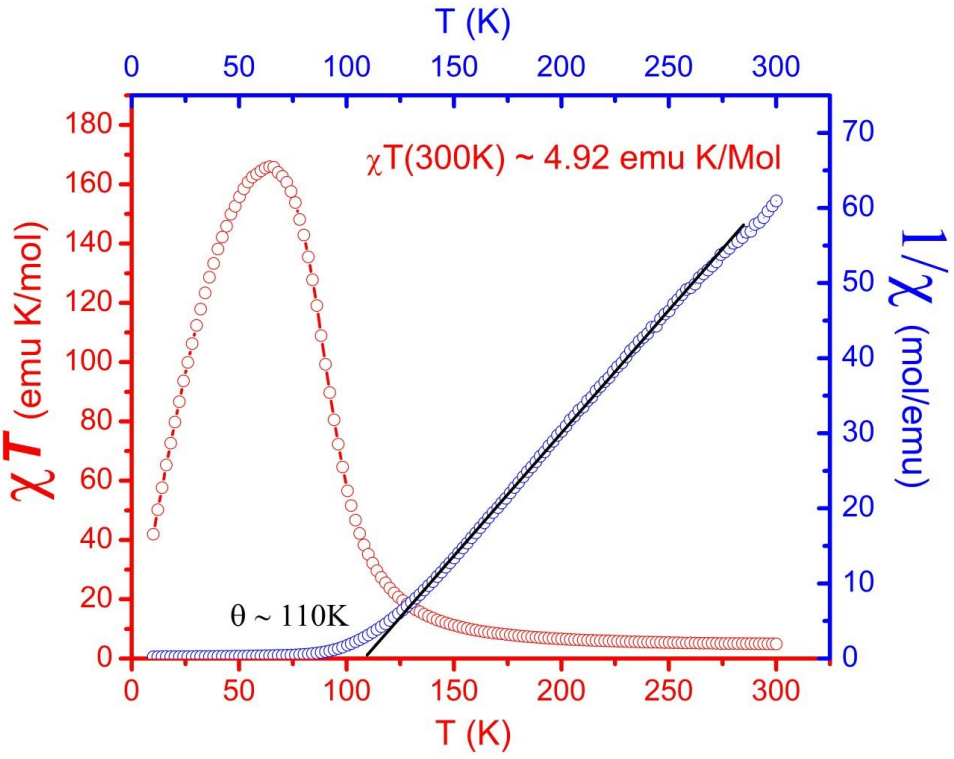

Figure 5.2. $\chi T(T)$ and $\chi^{-1}(T)$ of **1** (at H=5 kOe).

The field-dependent magnetization, $M(H)$, of **1** at 5 K is characteristic of a magnetically ordered state (Fig. 5.3). It is nearly saturated at 60 kOe reaching 22944 emu·Oe/mol (4.1 μ_B), which is slightly above the 4.0 μ_B expected for antiferromagnetically (AFM) coupled Mn^{II} (S = 5/2) and $TCNE^{\bullet-}$ (S = 1/2) ions. Evidently, the corresponding low-temperature *g*-factor for the Mn^{II} ion is slightly higher than 2 (g = 2.04), in accord with the ESR results for a similar Mn-TCNE magnet [172]. The $M(H)$ of **3** also exhibits a hysteresis with a coercive field, H_{cr}, of ~50 Oe and remanent magnetization, M_r, of 3100 emu·Oe/mol (0.56 μ_B) (Fig 5.3 inset). The magnets **6** and **7** demonstrate similar behavior.

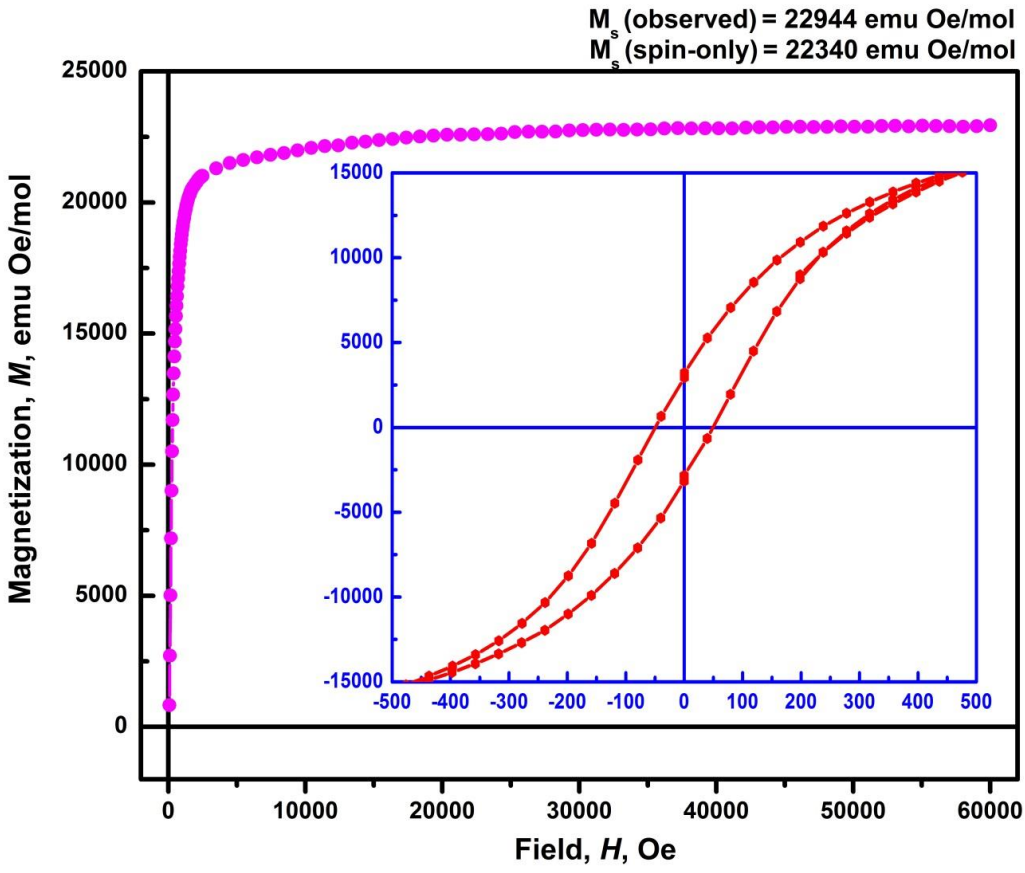

Figure 5.3. $M(H)$ and a hysteresis loop of **1** at 5 K (inset).

The 50 Oe field cooled and zero-field cooled magnetizations, $M(T)_{FC}$ and $M(T)_{ZFC}$, respectively, rise sharply below 80 K for all studied magnets (Fig. 5.4), which is indicative of the

onset of magnetic transition. $M(T)_{ZFC}$ curves reach maxima at T_{max} of 61, 63 and 62 K for compounds **6**, **7**, and **1**, respectively, followed by a gradual $M(T)_{ZFC}$ decrease which is presumably due to spin freezing. However, the unusual curvature of $M(T)_{ZFC}$ below T_{max} may be indicative of a second transition (vide infra). The $M(T)_{FC}$ magnetizations also decrease below $T_{max,}$ but at a much slower pace, reaching a shallow minima around 45 K, and then start growing again reaching values close to those at T_{max} at 5 K. The $M(T)_{ZFC}$ and $M(T)_{FC}$ bifurcation temperature $T_b = T_{max}$ is indicative of spin-glasses (SG) [173]. When the samples **6-7**, **1** were cooled to 5 K in a 100 Oe field followed by $M_r(T)$ measurement at zero field, the non-zero $M_r(T)$ values persisted up to ~75 K (Fig. 5.4). From $M_r(T)$ onsets the magnetic transitions have been evaluated to occur at T_c of 72, 73 and 75 ± 1 K for **6**, **7** and **1**, respectively. In going from **6** to **7** to **1**, the interlayer spacing and the shortest Mn-Mn inter-plane distance increase by 2.8% and 2.3%, respectively. Since $T_c \propto H_{dip} \propto 1/r^3_{i,j}$ (where H_{dip} is an average dipolar field) [169,174], T_c is expected to decrease by an amount between 7.1% and 8.5%. Opposite of this expectation, the transition temperature T_c increases slightly as the interlayer Mn-Mn inter-plane distance increases. Substitution of the large SbF_6 anion with the smaller PF_6 one thereby causing a contraction of the crystal lattice is a well-known approach to mimic the effect of external pressure [175]. Recently it was shown that the unit cell volume of **1** varies continuously with pressure up to 2 GPa with a bulk modulus $K = -V(dP/dV) = 10.4$ GPa.

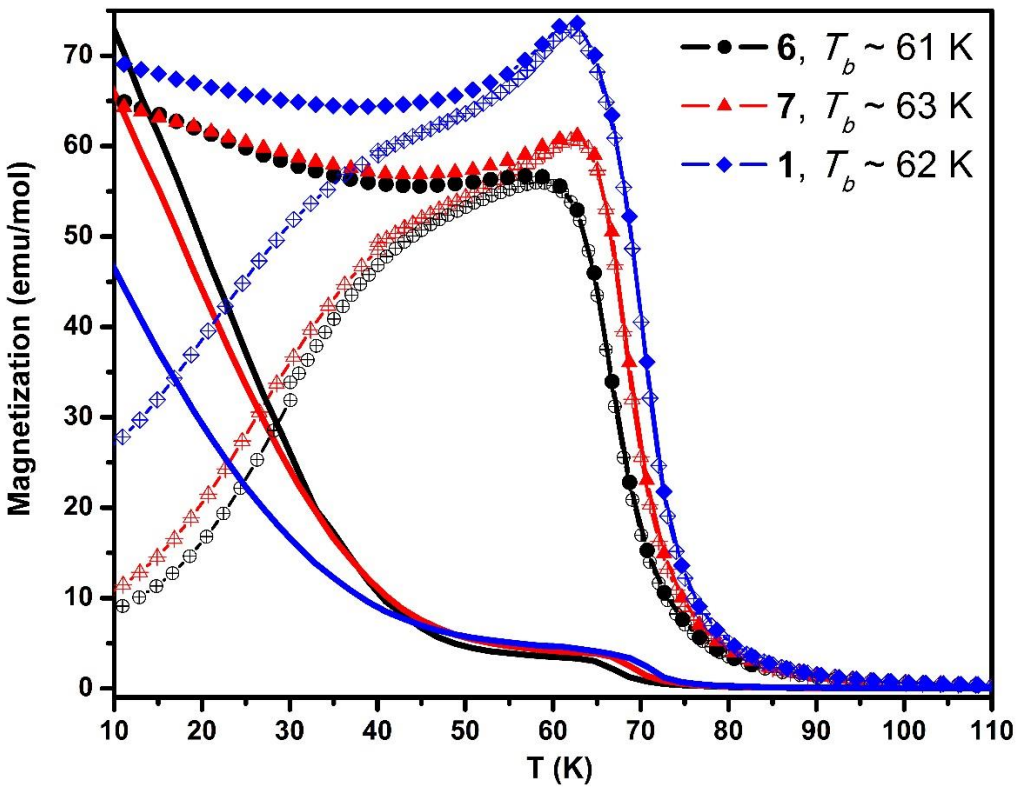

Figure 5.4. $M(T)_{ZFC}$ (open symbols with guide-line), $M(T)_{FC}$ (closed symbols), and $M_r(T)$ curves (solid lines) for [Mn(TCNE)(NCMe)$_2$]X series.

The main change in the unit cell volume occurs due to inter-layer distance contraction, while $Mn^{II}(\mu_4\text{-}TCNE^{\bullet-})$ layers remain relatively rigid reflecting the two-dimensional character of the network [176]. The observed differences in the intra- and interlayer structural parameters of **6** and **1** (3% volume and 2.3% interlayer distance decrease, respectively) due to the anion size change are consistent with the "chemical pressure" effect corresponding to ~0.5-0.6 GPa hydrostatic pressure application [176]. However, the magnetic studies of **1** under pressure have shown a sizable (up to 5%) increase of T_c at 0.6 GPa. Conversely, T_c for **6** is about 3 K lower than that for **1** despite a substantial inter-layer distance contraction and expected dipole coupling enhancement. It is conceivable that despite a shorter inter-layer spacing and larger dipole coupling in **6,** the T_c decrease is predominantly defined by the intra-layer direct and/or super-

exchange, e.g. the increase of the MnN_4-TCNE dihedral angle, which may facilitate a slightly better orbital overlap between Mn and NC moieties.

In all studied compounds $M_r(T)$ decreases rapidly from 5 to ~45 K, then decreases at a much slower pace with further warming, until it drops more rapidly again below 65 K, thus suggesting a possibility of multiple transitions in the $45 < T < 65$ K temperature range. To elucidate the nature of these transitions, the in-phase, $\chi'(T)$, and out-of-phase, $\chi''(T)$, components of the complex AC susceptibility of compounds **6-7**, **1** were measured at 3 Oe AC field and frequencies ranging from 33 Hz to 10 kHz in the temperature range of $20 < T < 80$ K. The corresponding χ vs. T curves are shown in Fig 5.5 (a-c). While $\chi'(T)$ curves (Fig. 5.5, left column) are similar in shape to $M(T)_{ZFC}$ plots, the splitting of χ''(T) curves (Fig. 5.5, right column) at least into two components clearly indicates the presence of multiple magnetic transitions in all of the studied materials. The onset of spontaneous magnetization or rapid increase in $\chi''(T)$ is often associated with T_c of magnetic transition [43]. For all studied compounds the abrupt raise of $\chi''(T)$ below ~69, 71, and 74 ± 1 K for **6**, **7**, and **1**, respectively, is in accord (within the experimental error) with the T_c values evaluated from $M_r(T)$.

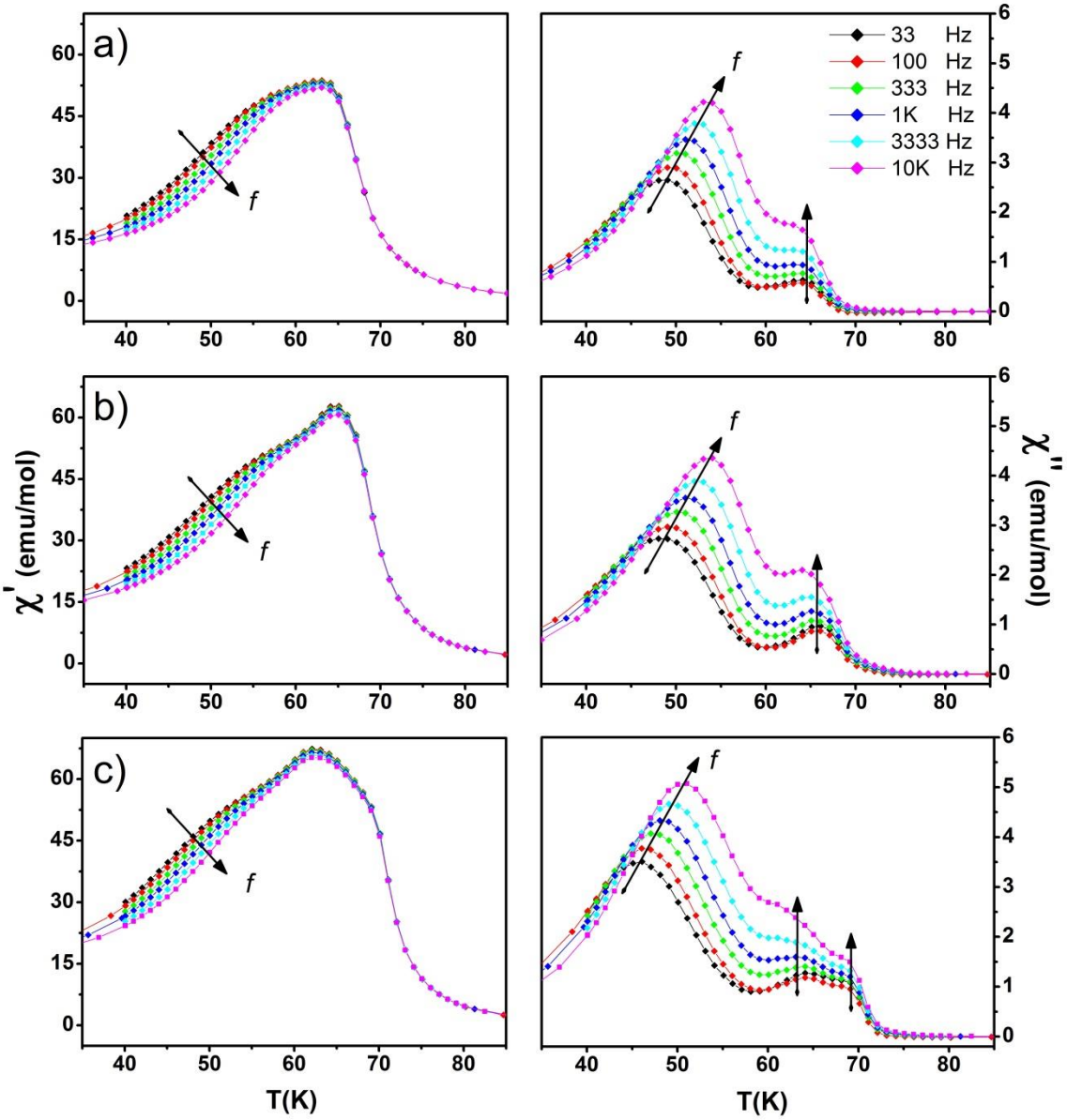

Figure 5.5. In-phase (χ') and out-of-phase (χ'') magnetic susceptibilities for $[Mn(TCNE)(NCMe)_2]X$, (X = PF_6^- [**6**, a], AsF_6^- [**7**, b], and SbF_6^- [**1**, c]) series.

5.3.3. Spin Glass Ordering

The analysis of the $\chi'(T)$ and $\chi''(T)$ susceptibilities at different frequencies may provide additional information about the nature of magnetic transitions observed in **6-7**, **1**. For spin-glasses, a frequency dependent maximum in $\chi'(T)$ (as well as the maximal slope in $\chi''(T)$) is

typically associated with the spin-freezing temperature T_f [22a]. In all studied compounds the T_{max} of the broad $\chi'(T)$ curves (at 63, 65 and 63 K for **6**, **7**, and **1**, respectively) is practically frequency independent, as is T_{max} of the more narrow peak/shoulder in the corresponding $\chi''(T)$ curves at 65, 66 and 64/69 K. For **1** the shift is difficult to evaluate due to a splitting of high temperature peak into two components at 64 and 69 K. The nature of this splitting is unknown; nevertheless, deconvolution of all peaks reveals only weak, if any (ΔT_{max} < 0.5 K) frequency dependence of both components (Fig. 5.6).

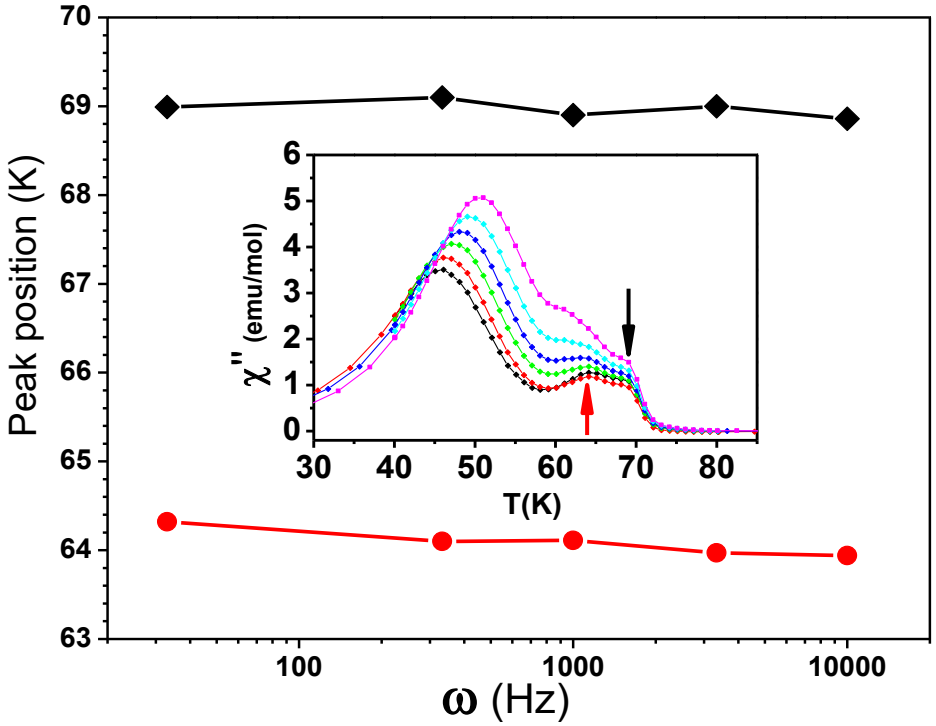

Figure 5.6. Frequency dependence of the high-temperature transition maxima from $\chi''(T)$ in complex **1** at ~69 K (black) and ~64 K (red). Inset shows the out-of-phase, $\chi''(T)$ component of the complex AC susceptibility for multiple frequencies (see Fig. 5.5 for legend). Peak positions are highlighted by color-coded indicators.

Such behavior of the AC susceptibility is in contrast with that expected for canonical spin-glasses. Therefore, these high-temperature features in $\chi'(T)$ and the associated peaks in $\chi''(T)$ are interpreted as manifestations of the long-range ferrimagnetic ordering in the studied compounds.

Conversely, the hump-like features in the in-phase $\chi'(T)$ curves and $\chi''(T)$ peaks at T_{max} of 46, 48 and 50 K for **6**, **7**, and **1**, respectively, exhibit the strong frequency dependence. Thus, it is conceivable to assert that the spin freezing occurs below these temperatures, manifesting a spin-glass state. All $d\chi'(T)/dT$ curves (Fig. 5.7) clearly show a peak corresponding to T_{max} in $\chi''(T)$, which shifts to higher temperatures with frequency, though experimental uncertainty introduced by differentiation of the curve thwarts a precise quantization of the peak shift.

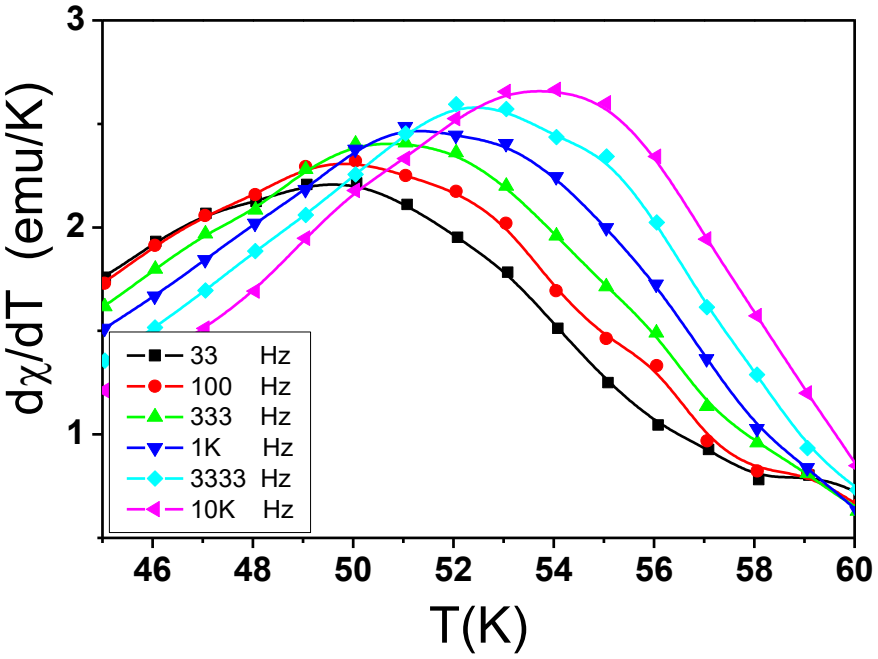

Figure 5.7. Temperature dependent $d\chi'(T)/dT$ curves for complex **1** measured with various AC field frequencies.

To accurately quantify the spin disorder parameter, the shift of the peak in the highly sensitive $\chi''(T)$ measurement is considered. A useful criterion for distinguishing a canonical spin glass from a spin-glass-like material is $\delta T_f = \Delta T_f/(T_f \Delta \log(\omega))$, which gives the relative shift of the spin-glass transition temperature T_f (usually defined as the peak temperature in χ'(T) curve) per frequency decade [22a]. In the present work, although the actual spin glass freezing temperature T_f cannot be determined from the χ'(T) curve, it is possible to calculate the

frequency shift of T_{max} using a similar expression to seek the spin glass features in the molecule-based magnets studied. The normalized frequency shift φ of the $\chi''(T)$ peak at T_{max} per frequency (ω) decade was evaluated using eq. 5.1

$$\varphi = \frac{\Delta T_{max}}{T_{max}\Delta(\log_{10}\omega)} \quad \text{(eq. 5.1)}$$

For both **6** and **7,** the T_{max} shift is 0.034, and 0.047 for **1**, comparable to the values of δT_f reported for cononical spin glasses [22a].

One of the remarkable characteristics of the SG state is a long-time decay of the remanent magnetization [22b]. The AC susceptibility measurements revealed a time-dependent magnetic relaxation in **6-7**, **1** that suggests a manifold of response times due to a configurational spin-disorder below T_c. When cooled in magnetic field, all spins become aligned resulting in disorder suppression; however, the relaxation of the system back to thermodynamic equilibrium in zero field may reveal additional details about the nature of the frozen state. To probe the metastable spin configurations below T_c, the isothermal time-dependent relaxation of the magnetization (*TRM*) was measured. The sample was field-cooled through T_c down to 15 K in an applied field of H = 5000 Oe; then the magnetization was measured as a function of time after switching off the magnetic field from t_i = 1 s to t_f = 6000 s. A slow decay of *TRM(t)* at zero field in compound **1** is shown in Fig. 5.8. The finite value of *TRM(t)* after 7000 s indicates frozen spin dynamics transforming spin configurations with time. Initial fit to logarithmic relaxation $TRM(t) = M_0 - S \times log(t)$ was unsuccessful (*TRM* in the inset of Fig. 5.8 significantly deviates from linear behavior) suggesting much slower spin dynamics. Therefore, a modified stretched-exponential decay expression (eq. 6.2) was chosen to model *TRM(t)* dependence, in which a constant term M_0 was added to model a possible remanence that occurs below T_c and coexists with the frozen spin configuration similar to that proposed in Gabay-Toulouse model [177]

$$TRM(t) = M_0 - \eta \times exp\left[-\left(\frac{t}{\tau}\right)^{1-n}\right] \qquad \text{(eq. 6.2)}$$

This approach has been recently used to describe the time-dependent relaxation behavior in diverse systems exhibiting spin glass behavior [178-180] including the quasi-1D cluster-glass molecule-based magnet [Mn(TPP)][TCNE] [181]. The best fit of the experimental *TRM*(*t*) data to the eq. 6.2 (solid line in Fig. 5.8) was achieved using the parameters M_0 = 515 emuOe/mol, η = 1580 emuOe/mol, relaxation time τ = 1300 s, and stretching factor *n* = 0.22.

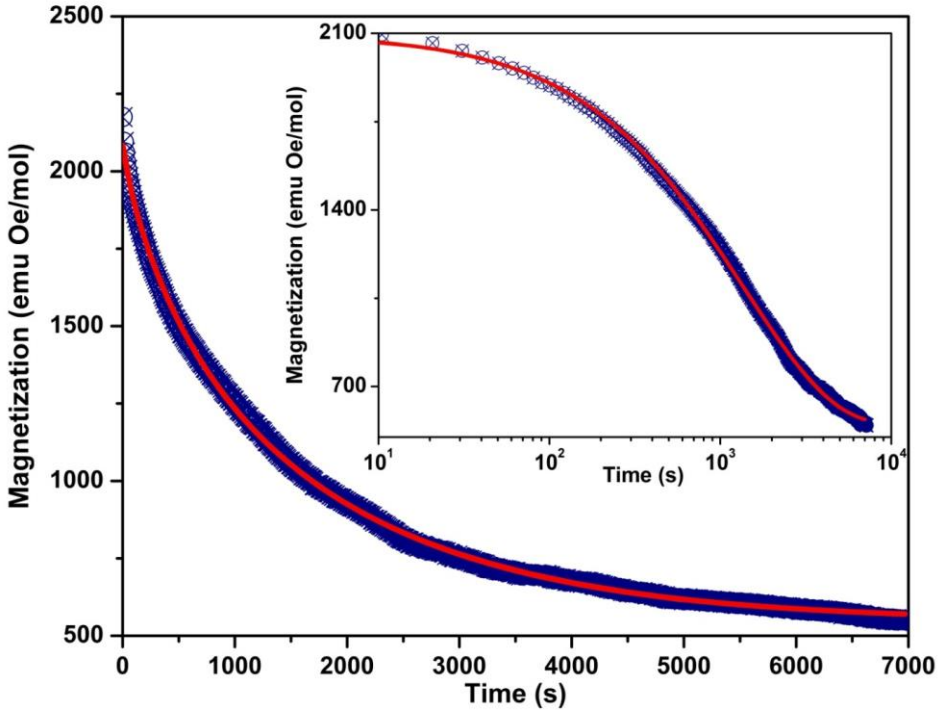

Figure 5.8. Time-dependent TRM results for compound **1** at 15K. The solid line is a stretched-exponential fit for the magnetic relaxation. Inset displays the same data on a logarithmic scale.

The slow relaxation time τ and deviation from Debye type relaxation (*n* = 0) is characteristic of spin-glass systems. The unusually large value of M_0 suggests the existence of a significant permanent remanence in addition to a frozen disordered component of magnetization at low temperatures (vide infra).

5.3.4. Critial Spin Dynamics and Reentrant Transitions

To establish the nature of the low temperature transition, a fitting of the AC susceptibility under dynamic scaling theory was sought. For spin glass systems, frequency dependence of the spin freezing temperature near spin glass transition can be described by a critical slowing down of the spin relaxation time, expressed as $\tau = \tau_0[(T_f - T_G)/T_G]^{-z\nu}$ [32], where τ is the dynamic fluctuation time (related to the experimental AC field frequency ω as $\tau = 1/\omega$ in the vicinity of transition), τ_0 is the microscopic spin relaxation time, T_f is the dynamic spin freezing temperature determined as the peak position in $\chi'(T)$ curve, T_G is the static ($\omega \rightarrow 0$) spin freezing temperature, and $z\nu$ is the dynamical exponent [33-35]. As mentioned above, although T_f of our samples cannot be determined from the $\chi'(T)$ curve, the parameters T_G, τ_0 and $z\nu$ are sought by fitting the $T_{max}(\omega)$ data to the similar equation, $\tau = \tau_0[(T_{max} - T_G)/T_G]^{-z\nu}$, which may be rewritten as

$$\log_{10}(\tau) = \log_{10}(\tau_0) - Z\nu \log_{10}\left(\frac{T_{max}}{T_G} - 1\right) \qquad \text{(eq. 6.3)}$$

In a linear regression fitting to the experimental data, the corresponding log-log plot allowed determination of parameters τ_0 and $Z\nu$, with T_G derived independently by extrapolation of the T_{max} vs. $\log(\omega)$ plot (eq. 6.3) to zero. The variation of $\log(\tau)$ vs. $\log(T_{max}/T_G - 1)$ for $[Mn(TCNE)(NCMe)_2]X$ (X = PF_6^- (**6**), AsF_6^- (**7**), and SbF_6^- (**1**), respectively) series is shown in Fig. 5.9 (a-c). The best fit was obtained with T_G, τ_0, $Z\nu$ values equal to 40.1 K, 3.3×10^{-10} s and 11.7 for **6**; 43.0 K, 2.4×10^{-10} s and 9.2 for **7**; and 40.2 K, 6.8×10^{-10} s and 8.7 for **1**, respectively. Although the actual spin glass freezing temperature T_f cannot be determined from the $\chi'(T)$ curve in the present work, and thus the characteristic parameters T_G, τ_0 and $z\nu$ cannot be estimated from the $T_f(\omega)$ data, the T_G, τ_0 and $z\nu$ values evaluated by fitting the $T_{max}(\omega)$ data to equation 3 strongly suggest the formation of a spin glass state in all materials studied here. The fitting reveals larger

dynamic coefficients, $Z\nu$, and longer relaxation times, τ_0, compared to those reported for canonical spin-glasses ($Z\nu$ = 5 - 10, $\tau_0 = 10^{-10}$- 10^{-13} s) [182]; however, they are in accord with the values obtained in some well-known perovskite-type magnetic oxide SGs [183-185]. Enhanced relaxation times suggest the formation of spin-clusters with a long spin-correlation length near the critical region, which is consistent with the large observed dynamic coefficients as well as M_0 value derived from *TRM* experiment.

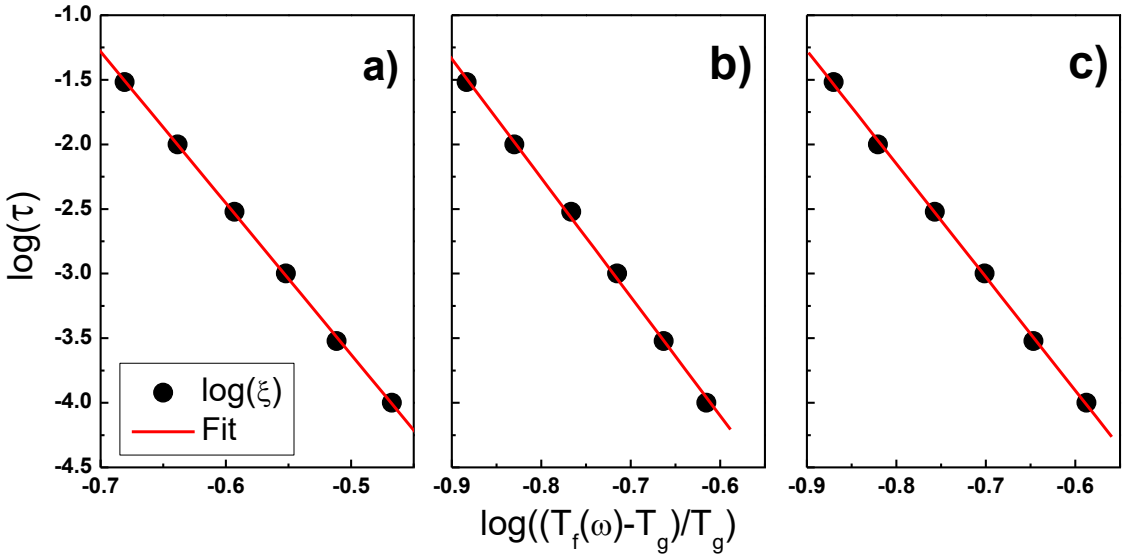

Figure 5.9. The variation of log(τ) vs. log(T_{max}/T_G -1) for [Mn(TCNE)$(NCMe)_2$][X] (X=PF_6^- [**6**, panel a], AsF_6^- [**7**, panel b], SbF_6^- [**1**, panel c]) series. Solid line represents a linear regression fit to the experimental data.

The experimental results clearly suggest that all studied isostructural 2D magnets undergo the transition into a ferrimagnetic state with remanence at 70, 72, and 75 K for **6**, **7**, and **1**, respectively. However, on further cooling these compounds experience another transition into a magnetically disordered SG state at 49, 48 and 46 K, respectively. Consequently, a ferrimagnetic state intervenes between the paramagnetic (at $T > T_c$) and SG states (at $T < T_f$), which is characteristic of reentrant spin-glasses (RSG) and is ascribed to the coexistence of short-range SG ordering and magnetic long-range ordering for the transverse and longitudinal components of magnetization, respectively [177]. The observed features are reminiscent of the

observed reentrant spin-glass behavior in $[Mn^{II}(TCNE)(C_4(CN)_8)_{1/2}]$ [186] but with much more pronounced behavior.

Since the magnetocrystalline anisotropy of the Mn^{II} ion is weak, it was assumed that solely interlayer dipole-dipole interaction may facilitate long-range 3D magnetic ordering in **6-7**, **1** magnets. The dipolar interaction between individual spins belonging to adjacent layers is very small, e.g. the potential energy of dipole-dipole coupling, V, between two Mn^{2+} ions with S_{eff} = 5/2 -1/2 = 2 separated by d = 0.89 nm is about $V/k_B \sim \mu_0\mu^2/4\pi d^3$ = 21 mK (μ_0 - permeability of vacuum, μ - a magnetic moment of Mn^{2+} ion). Conversely, the dipolar interaction can reach a significant strength as soon as spins become correlated in blocks within the layer. Since the spin correlated blocks of size ξ^2 grow exponentially as the temperature decreases, the 3D ordering may occur as soon as the in-plane correlation length ξ reaches a threshold value [169,187]. It was shown that the exponential divergence of ξ defined by in-plane super-exchange is the main reason of weak T_c dependence on the distance between magnetic layers [169].

In all materials studied here, sizable remanence is observed below T_c. However, it remains practically the same (Fig. 5.4) in the range of $45 < T < 65$ K suggesting that the spin-blocks (if they do exist) do not grow exponentially on cooling; otherwise at least 4 fold increase should have been expected. Conversely, the rapid increase of remanence on cooling in the SG state ($T < T_f$) is in accord with divergence of ξ at low temperature predicted by theory [188]. Consequently, the SG ground state in these Mn based magnets suggests that in contrast to layered $Cu_2^{(II)}(OH)_3$-based compounds the dipolar inter-plane interaction in the magnets **6-7**, **1** is not strong enough to secure the long-range magnetic ordering.

It is most likely that the difference in magnetocrystalline anisotropy should be considered the main factor responsible for the striking difference in magnetic properties of structurally similar

Fe^{II} and $Mn^{II}(\mu_4\text{-}TCNE^{\bullet-})$ layer compounds. For very thin magnetic films, it has been shown that a homogeneously magnetized state becomes unstable if the magnetocrystalline anisotropy is too small to pull the magnetization out of the film plane [168]. It is conceivable to assume that this statement is valid for the 2D $Mn^{II}(\mu_4\text{-}TCNE^{\bullet-})$ layers. However, the small magnetocrystalline anisotropy observed below the critical temperature ($g \neq 2$) could be sufficient to produce a non-zero magnetization component perpendicular to the layer as the material approaches the transition.

Numerous studies of both metallurgical reentrant spin glass alloys (e.g. Au-Fe [189]), disordered perovskites [185] as well as Heusler alloys [190] have shown that Gabay-Toulouse model provides a consistent basis for understanding the magnetic order in these materials. In $[Mn^{II}(TCNE)(NCMe)_2]X$ magnets the high-temperature transition at T_c likely marks the onset of a long range ordering of the magnetic moment components normal to the plane, while in-plane components remain in precession. At T_f the in-plane components freeze randomly ("canting transition"), so that the modulus of the total moment shows an anomalous increase, in accord with experimental observations. However, the normal ferimagnetic component continues to increase as temperature is lowered in accord with *TRM* results. However, while a phase transformation, which in principle might introduce a reversible structural disorder (e.g., $Mn^{II}(\mu_4\text{-}TCNE^{\bullet-})$ layer corrugation fluctuations) resulting in time dependent magnetization, could not be definitively ruled out, the small magneto-crystalline anisotropy of Mn ion makes this scenario very unlikely.

As mentioned above, the RSG behavior was observed for the quasi-3D $[Mn^{II}(TCNE)(C_4(CN)_8)_{1/2}]$ compound, which features a similar $Mn^{II}(\mu_4\text{-}TCNE^{\bullet-})$ type layered structure with additional apical coordination of the Mn^{II} through a diamagnetic $[TCNE]_2^{2-}$ dimer

providing a weak interlayer coupling [172]. Conversely, the recently discovered 3D molecular magnet $[Mn^{II}(TCNE)_{1.5}](I_3)_{0.5}$ (also possessing a $Mn^{II}(\mu_4\text{-}TCNE^{\bullet-})$ layered motif with the layers linked via another μ_4-$TCNE^{\bullet-}$ moiety) exhibits a magnetic behavior very similar to that of $[Fe^{II}(TCNE)(NCMe)_2]FeCl_4$ suggesting the stabilization of long-range magnetic ordering at T_c = 170 K. Apparently, an exchange between layers involving the TCNE anion spin-density totally suppresses the RSG behavior despite the weak Mn^{II} magneto-crystalline anisotropy.

5.4. Conclusions

The systematic structural, spectroscopic, and magnetic characterization of a series of $[Mn^{II}(TCNE)(NCMe)_2]X$ complexes (X = PF_6, AsF_6, SbF_6) has shown that dipolar interaction is not the primary contributor to 3D magnetic ordering in these materials, while the magnetocrystalline anisotropy could be the main factor responsible for the difference in magnetic properties of layered molecular magnets. The observed RSG behavior was interpreted in terms of subsequent long range ordering and spin-glass transitions of normal and in-plane components of magnetization.

6. DFT MODELING OF MAGNETIC AND ELECTRONIC STRUCTURE FOR 2D AND 3D NETWORKED Mn[TCNE] MAGNETS

6.1. Introduction

For several decades magnetism in the solids containing 3d electrons has remained one of the main focuses of modern condensed matter physics. In contrast to the itinerant ferromagnetic exchange between almost free electrons in metals (*direct exchange*), the main mechanism of exchange interaction in magnetic insulators like simple transition metal oxides, is *a virtual hopping* of electrons between almost isolated ions (metal and oxygen) leading to an anti- or ferromagnetic Heisenberg exchange interaction between unpaired spins of metals, traditionally defined as the *indirect*- or *superexchange* [38,45,46].

The idea that the spin ordering in M[TCNE] magnets results from a strong antiferromagnetic (AFM) exchange between unpaired spins residing on the metal 3d orbitals and delocalized unpaired *p* electrons (S = 1/2) residing on the π* molecular orbital of $TCNE^{\bullet-}$ [99] has been confirmed by numerous magnetic studies of M[TCNE] magnets (see the recent reviews [13,43,95,191,192] and references therein). Since the neutron diffraction studies of $TCNE^{\bullet-}$ demonstrated that ~1/8 of the unpaired electron density resides on each N≡C group of $TCNE^{\bullet-}$ [122], it is conceivable to assume that there exists a weak hybridization (direct exchange) between symmetry allowed 3d half-filled orbitals of metal and single occupied π* molecular orbitals (SOMOs) of $TCNE^{\bullet-}$. Earlier it was proposed that the ferrimagnetic ground state in the most studied M[TCNE] species, $V[TCNE]_x$ (T_c = 400 K), arises due to weak electron hopping (superexchange) between the V^{II} 3d sites via the π* orbital of $TCNE^{\bullet-}$ [100]. Conversely, the analysis of XAS and XMCD results on the same material using ligand field multiplet calculation

(LMC) approach suggests that the V^{II} 3d ground state consists of 60% $3d^3$ and 40% $3d^4\underline{L}$ ($\underline{L}$ = hole on $TCNE^{\bullet-}$ ligand), implying that there exists a hybrid state with substantial ligand to metal charge transfer [91]. Therefore, the question of whether the origin of magnetic ordering should be attributed to a virtual hopping of electrons between the nearest neighbor 3d metal cations mediated by the $TCNE^{\bullet-}$ π^* orbital or by direct $TCNE^{\bullet-}$ π^* and M-3d orbital overlap remains unanswered. Considering that there is no clear experimental evidence to support one mechanism over the other, the electronic structure modeling via ab-initio methods is an essential tool in interpreting the experimental observations, as well as establishing structure-properties correlations. Recent computational studies on hypothetical V[TCNE] structures have successfully reproduced some experimental features of $V^{II}[TCNE]_x$ ($x \sim 2$) such as significant antiferromagnetic spin coupling and semiconducting band gap, as discussed in Chapter 2. However, these simulations lack a detailed assignment of the orbital mixing or hybridization of V^{II} and $TCNE^{\bullet-}$ in the magnetic ground state, and could not elucidate the impact of structural and magnetic dimensionality on magnetic spin coupling.

In contrast to the use of hypothetical simulation structures, the recent structural characterization of Mn[TCNE] based MBMs of varying coordination dimensionality, i.e. the 2D layered structure $[Mn^{II}(TCNE)(NCMe)_2]SbF_6$ (T_c = 70 K, compound **1**) and the fully 3D-networked $[Mn^{II}(TCNE)_{1.5}](I_3)_{0.5}$ (T_c = 170 K, compound **5**), [82, 85] provides a rigorous experimental basis to investigate theoretically the magneto-structural correlation leading to enhanced magnetic interaction. Herein, an extensive computational characterization of the spin-polarized electronic structure, magnetic coupling, and orbital hybridization characteristics of experimentally characterized Mn[TCNE] MBMs is reported. With this approach, the nature of

magnetic coupling enhancement in structurally related Mn[TCNE] complexes is investigated, and new information about magnetic exchange pathways in this MBM class is revealed.

6.2. Computational Details

All DFT calculations were performed using commercial software program VASP, version 5.2.1 [193-195] utilizing the HSE06 functional. Core electrons were treated by a projector augmented wave (PAW) pseudopotential. The plane-wave basis set was used to expand the wavefunctions up to a kinetic energy cutoff value of 500 eV.

The crystal structures of $[Mn^{II}(TCNE)(NCMe)_2]SbF_6$ and $[Mn^{II}(TCNE)_{1.5}](I_3)_{0.5}$ MBMs were used as initial geometries [196,197]. In the latter compound (**5**) [85], an interstitial C_4H_4O (THF) (~0.5 molecule per formula unit) was identified. Since the THF position in the unit cell was defined with large uncertainty and no short contacts were found between THF and other molecules, it was removed from the unit cell used for DFT modeling. The structure was then fully optimized allowing a full relaxation of ionic and unit-cell parameters using a conjugate-gradient algorithm with convergence criterion of $\Delta E = 10^{-3}$ eV/Å. The full experimental crystal structure of **1** [35] was optimized following the same approach and convergence tolerance. For geometry optimizations, a Γ-point only sampling scheme is used. For electronic structure analysis, a Γ-centered Monkhorst-Pack grid [198] with 2×2×2 *k*-point sampling of the Brillion zone was used, yielding 4 and 12 unique *k*-points for the HSE-optimized compounds **1** and **5**, respectively. The spin-polarized Kohn-Sham eigenvalues were converged self-consistently for the optimized structures using an electronic wavefunction convergence criterion of $\Delta E = 10^{-4}$ eV. Partial occupancy of electronic states was treated by sampling the Brillouin zone using the linear tetrahedron method with Blöchl corrections [199]. The broken-symmetry magnetic

configurations [200,201] were structurally relaxed separately and converged self-consistently from a spin-unconstrained initial guess, d^5 high-spin configuration assigned to each Mn^{II} ion in the calculation cell, using the same DFT methodology reported above. This approach ensures comparability between the ground and higher-symmetry spin state energies.

6.3. Results and Discussion

6.3.1. Crystalline and Magnetic Ordering

In the 2D layered $[Mn(TCNE)(MeCN)_2]SbF_6$ magnet (**1**, Fig. 6.1a), each Mn^{II} cation is coordinated to four (:N≡C-) nitrile groups of TCNE anions within the layer ($Mn^{II}(\mu_4\text{-}TCNE^{\bullet-})$ motif) and possesses charge-balancing anions intercalated between layers, which exhibit no covalent bonding or short contacts that could facilitate an interlayer magnetic exchange [196,202]. Compound **5** is the recently discovered molecular magnet $[Mn^{II}(TCNE)_{1.5}](I_3)_{0.5}$ [197], in which each Mn^{II} ion is octahedrally coordinated to six (:N≡C-) nitrile groups of TCNE anions (Fig. 6.1c). This structure maintains the similar $Mn^{II}(\mu_4\text{-}TCNE^{\bullet-})$ corrugated plane motif, but additionally possesses cross-linking between 2D planes by a $\mu_4\text{-}TCNE^{\bullet-}$ moiety.

The experimental structural parameters for the studied **1** and **5** compounds are compared to the ones after geometry optimization in Table 6.1. The geometry optimization results in only a slight relaxation of the unit cells from the experimental orthorhombic ones to triclinic Bravis lattices. In compound **1** the cell along ***b*** relaxes by ~0.66 Å (4.1%), most likely due to steric interaction between the large SbF_6^- anion density and the positively charged $Mn^{II}(\mu_4\text{-}TCNE^{\bullet-})$ layers. For compound **5**, a contraction of ~0.1 Å (0.7%) is seen for the ***a*** axis, possibly due to removal of the uncoordinated interstitial THF solvent molecule.

It should be noted that the structural motif for compound **5** slightly distorts the octahedral environment around the Mn^{II} ions. These features are preserved upon optimization, though exhibit a slight rearrangement through the small closing of angles $\angle N_1\text{-}Mn\text{-}N_2$ (expansion of $\angle N_2\text{-}Mn\text{-}N_3$). Despite this small re-configuration, the Mn-N bond lengths remain in good agreement with the experimental values for both compounds. These small deviations represent a departure from an idealized octahedral O_h point group symmetry for the metal coordination environment, which is expected to result in degeneracy breaking of the electronic levels. Nevertheless, for convenience the symmetry descriptions of this point group will be used when characterizing electronic structure results below. Upon optimization, the organic moieties in both compounds relax from the values found in the experimental structures, with noticeable extension of both the C=C and C≡N bonds. However, these converged geometries remain in good agreement with the optimized structure of the isolated uncoordinated $TCNE^{\bullet-}$ radical molecule (Table 6.1.) and those previously reported for simulations of $V[TCNE]_x$ magnets [144]. The ground-state spin-density iso-surfaces that are spatially overlaid with the crystal structures of **1** and **5** are shown in Fig. 6.1b and d, respectively. The surfaces are defined as a difference between α spin-up ($\rho\uparrow$) and β spin-down ($\rho\downarrow$) densities and displayed at a level of 9×10^{-3} e^-/a_o^3. The surfaces reveal a spherical distribution of excess α spin density primarily localized around the Mn^{II} ion due to a high-spin occupancy of the e_g- and t_{2g}-like electronic states. A calculated spin-density of 4.56 and 4.54 |e| residing on each Mn^{II} was found for **1** and **5** respectively, in accord with the expected five unpaired electrons in high-spin Mn^{II}. The minority β spin density is delocalized over the $TCNE^{\bullet-}$ ligand, and its shape is consistent with π* orbital, i.e., the density antinodes on the nitrogens of nitrile-groups and vinyl carbons with a zero-density node at the center of the C=C double bonds.

Table 6.1. Structural parameters for the experimental and DFT optimized geometries of the complexes $[Mn^{II}(TCNE)(NCMe)_2]SbF_6$ (**1**) and $[Mn^{II}(TCNE)_{1.5}](I_3)_{0.5}$ (**5**) considered in this study. DFT structure factors here correspond to optimized geometries in the magnetic ground-state configurations $\boldsymbol{E_{2D}^1}$ and $\boldsymbol{E_{3D}^1}$.

	$[Mn^{II}(TCNE)(NCMe)_2]SbF_6$		**$[Mn^{II}(TCNE)_{1.5}](I_3)_{0.5}$**		**$TCNE^{\bullet-}$**	
Parameter (Å, degree)	***Exp.***	***Opt.*** ([e] $\boldsymbol{E_{2D}^1}$)	***Exp.***	***Opt.*** ([e] $\boldsymbol{E_{3D}^1}$)	[c] ***Exp.***	[d] ***Opt.***
a	7.192	7.214	13.170	13.075	∅	12.019
b	16.293	16.968	15.926	16.030	∅	11.557
c	14.942	14.920	7.608	7.657	∅	7.800
α	90.00	90.01	90.00	89.91	∅	90.00
β	90.00	89.97	90.00	90.03	∅	90.00
γ	90.00	89.69	90.00	89.99	∅	90.00
C=C (eq.)	1.38	1.42	1.34	1.42	1.34	1.43
[a,b] C=C (ap.)	∅	∅	1.34	1.42	∅	∅
C≡N (eq.)	1.119	1.16	1.16	1.16	1.21	1.16
[a] C≡N (ap.)	1.119	1.16	1.16	1.16	∅	∅
Mn-N (eq.)	2.23	~2.22	2.21	~2.21	∅	∅
[a] Mn-N (ap.)	2.19	2.21	2.18	2.20	∅	∅
$\angle N_1$-Mn-N_2	92.98	92.68	95.89	93.73	∅	∅
$\angle N_2$-Mn-N_3	87.02	87.395	84.11	86.27	∅	∅

[a]Structure **1**'s 2D motif possesses apical coordination by the nitrile group of the acetonitrile ligand (c.f. figure 6.1a, 6.11c)
[b]Refering to C=C bond of apically coordinated TCNE ligand, found only in **5** (c.f. figure 1a, 1c)
[c]Taken from $Bu_4N[TCNE]^{\bullet-}$ molecular crystal, see text.
[d]Simulation cell for lone $TCNE^{\bullet-}$ molecular radical, cell geometry not to be compared with that of $Bu_4N[TCNE]^{\bullet-}$
[e]Geometric factors taken from the structurally optimized ground-state magnetic configuration

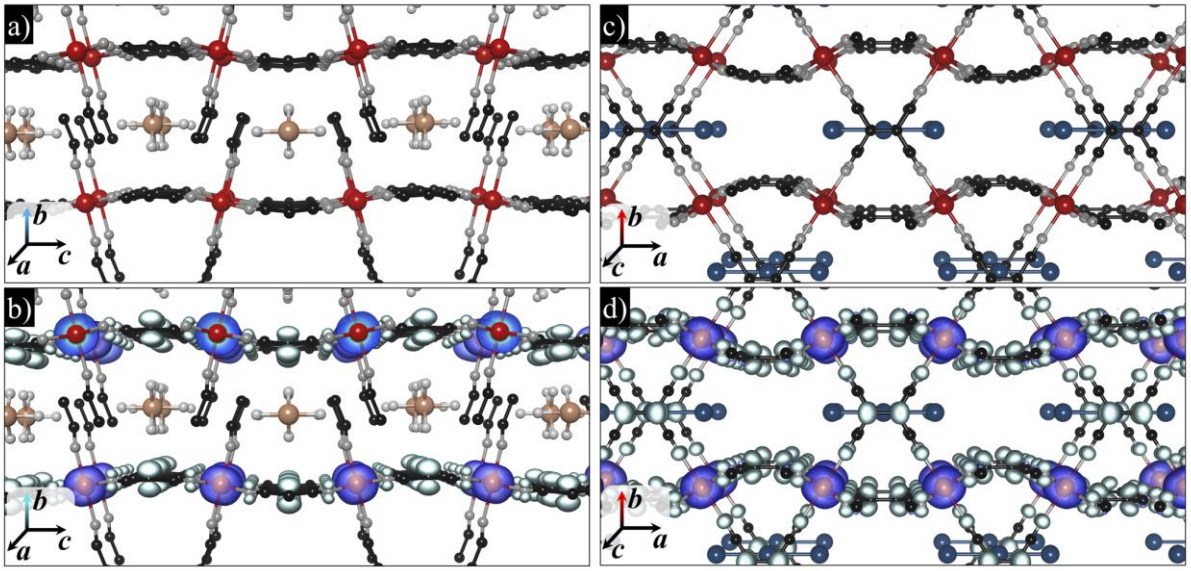

Figure 6.1. Geometry optimized crystal structures (panels a, c) and calculated spin-density distribution manifolds (panels b, d) in $[Mn^{II}(TCNE)(MeCN)_2]SbF_6$ (**1**) and $[Mn^{II}(TCNE)_{1.5}](I_3)_{0.5}$ (**5**) magnets with two- and three- dimensional magnetic interaction, respectively (C – black; N – grey; Mn – red; Sb – tan; I – dark teal; F – white, H – for clarity, not shown).

As expected, in **1** the effective magnetic spins are confined to the two-dimensional $Mn^{II}(\mu_4\text{-}TCNE^{\bullet-})$ plane. In contrast, compound **5** contains two crystallographically inequivalent $Mn^{II}(\mu_4\text{-}TCNE^{\bullet-})$ coordination planes, denoted as "equatorial" and "apical", which contribute to the spin density distribution (Fig. 6.1d). In the "equatorial" $Mn^{II}\text{-}N_4$ plane, which extends in the ***a*-*c*** crystallographic plane, the adjacent octahedra are canted by 37° clockwise or counter clockwise (the angle between the plane and ***b***-axis). The Mn-N≡C angle decreases from 180 to 157° causing a significant warping of the $Mn^{II}(\mu_4\text{-}TCNE^{\bullet-})$ plane (see Fig 6.1c). In contrast, for apically coordinated ligands, the Mn-N≡C angle is 173°, which is close to that of a slightly warped "equatorial" plane in **1** (169°). This coordination motif creates a second undistorted (planar) $Mn^{II}(\mu_4\text{-}TCNE^{\bullet-})$ layer in the crystallographic ***a*-*b*** plane and bridges the warped ***a*-*c*** plane layers.

Despite the significant topological differences between the planar and apical TCNE moiety in this structure, little change is observed in the ground state magnetic spin density distribution. These results support the hypothesized stabilization of AFM ordering between localized Mn^{II}-3d and π* $TCNE^{\bullet-}$ electrons, in accord with the low temperature saturated magnetization studies [196, 202]. Thus, our DFT simulations confirm the AFM ground state for both the **1** and **5** Mn[TCNE] magnets.

6.3.2. Evaluation of Magnetic Coupling Values

The experimentally observed T_c value of **1** is more than twice as small as that of the **5** magnet (70 and 170 K, respectively). It suggests that the interlayer coupling introduced via spin-bearing ligand coordination pathways causes a significant enhancement of magnetic T_c. The interaction energy between two spin vectors may be used to estimate the strength of magnetic interaction. The Heisenberg Hamiltonian $\mathcal{H} = -\sum_{i<j} J_{ij} \boldsymbol{S}_i \bullet \boldsymbol{S}_j$ is commonly used to deduce nearest-neighbor coupling strength J_{ij}. For the system of two equivalent magnetic centers, the J value can be calculated from DFT using the relative energies of the possible configurations of the projected spin-multiplets in the Ising limit, otherwise known as the broken-symmetry approximation[200]. This approach is widely used as a measure of magnetic coupling strength between two spin-bearing bodies in the DFT formalism, and was applied most recently in other M[TCNE] studies investigating the particulars of the exchange interactions therein [108,144,203]. Adopting this approach for the **1** and **5** structures, the following spin Hamiltonians are defined, respectively:

$$\mathcal{H}_{\boldsymbol{2D}} = -4J_{eq}S_{3d}S_{eq} \qquad \text{(eq. 6.1)}$$

$$\mathcal{H}_{\boldsymbol{3D}} = -4J'_{eq}S_{3d}S_{eq} - 2J_{ap}S_{3d}S_{ap} \qquad \text{(eq. 6.1)}$$

These Hamiltonians adequately reflect the antiferromagnetic structure suggested by the ground state spin-density distribution described above. In **1** a gently corrugated $Mn^{II}(\mu_4\text{-}TCNE^{\bullet-})$ layer in the ***a-c*** crystallographic plane that contains Mn^{II} centers *equatorially* bound by four TCNE moieties, with diamagnetic acetonitrile (MeCN) solvent molecules capping in the apical position (Fig. 6.1a). Therefore, magnetic interaction solely between Mn^{II}-3d ($\boldsymbol{S}_{3d}$) and π*-$TCNE^{\bullet-}$ ($\boldsymbol{S}_{eq}$) spins within this 2D layer is anticipated, described by the coupling parameter J_{eq} in eq. 6.1. In compound **5**, the layered-structure in the ***a-c*** crystallographic plane is similar to that of **1**, while being significantly more warped; yielding a J'_{eq} coupling in eq. 6.2. The interlayer coupling in the ***a-b*** crystallographic plane through the additional spin-bearing $TCNE^{\bullet-}$ ligands *apically* bonded to Mn^{II} ions in the adjacent layers (Fig. 6.1c) is taken into account by introducing the additional interaction term J_{ap} in $\mathcal{H}_{3D}$ in eq. 6.2.

Application of these Hamiltonians to the broken-symmetry magnetic configurations listed in Table 6.2 (first column) gives the expression for the system energies in different spin states (columns 2-4) for both compounds. Conversely, the broken-symmetry spin-state energies and corresponding relaxed structural geometries have been computed via DFT modeling for complexes **1**, **5**. Broken-symmetry energies with respect to that of the AFM ground state are listed in the last column of Table 6.2, while structural factors corresponding to the broken-symmetry states are found in Table 6.3 and 6.4. Solving the systems of equations (first column in Table 6.2) using a least squares fitting of the Hamiltonian reveals the exchange values of J_{ap} = -29.50 meV, J'_{eq} = -37.19 meV for compound **5**, and J_{eq} = -23.74 meV for the two-dimensional layered compound **1.** Recently, mean-field formulas based on the simple Heisenberg model were proposed, thus allowing the correlation of inter- and intra-layer exchange coupling to the critical temperature, T_c, for several M[TCNE] MBMs with extended 2D and 3D structures [204]. Using

DFT-calculated J values for the compounds **1** and **5** and the structures' corresponding T_c expressions [204], the corresponding critical temperature values of T_c^{2D} ~ 941 K and T_c^{3D} ~ 1690 K have been derived.

Table 6.2. The relative energies of the allowed spin configurations in magnets **1** and **5**.

Configuration	S_1–Mn^{II} *3d*	S_2–$TCNE_{eq}$ π*	S_3–$TCNE_{ap}$ π*	ΔE ($\|E^N - E^1\|$)
$[Mn^{II}(TCNE)(NCMe)_2]SbF_6$ (1)				
$E_{2D}^1 = 7J_{eq}$	↑ (5/2)	↓ (1/2)	∅	0 eV
$E_{2D}^2 = -5J_{eq}$	↑ (5/2)	↑ (1/2)	∅	0.2849 eV
$[Mn^{II}(TCNE)_{1.5}](I_3)_{0.5}$ (5)				
$E_{3D}^1 = 5J'_{eq} + \frac{5}{2}J_{ap}$	↑ (5/2)	↓ (1/2)	↓ (1/2)	0 eV
$E_{3D}^2 = 5J'_{eq} - \frac{5}{2}J_{ap}$	↑ (5/2)	↓ (1/2)	↑ (1/2)	0.1508 eV
$E_{3D}^3 = -5J'_{eq} + \frac{5}{2}J_{ap}$	↑ (5/2)	↑ (1/2)	↓ (1/2)	0.3752 eV
$E_{3D}^4 = -5J'_{eq} - \frac{5}{2}J_{ap}$	↑ (5/2)	↑ (1/2)	↑ (1/2)	0.5194 eV

The estimated values about an order of magnitude exceed those obtained experimentally [197, 205]. The discrepancy likely occurs due to overlooked thermal fluctuations and the possible FM exchange channels involving Mn 3d-e_g derived electrons that may weaken kinetic exchange resulting in lower T_c [206]. However, these DFT-derived J values at least on a semi-quantitative level describe well the changes in experimentally observed T_c in Mn[TCNE] magnets due to the increase of the dimensionality of magnetic exchange. Previously it was shown that the ∠M-N≡C bond angle value, and hence the degree of 3d-π* overlap, exhibits a clear correlation: more this angle deviates from the ideal 180°, the larger the 3d-π* overlap and corresponding J value [107, 207-209]. An almost 70 % increase of J_{eq} in the **5** magnet with

respect to that in **1** is in accord with a substantially smaller ∠M-N≡C bond angle in the former. It should be noted that the J coupling constants are significantly smaller in both Mn[TCNE] magnets than those evaluated via similar DFT-based analysis of the high-T_c V[TCNE]$_x$ (x~2, T_c ~ 400 K) magnet, assuming a hypothetical 3D network structure [113] in accord with the experimental observations. This suggests the validity of the hybrid-DFT broken-symmetry approach for the exchange mechanism study.

Table 6.3. Structural parameters for the experimental and DFT optimized geometries of the $[Mn^{II}(TCNE)_{1.5}](I_3)_{0.5}$ (**5**) complex. DFT structure factors ("Opt.") correspond to optimized geometries from spin configurations labeled $\boldsymbol{E_{3D}^{N}}$ from Table 6.1.

	$[Mn^{II}(TCNE)_{1.5}](I_3)_{0.5}$				
Parameter (Å, degree)	***Exp.***	***Opt.*** (^{b} $\boldsymbol{E_{3D}^{1}}$)	***Opt.*** (^{b} $\boldsymbol{E_{3D}^{2}}$)	***Opt.*** (^{b} $\boldsymbol{E_{3D}^{3}}$)	***Opt.*** (^{b} $\boldsymbol{E_{3D}^{4}}$)
a	13.170	13.075	13.075	13.090	13.095
b	15.926	16.030	16.090	15.994	16.084
c	7.608	7.657	7.633	7.683	7.668
α	90.00	89.91	89.95	89.92	89.96
β	90.00	90.03	90.08	90.06	90.06
γ	90.00	89.99	90.00	90.01	90.00
C=C (eq.)	1.34	1.42	1.42	1.43	1.43
[a] C=C (ap.)	1.34	1.42	1.42	1.42	1.42
C≡N (eq.)	1.16	1.16	1.16	1.16	1.16
[a] C≡N (ap.)	1.16	1.16	1.16	1.16	1.16
Mn-N (eq.)	2.21	2.21	2.21	2.23	2.23
[a] Mn-N (ap.)	2.18	2.20	2.21	2.19	2.22

[a]Refering to C=C and Mn-N bonds of apically coordinated TCNE ligand in the ***a-b*** crystallographic plane.
[b]Geometric factors taken from the structurally optimized magnetic configurations given in Table 6.1.

Table 6.4. Structural parameters for the experimental and DFT optimized geometries of the complexes $[Mn^{II}(TCNE)(NCMe)_2]SbF_6$ (**1**). DFT structure factors ("Opt.") correspond to optimized geometries from spin configurations labeled $\boldsymbol{E_{2D}^{1}}$ and $\boldsymbol{E_{2D}^{2}}$ from Table 6.1.

	$[Mn^{II}(TCNE)(NCMe)_2]SbF_6$		
Parameter (Å, degree)	***Exp.***	***Opt.*** (^{b} $\boldsymbol{E_{2D}^{1}}$)	***Opt.*** (^{b} $\boldsymbol{E_{2D}^{2}}$)
a	7.192	7.214	7.192
b	16.293	16.968	16.293
c	14.942	14.920	14.942
α	90.00	90.01	90.01
β	90.00	89.97	89.97
γ	90.00	89.69	89.69
C=C (eq.)	1.38	1.42	1.42
C≡N (eq.)	1.119	1.16	1.16
[a] C≡N (ap.)	1.119	1.16	1.15
Mn-N (eq.)	2.23	~2.22	2.21
[a] Mn-N (ap.)	2.19	2.21	2.22

[a]Structure **1**'s 2D motif possesses apical coordination by the nitrile group of the acetonitrile ligand (c.f. figure 6.1a, 6.1c)
[b]Geometric factors taken from the structurally optimized magnetic configurations given in Table 6.1.

6.3.3. Electronic Structure Analysis

Details regarding the nature and degree of hybridization between individual spin-host's electronic levels are crucial to understanding basic magnetic interaction in MBMs. This information may be obtained via careful investigation of the spin-resolved Kohn-Sham eigenstates. The band decomposed density of states (DOS) for complexes **1** and **5** are shown in Fig. 6.2 (panel a, b respectively).

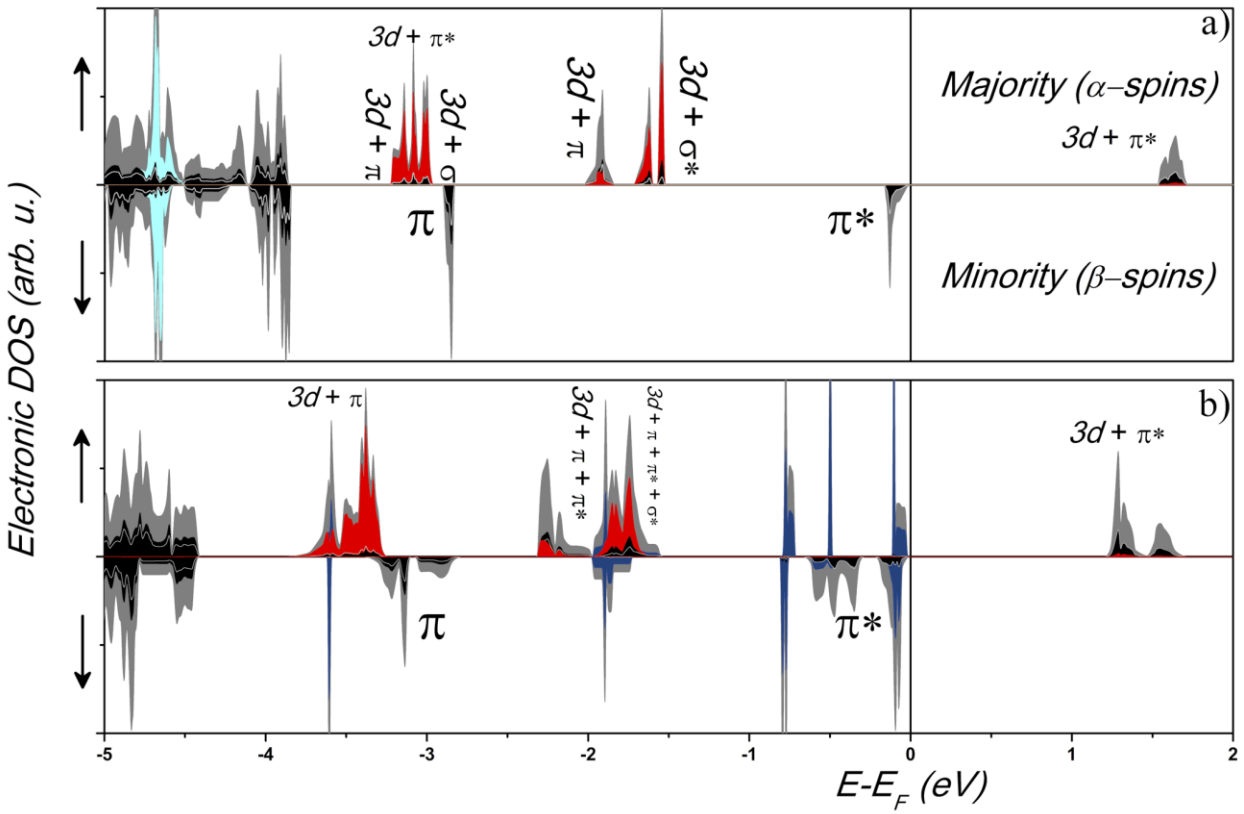

Figure 6.2. Orbital decomposed density of states for complex **1** (a) and **5** (b) (C (p) – black; N (p) – white; Mn (d) – red; Sb (s+p) – cyan; I (s+p) – dark teal; Total – grey).

For complex **1**, unpolarized bands are identified below -4 eV with strong π ligand character. These bands are related to the ligand states (both TCNE and capping acetonitrile) that occur due to σ-type donation of lone pair electron density from TCNE ligand nitrile groups. In -(3.0–1.5) eV region of the α-spin, the expected octahedral crystal field split Mn derived d-bands (e_g and t_{2g}) are revealed. The observed intra-band splitting within the e_g/t_{2g} degenerate bands presumably results from the compression of the apical Mn-N bonds in contrast to the equatorial ones leading to degeneracy lifting beyond the one expected from pure O_h coordination symmetry. This is reminiscent of the d-state effects of the Jahn-Teller splitting in Heusler-type complexes. The t_{2g} manifold near -3.3 eV is predominantly of Mn^{II} character; however, the

presence of the ligand contribution (both carbon and nitrogen) suggests the metal-ligand orbital overlap or hybridization that is also clearly seen.

The nature of this hybridization is visualized via density-decomposition of the total Kohn-Sham wave function and is shown in Fig. 6.2. The t_{2g}-like manifold reveals a complex and nontrivial hybridization of ligand states. In the lowest energy manifold component the characteristic 3d-π type hybridization is revealed primarily between electron density localized on the π-type orbitals of the TCNE moiety (see Fig. 6.3a).

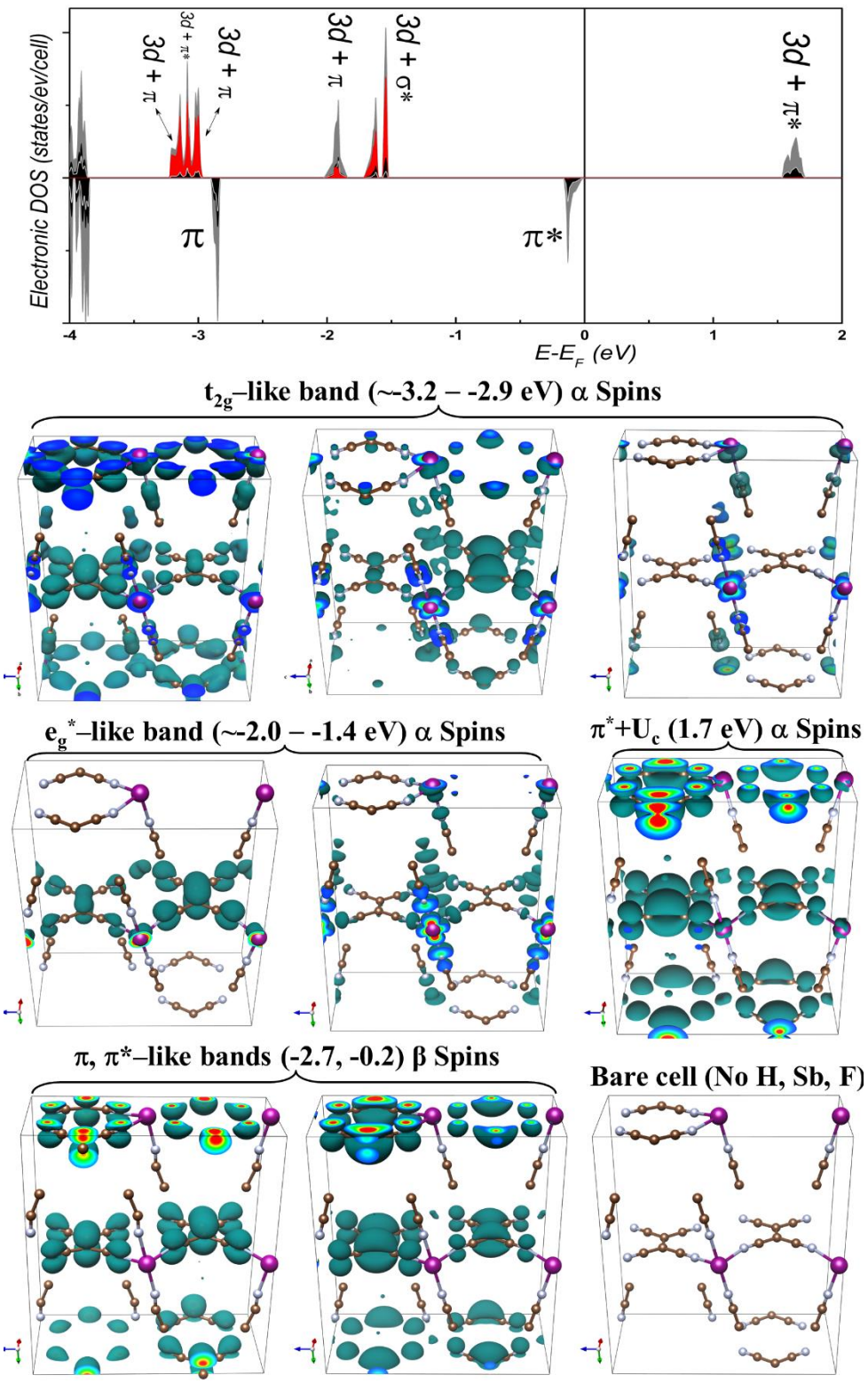

Figure 6.3. a-i. Orbital projected DOS and representative eigenstates for 2D. (DOS: C – black, N – grey, Mn – red, total – dark grey; Scheme: C – brown, N – grey, Mn – purple, H, SbF_6 – For clarity, not shown).

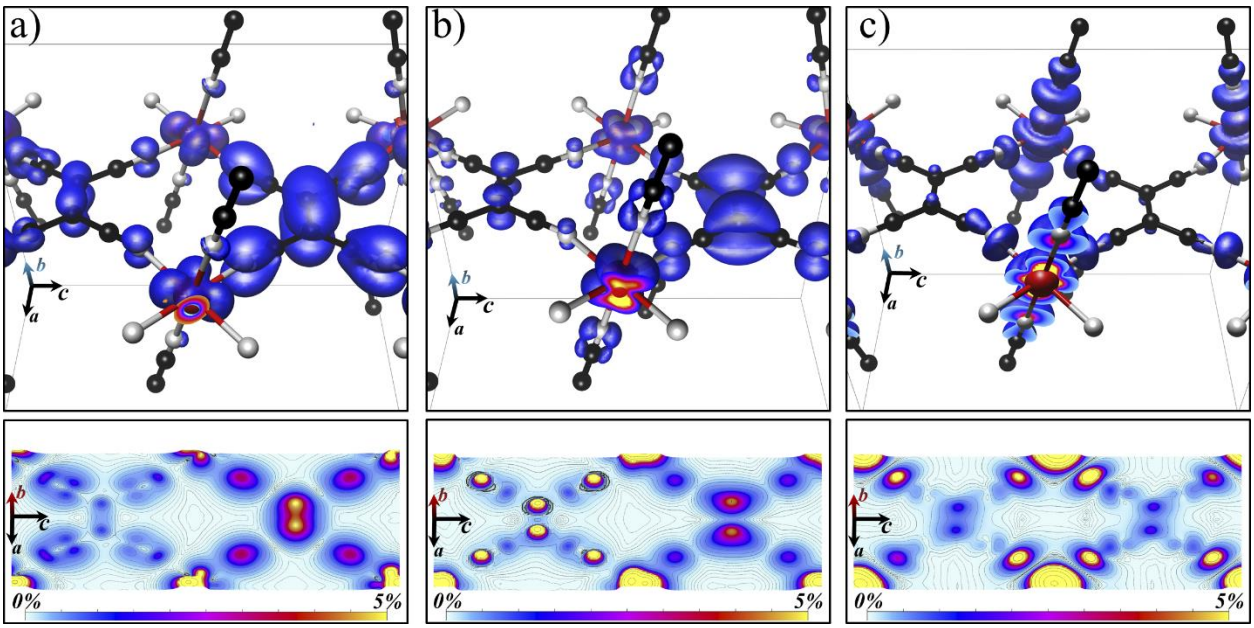

Figure 6.4. The representative fragments of α-spin eigenstates for **1** in -(3.2–2.9 eV) range that are characteristic of Mn 3d-π (a), Mn 3d-π^* (b), and Mn 3d-d_z^2-σ MeCN (c) types of hybridization. Bottom panels display a two-dimensional slice through the *ac* plane, mapped with electron density profiles of the representative eigenstates. The slices are mapped with the eigenstate electron density profile and saturate at 5% of the maximal electron density value. Here, the fine details of the characteristic eigenstate topologies just described (π bonding (a), π^* antibonding (b), lone-pair Mn 3d hybridization (c)) can be clearly observed. Contours form a guide to the eye for the density profile.

The highest energy component of the three-pronged manifold shows a very weak σ-type overlap of the Mn d_{z^2}-type orbitals and lone-pair p_z-orbitals of MeCN capping ligands that are localized on its nitrile group. In the central component of this manifold about one third of all states exhibits a strong electronic mixing between the Mn 3d and the $TCNE^{\bullet-}$ π^* orbitals, which is most likely responsible for the AFM ordering via a direct exchange (Fig. 6.4b). This finding is in accord with the experimentally observed ~0.1|e| ligand-to-metal charge transfer in this compound [80]. In contrast to the 3d-π* hybridization, a similar 3d-π type of overlap involving primarily the Mn 3d and $TCNE^{\bullet-}$ orbitals, albeit with more equal contribution from metal and ligand, is observed in two-component e_g-derived manifold near -2.0 eV. As expected, the iso-

surfaces in Fig. 6.4c exhibit a hybridization of σ-type of 3d-d_z^2 derived Mn and lone-pair electron orbitals of the nitrile groups from the coordinating MeCN solvent.

Two bands are revealed in the (quasi) valence region of the β-channel, i.e. the π character band near -2.8 eV and the π^* character band near -0.2 eV (both derived from the TCNE ligand), as is shown in Fig. 6.3 g-h, respectively. The singly occupied π^* orbitals reside in the β-channel in accord with the AFM ground state predicted by the DFT simulation. These β-spin π^* levels yield no observable hybridization with the 3d metal orbital density, in contrast to the 3d-π^* (Fig. 6.4b). The α-spin TCNE π states exhibit a small energy stabilization lower energy side shift of ~0.2 eV (from its β-spin counterpart) most likely due to the α-density hybridization with Mn^{II}-3d orbitals as discussed above. No sign of 3d-π hybridization was found in the β-spin counterpart.

It should be noted that the *d*-electron correlations in crystals are well described by the Hubbard model [45], which takes into account the effect of on-site Coulomb repulsion between electrons, *U*. The model predicts that the conduction band will split into two oppositely spin-polarized subbands (one half-occupied and one empty) with an energy gap of ~*U*, which leads to a half-semiconducting behavior. Indeed, the correspondent unoccupied $\pi^* + U$ Hubbard subband is observed at +1.6 eV in α-spin channel. The splitting *U* of ~1.8 eV is in accord with the experimentally derived value (2.0 eV) [210] suggesting an accurate account of electronic Coulomb correlation by the HSE06 functional, as sought. The $\pi^* + U$ Hubbard subband exhibits an expected π^* character but with small contribution of the 3d type density from the Mn centers, indicative of the orbital overlap between the partially occupied 3d and π^* states as predicted (Fig. 6.3f).

The DOS pattern for **5** (Fig. 6.2b) exhibits similar features found in **1**. However, the Kohn-Sham eigenstates analysis (Fig. 6.6) reveals a much more complex hybridization pattern in

the valence energy region. Similar to **1**, the e_g and t_{2g} manifolds can be identified around -1.8 and -3.4 eV. In addition, small set of states within the mid t_{2g}-e_g gap is observed at ~ -2.3 eV which is predominantly of π/π^* in character. The group of α-channel *d*-state manifolds for **5** is shifted downwards about 0.5 eV with respect to that in **1**, presumably due to the enhanced interaction with the $TCNE^{\bullet-}$ coordination environment. This coordination motif also leads to a more complex degeneracy lifting in the t_{2g} bands due to a further distortion of the O_h symmetry with respect to that in **1**. These majority spin bands in the -(4.0–0.4 eV) region again are primarily Mn 3d-derived, with a hybridization similar to that observed in **1**, but with less significant ligand engagement in the lower energy t_{2g} portion.

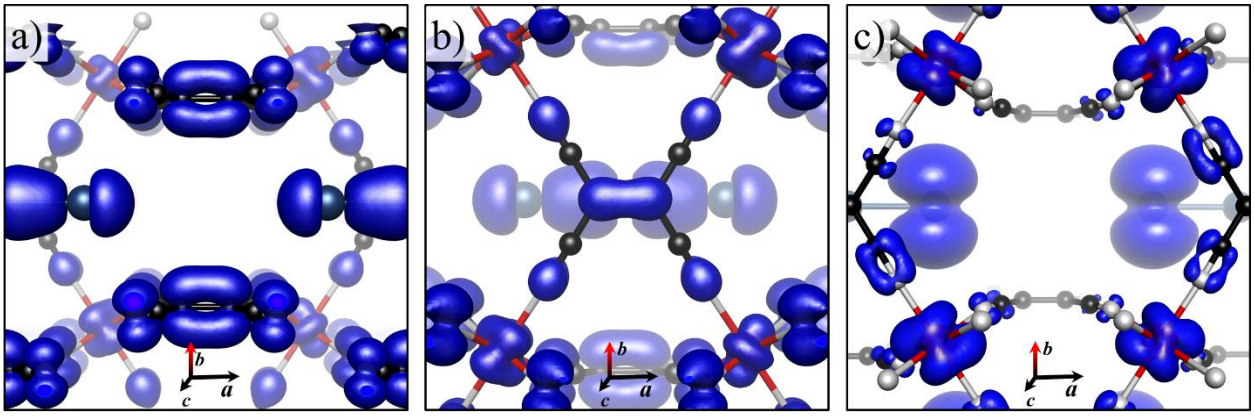

Figure 6.5. The representative fragments of α-spin eigenstates for **5** in -(3.6–3.2 eV) region with Mn 3d-π equatorial (a) and apical (b) hybridization; Mn 3d-π hybrids with predominantly metal and anion I_3 components with a small π electron density contribution from apical TCNE nitrile groups (c).

Typical eigenstates of this manifold are visualized in Fig. 6.6a-h. Similar to **1**, the states display a mostly 3d-π type hybridization, with orbital localization on both apically and equatorially coordinated TCNE nitrile groups. Within these bands, a general trend of slight degeneracy lifting is noted, i.e. the hybrids with π density localization primarily on the equatorial $Mn^{II}(\mu_4\text{-}TCNE^{\bullet-})$ layers reveal themselves at lower-energy components (Fig. 6.5a) compared to those in which π electron density is found more intensely on axial TCNE (Fig. 6.5b). The

highest-energy levels are demonstrated the hybrids with predominantly metal and anion I_3 components with a slight admixture of π density localization primarily on the apical TCNE nitrile groups (Fig 6.5c). In contrast to the **1** complex, no Mn 3d-π^* hybridized states were found in the t_{2g}-derived bands.

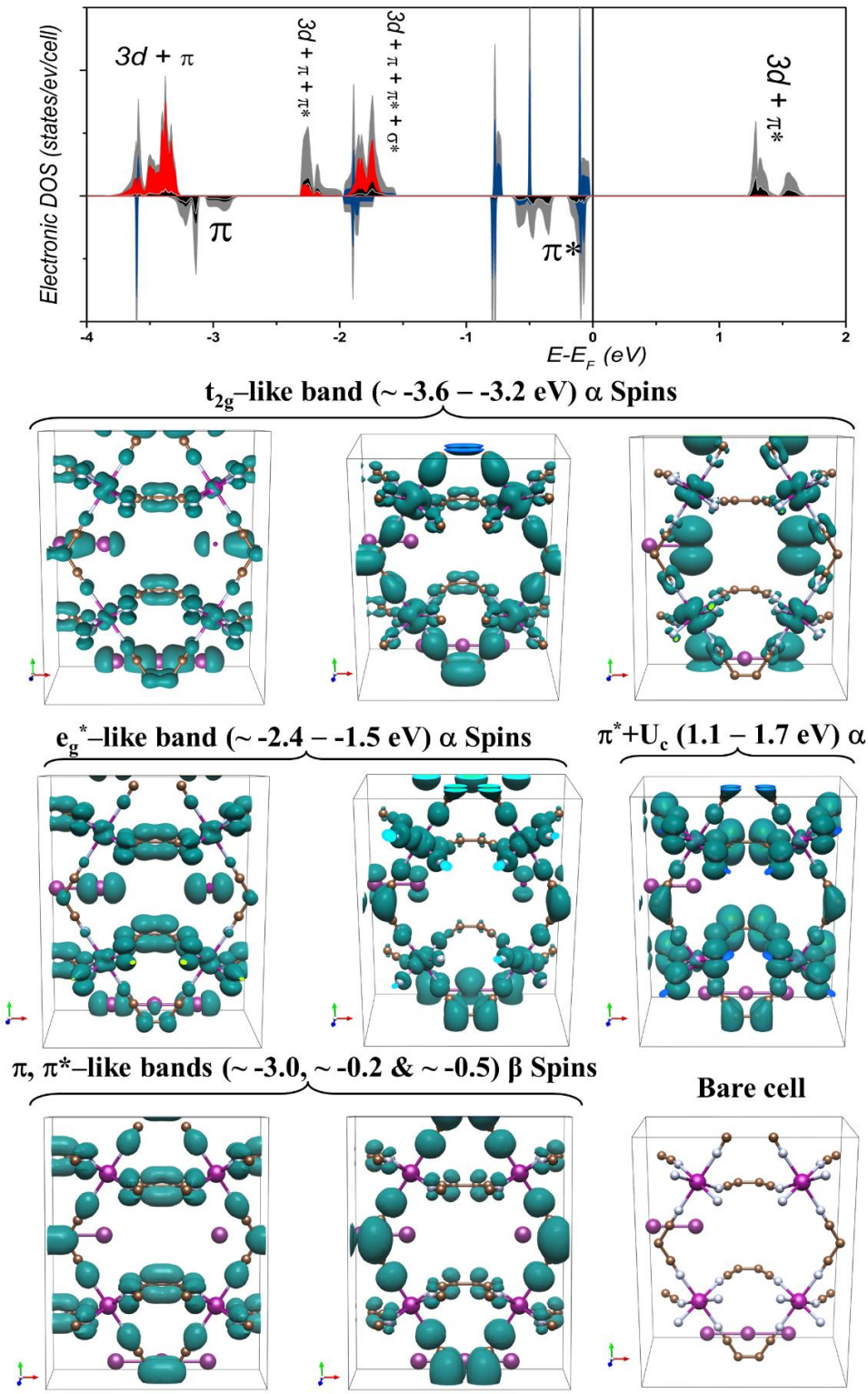

Figure 6.6. a-i. Orbitally projected DOS and representative eigenstates for **5**. (DOS: C – black, N – grey, Mn – red, I – dark teal, total – dark grey; Scheme: C – brown, N – gray, Mn – pink, I – purple).

In the region of -(2.5–1.5) two sub-bands are computed, again similar in structure and composition to those found in the decomposed DOS of **1**. Visualization of these levels reveals that the majority spin states appearing at ~-2.4 eV consist primarily of the 3d-π hybrids with relatively small 3d-π^* component, as illustrated in Fig. 6.6d-e. The former illustrates the eigenstates exhibiting the 3d-π type hybridization with mostly equatorial TCNEs, whereas the latter the 3d-π^* hybridization with the axial TCNE ligands. The high-energy Mn-3d e_g derived manifold centered near -1.8 eV spreads over broader energy range than that in **1** and exhibits a more complex mixing of Mn[TCNE] states. States in this cluster are composed of a few 3d-π derived hybrids, while the majority are of the 3d-π^* type. These latter states are differentiated from the lower energy lying 3d-π^* hybrids since the π^* character is noted in both TCNE coordination planes, with different ligand orbital contribution in the equatorial and apical planes.

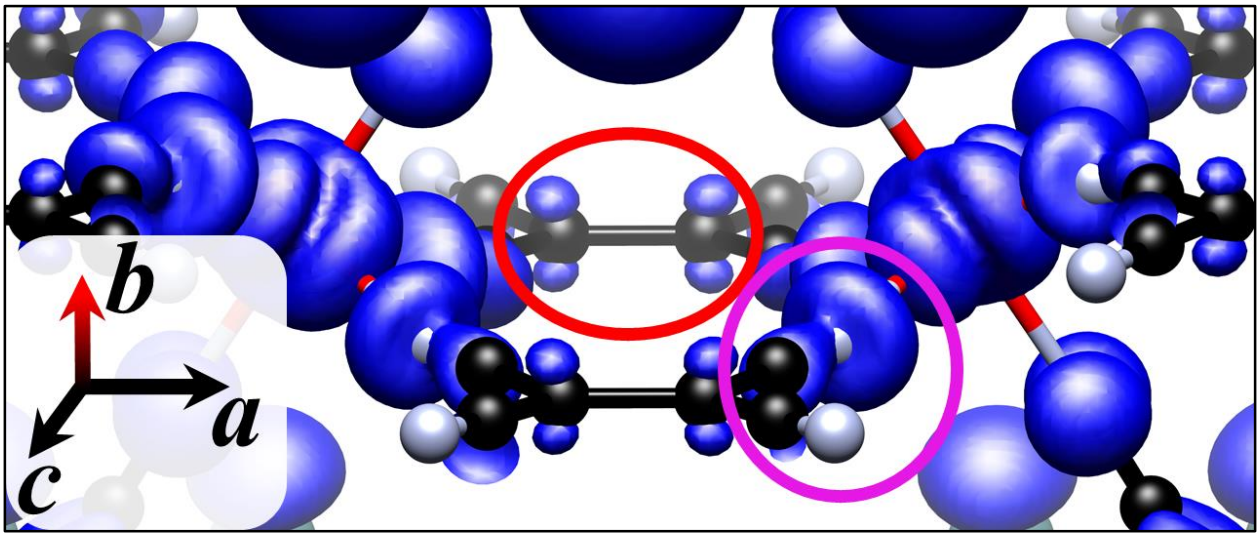

Figure 6.7. Illustration of lone-pair σ-type orbital with minor π^* hybridization in the ***a-c*** plane of **5**.

Interestingly, a slight mixing of the lone-pair σ-type orbitals of nitrile groups (Fig. 6.7, magenta circle) with a π^* density on the central carbons of equatorial TCNE ligands (Fig. 6.7, red circle) is found for many states in this band. It should be noted that a similar very weak

hybridization between MeCN lone-pair σ-type and the equatorial TCNE ligands π* orbitals was observed for the states in e_g-like band of compound **1** (cf. Fig. 6.4c and Fig. 6.7). In contrast, analogous albeit much stronger σ-π orbitals mixing were found for the 3d-π* hybrids involving the apically coordinated TCNE ligands (vide infra).

Two groups of bands are revealed in the β-spin channel of the (quasi) valence region of **5**, i.e. the multicomponent π character bands between -3.2 and -2.8 eV and π^* bands near -0.5 eV (both derived from the TCNE ligand), as is shown in Fig. 6.6 g-h, respectively. Similar to **1**, these β-spin π and π^* levels yield no observable hybridization with the 3d metal orbital density, in contrast to the π^*+U group of unoccupied bands that are revealed in the α-spin channel near +1.4 eV. The broadening of π, π* and π^*+U bands in the β-spin channel most probably occurs due to the presence of crystallographically inequivalent TCNE moieties in the unit cell.
The direct pair wise comparison of similar eigenstates consisting of characteristic orbitals involved in magnetic interaction helps rationalize the J values captured from the broken-symmetry analysis of **1** and **5** magnets. The typical 3d-π^* hybrid states responsible for the direct-exchange mechanism are shown in Fig. 6.8.

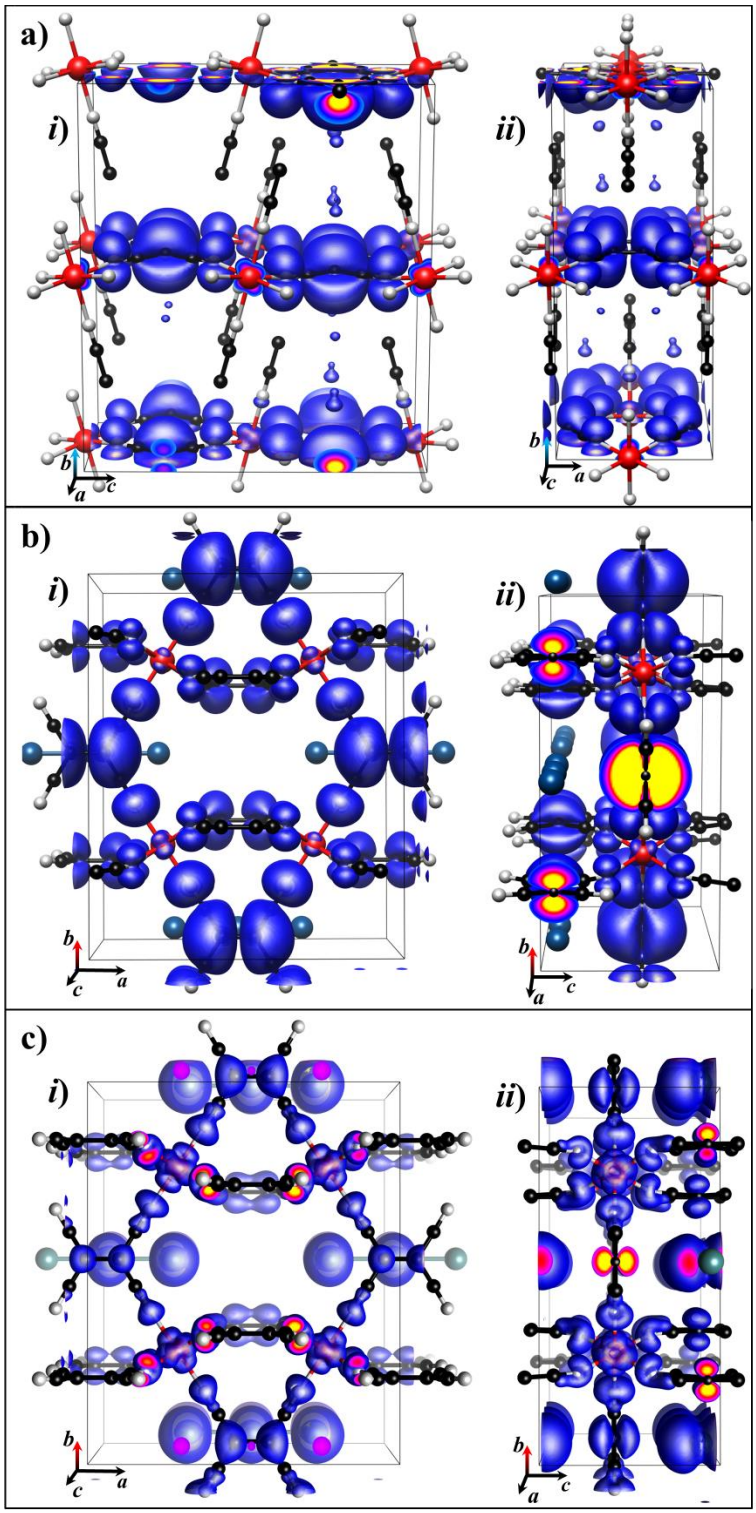

Figure 6.8. The 3d-π* hybrid states involved in the direct-exchange mechanism in **1** (a) and **5** (b, c) magnets; standard views (i) and cells rotated 90º in the ac plane (ii) are shown.

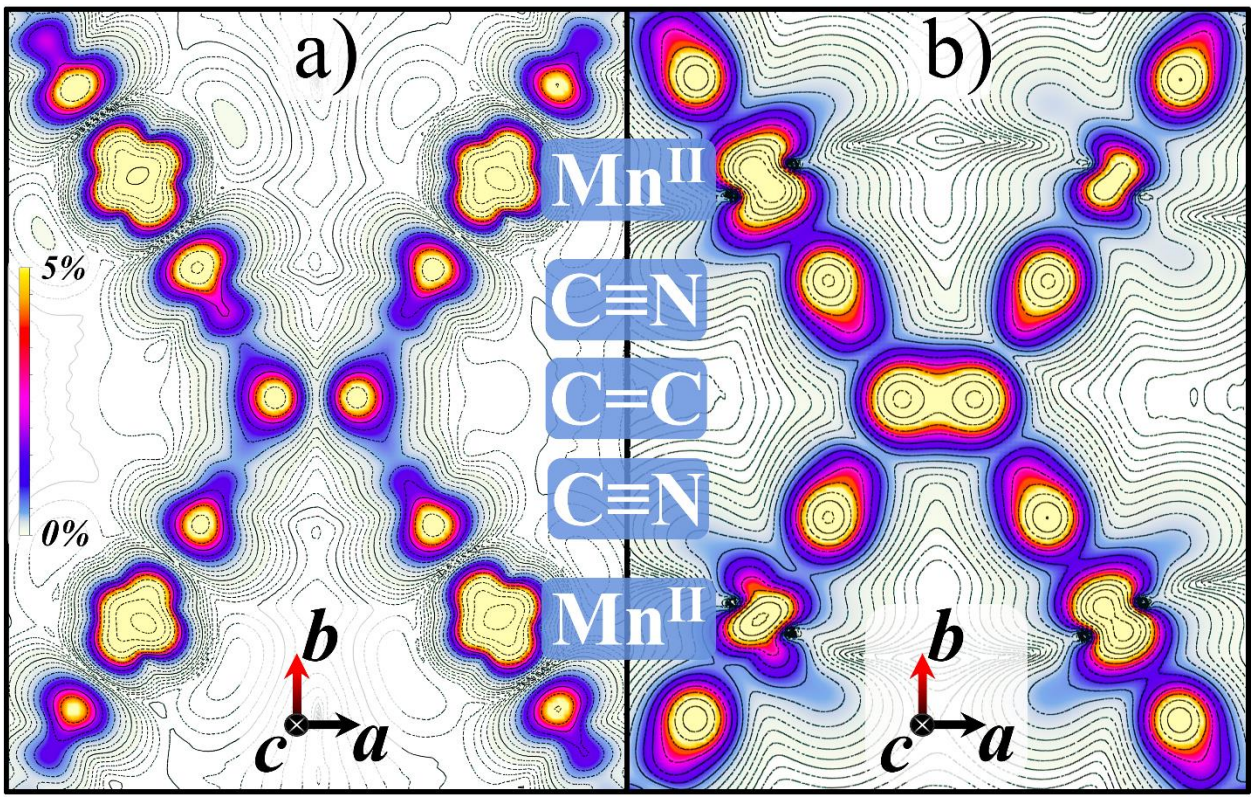

Figure 6.9. Direct comparison of lone-pair hybridized 3d-π^* (a) and 3d-π (b) orbitals occurring in the ***a-b*** (apical) plane of complex **5**. The spin densities from the $Mn^{II}(\mu_4\text{-}TCNE^{\bullet-})$ structural fragments are mapped to the plane. Color values saturate at 5% of the maximal electron density values found in the plane. Contour lines are a guide to the eye.

Using the Ising spin Hamitonian solutions, a modest exchange anisotropy was calculated in the apical and equatorial magnetic couplings in complex **5**, J_{ap}/J'_{eq} ~ 0.84, in contrast to the expected large anisotropy due to a substantial difference in the Mn−N≡C angles governing the 3d-π* orbital overlap. As it was mentioned above, the $Mn^{II}(\mu_4\text{-}TCNE^{\bullet-})$ layers in the ***a-b*** (apical) plane of **5** magnet possess 3d-π^* hybrid states in which the π* component consists of a lobe shaped density localized of TCNE nitrile groups, best illustrated in Fig. 6.8c. These remarkable eigenstates clearly lack the strong angular overlap dependence with Mn^{II} typical of the more characteristic TCNE-π^* states (Fig. 6.8a-b) in the equatorial ***a-c*** crystallographic direction. This orbital contrasts strongly with the 3d-π hybridized states also occurring in the ***a-b*** plane (Fig. 6.9). Thus, despite a possessing nearly linear Mn−N≡C angle, a strong direct exchange

interaction can be facilitated in the apical $Mn^{II}(\mu_4\text{-}TCNE^{\bullet-})$ layer. Notably, while very few 3d-π^* eigenstates possessing the lone-pair lobes are observed in the equatorial plane, they may also contribute to a J'_{eq} value enhancement along with the equatorial layer warping. In contrast, for complex **1** the lack of both significant $Mn^{II}(\mu_4\text{-}TCNE^{\bullet-})$ warping and TCNE lone pair-π^* hybridization explains the relatively low magnetic coupling constant found from the DFT analysis.

A detailed study of the spin/electronic DOS peculiarities revealed a modest ligand-to-metal charge transfer and spin-polarization of the diamagnetic α-spin TCNE π states hybridized with the Mn 3d (Fig. 6.10 a-b.).

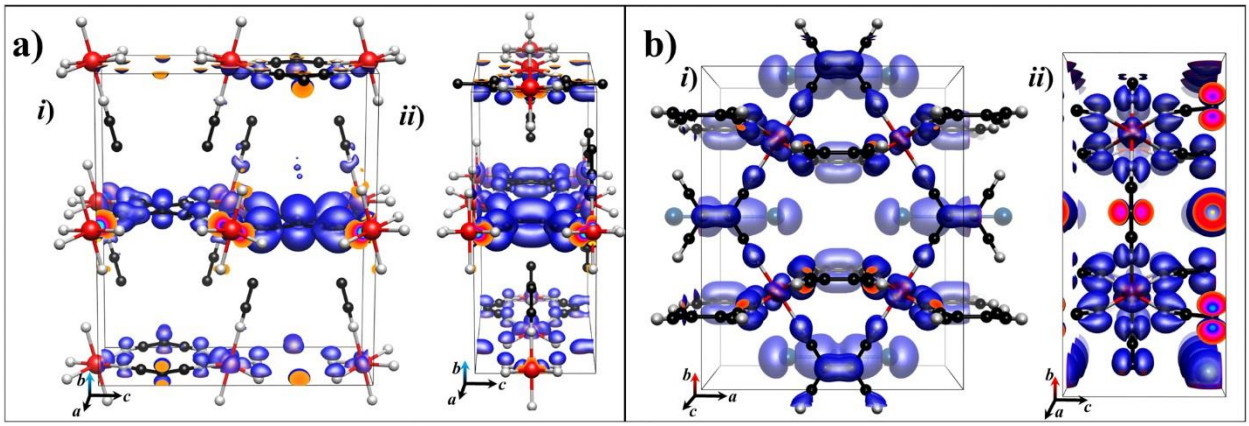

Figure 6.10. The Mn 3d-π hybrid states involved **1** (c) and **5** (d) magnets; standard views (i) and cells rotated 90º in the ***a-c*** plane (ii) are shown.

Revealing these hybrid states in DOSs of both **1** and **5** complexes suggests a more complex magnetic exchange mechanism than traditiaonlly thought for M[TCNE] MBMs. Specifically, analysis of DOS has revealed that Mn 3d-π hybrid states similar to those shown in Fig. 6.10 dominate within the energy range of t_{2g}-derived manifold in both materials. Albeit some Mn 3d-π* character hybrids have been also found in this region, but only for complex **1**. Nevertheless, the number of α-spin eigenstates with 3d-π* hybridization character is small, and

they are less representative in the overall metal-ligand hybridization picture. The filling of e_g orbitals in Mn^{II} caused a substantial stabilization of t_{2g} orbitals and increased t_{2g}-π^* derived orbital separation to ~3 eV for both **1** and **5** magnets thus making the Mn t_{2g}-π^* derived orbital coupling less efficient. Conversely, energetically the position of Mn t_{2g}- and π-derived orbitals is very close. Experimentally the energy overlapping of 3d metal and π TCNE orbitals was confirmed by XPS studies of Fe[TCNE] magnet [94]. It should be noted that both the π^* singly occupied molecular orbital and the lower-energy doubly occupied π orbital of $TCNE^{\bullet-}$ are symmetry wise adapted to overlap with the metal t_{2g} states in a traditional ligand-field π bonding scheme. Following Ruiz [211], a spin-polarization of diamagnetic π-bonding states should be expected due to the α-spin density shift toward the Mn^{II} ion, which in fact is clearly observed in DOS of both complexes (Fig. 6.2, -3 eV region) as discussed above. Recently, a strong spin-polarization of π-orbitals in a limited energy region was shown to exist in the isocyclic organic adsorbates in close contact (~2.5 Å) with a ferromagnetic substrate [212]. It was shown that the spin-polarization effect can significantly modify the spin density near the Fermi-edge via formation of π-d hybridized states in the α-spin channel. Spin-resolved local density of states for organic molecules (e.g. benzene) demonstrated close similarity with the behavior observed in the simulated DOS of **1** and **5** complexes in the t_{2g}-like region thus supporting the proposed metal-ligand hybridization mechanism. This mechanism could potentially introduce a ferromagnetic interaction between the α-spin polarized Mn 3d- and TCNE π-orbital derived states effectively weakening the main kinetic exchange coupling due to 3d-π^* direct exchange coupling. The critical ordering temperatures calculated above from the broken symmetry configurations of the nearest-neighbor Hamiltonians above do not account for these additional exchange interactions

though a diamagnetic ligand, potentially explaining the significant deviation from experimental values.

The above room temperature T_c of $V^{II}[TCNE]_x$ (x~2) magnet can be rationalized within the proposed conceptual framework. In this material, the V^{II} spins are in d^3 state and e_g states are unoccupied, in contrast to d^5 state in the high spin Mn^{II}. This electron configuration leads to a significantly reduced t_{2g}-π^* states energy separation (<1 eV [91-93]) facilitating very strong direct-exchange between the t_{2g}-π^* spins. Due to a relatively large t_{2g}-π orbital energy separation, only a weak interaction between t_{2g}-π orbitals is expected which possibly minimizes the detrimental effect of FM coupling on T_c via a strong 3d-π hybridization.

6.4. Conclusions

Using the crystal structures for the recently characterized 2D- and 3D- coordinated molecule-based magnets $[Mn^{II}(TCNE)(NCMe)_2]SbF_6$ (**1**) and $[Mn^{II}(TCNE)_{1.5}](I_3)_{0.5}$ (**5**), a comprehensive hybrid density-functional modeling investigation of the electronic and magnetic structures was performed. In accord with the experiment, the simulated ground-state magnetic configurations revealed by effective spin-density isosurfaces confirmed the expected ferrimagnetic 3d-π^* spin ordering in both structures. Low-lying magnetic excitations were simulated in accord with a broken-symmetry Ising Hamiltonian, and nearest-neighbor magnetic exchange constants J were calculated. Our simulations predicted a strengthening of the antiferromagnetic exchange interaction in **5**, presumably due to i) increased dimensionality of Mn 3d and TCNE π^* spin coupling and ii) more pronounced TCNE layer warping than in **1**, favoring enhanced spin-orbital overlap. The natures of three-dimensonal coupling and enhanced J-values were rationalized through identification of a unique lone-pair hybridized π^* state found

predominantly in **5**. These results explain the significant T_c increase in the **5** complex relative to its structurally related counterpart **1** and demonstrates the crucial role of realistic structural models in identifying bonding, hybridization, and spin-coupling motifs in M[TCNE] MBMs.

Computational modeling also unexpectedly revealed a strong spin-polarized 3d-π-type hybridization in both materials' valence d-orbital states, in addition to the expected 3d-π^* ones. It is suggested that this hybridization provides a spin-polarization type Mn^{II}[TCNE] (3d-π) interaction through the diamagnetic TCNE π orbitals, which may compete with the direct-exchange mode (3d-π^*), thus diminishing the direct metal-ligand spin coupling strength. This interaction mode was not predicted in previous and methodologically similar DFT modeling studies of hypothetical $V^{II}[TCNE]_2$ structures, and illustrates the nature of the complex electron-exchange landscape in higher-series transition metal M[TCNE] complexes.

7. CONCLUSIONS

In this dissertation, the primary goal was the realization poly-crystalline molecule-based magnetic solids within the M^{II}[TCNE] family (M^{II} = 3d transition metal) whose chemical composition and structural properties may be modified by simple chemical means. A rational synthetic approach achieving this goal would allow this class of solids to act as a model material system, affording a more rigorous exploration of composition- and structure-function relationships. These relationships were targeted as a means to better understand the complex interplay between magnetic exchange interactions, charge transfer of magnetic spins, and anisotropy or orbital filling as a function of chemical and structural factors in a series of magnetic insulators (as outlined in Chapter 2). This fundamental goal was attained by utilizing a new chemical metathesis route, which bypasses the previous and widely used synthetic scheme where the necessary chemical reduction of the organic TCNE building blocks occurs by 3d-series transition metals (Fe or V) in solution or vapor phases. The new synthetic route produced a significantly more general and advantageous chemical template: polycrystalline powders of $[M^{II}(TCNE)(NCMe)_2]X$ (M^{II} = 3d transition metal, X = inorganic anion, NCMe = acetonitrile ligand), where chemical properties may be modified and structures resolved. This synthetic approach was described in detail in the concluding portion of Chapter 2, and was leveraged to create the precursor and final magnetic materials extensively studied in Chapters 4-5 and in a portion of Chapter 6.

With the desired chemical route identified, the effect of 3d transition metal orbital filling in the $[M^{II}(TCNE)(NCMe)_2]SbF_6$ (M= 3d transition metal) material system was first studied. Here, a magnetometric and vibrational spectroscopic study (infrared and for the first time, Raman) was completed for M = Mn, Fe, Ni materials.

A new MBM $[Mn^{II}(TCNE)(NCME)_2]SbF_6$ was synthesized and crystal structure revealed by XRD analysis. It was shown to possess a quasi-2D structural motif of positively charged $(MeCN)_2$-$Mn^{II}(\mu_4$-$TCNE^{\bullet-})$ slabs with SbF_6 anions trapped between layers. XRD patterns of the Fe-derived species suggest it to be isostructural. Raman spectroscopic analysis revealed a quantitative linear correlation between the $\nu_{C=C}$ (a_g) frequency of the TCNE ligand and its formal charge Z (the spin density on the π^* orbital), affording characterization of both the direction and degree of charge transfer in $[M^{II}(TCNE)(NCMe)_2]SbF_6$ (M = Mn, Fe, Ni) molecular magnets. It was found that in all cases ~20% of the π^* electron ligand spin density is transferred to the metal as revealed by the Raman analysis. Magnetometry revealed the critical magnetic ordering temperatures to be 75 K (Mn), 90 K (Fe), and 30 K (Ni). The lack of significant correlation between the totally symmetric $\nu_{C=C}$ Raman frequencies and widely varying critical ordering temperatures T_c in the above materials suggests a magnetocrystalline anisotropy, and perhaps not the extent of charge transfer, most significantly influences the magnetic properties within the 2D $(MeCN)_2$-$M^{II}(\mu_4$-$TCNE^{\bullet-})$ layers. Finally, the $[M^{II}(TCNE)(NCMe)_2]SbF_6$ magnet was shown to possess an unusual frustrated magnetic transition with a weak bifurcation in the FC/ZFC measurement, in contrast to the Fe^{II}- and Ni^{II}-based magnets. This transition, in addition to a strong frequency-dependent dynamic susceptibility near T_c, suggested a disordered or "glassy" magnetic transition due either to impurity or an intrinsically frustrated spin ground state.

With a reproducible route to highly crystalline 2D MBMs identified, the dependence of magnetic properties upon lattice parameter modulation was investigated within the crystalline $[Mn^{II}(TCNE)(NCMe)_2]X$ (X = PF_6, AsF_6, SbF_6) material system. This task was targeted to examine the role of interlayer magnetic dipolar coupling in the 2D magnets. Anion size variation

from R(Å) = 3.02 (PF_6^-), 3.17 (AsF_6^-), 3.31 (SbF_6^-), introduced an expansion of ~2.8% in the $(MeCN)_2$-$Mn^{II}(\mu_4$-$TCNE^{\bullet-})$ interlayer distances upon $PF_6^- \rightarrow SbF_6^-$ substitution via chemical synthesis. If present, a T_c suppression of up to ~8.5% was expected concomitant with the lattice expansion due to the dipolar coupling relation $T_c \propto H_{dip} \propto 1/r^3_{i,j}$. Negligible shifts in T_c measured by static and dynamic magnetic susceptibility proved that interlayer dipolar coupling does not contribute to the magnetic ordering or critical phenomena in this material class. In addition, a unique re-entrant spin-glass state was identified through dynamic susceptibility measurements and thoroughly characterized. Due to the crystalline material quality, impurity-driven disorder in the spin dynamics was ruled out. Thus, this material system represents a unique example of a relatively simple polycrystalline organometallic solid possessing a two-dimensional magnetic lattice exhibiting both ordered and glassy magnetic transitions, likely due to the small single-ion anisotropy within the $S = 5/2$ Mn^{II} anion.

Finally, a comprehensive hybrid density-functional modeling investigation of electronic and magnetic structures was performed using the XRD-resolved crystal structures for the structurally related 2D- and 3D- coordinated molecule-based magnets $[Mn^{II}(TCNE)(MeCN)_2]SbF_6$ (T_c ~ 70 K) and $[Mn^{II}(TCNE)_{1.5}](I_3)_{0.5}$ (T_c ~ 170 K) respectively. Magnetic excitations were simulated in accord with a broken-symmetry Ising Hamiltonian, and nearest-neighbor magnetic exchange coupling constants between Mn^{II} (3d) and $TCNE^{\bullet-}$ (π^*) spins were calculated in all crystallographic directions for both materials. The simulations predicted a strengthening of the antiferromagnetic *direct exchange* magnetic coupling in the 3D material, in accord with experiment. The magnetic coupling strength increases within individual $Mn^{II}(\mu_4$-$TCNE^{\bullet-})$ planes of $[Mn^{II}(TCNE)_{1.5}](I_3)_{0.5}$ were rationalized on the basis of unique and unexpected 3d-π^* spin-orbital hybridization only observed in this fully 3D-networked structure.

Furthermore, a new electronic *superexchange* pathway containing significant 3d-π orbital contributions was identified in both studied materials, suggesting a more complex magnetic coupling landscape than previously thought for M^{II}[TCNE] molecule-based magnets. The 3d-π hybridization is postulated to arise through energetic stabilization of the 3d e_g*/t_{2g} manifold by occupation of the e_g symmetry orbitals, as is the case for high-spin Mn^{II}-derived magnets. This hybridization mode suggests that through-TCNE *superexchange* similar to the M(3d)−O(π)−M(3d) (M = transition metal, O = oxygen) superexchange in transition metal oxides may particpate in stabilizing magnetic order in higher-series transition metal M^{II}[TCNE] complexes. This is in contrast to the widely used, purely 3d-π* direct exchange model derived from experimental saturation studies. Collectively, these findings illustrate the roles that both dimensionality and transition metal identity play in facilitating the exceptional room-temperature magnetic ordering of the the $V^{II}[TCNE]_x$ (x ~ 2) complex. In V^{II} magnets, the 3d e_g* orbitals are unoccupied, and may suppress the formation of through-TCNE superexchange observed in Mn^{II}[TCNE] materials. The higher energy t_{2g}^3 states of V^{II} should instead provide strong overlap with the higher-energy π* state of $TCNE^{\bullet-}$, potentially enhanced by $TCNE^{\bullet-}$ π*-σ hybridized states donating spin directly through the chemical bond (similar to those observed in $[Mn^{II}(TCNE)_{1.5}](I_3)_{0.5}$), thus increasing significantly the effective magnetic overlap and T_c.

8. REFERENCES

[1] S. Fusil, V. Garcia, A. Barthelemy, M. Bibes, in: D.R. Clarke (Ed.), Annual Review of Materials Research, Vol 44, Annual Reviews, Palo Alto, 2014, p. 91.

[2] S.D. Bader, S.S.P. Parkin, in: J.S. Langer (Ed.), Annual Review of Condensed Matter Physics, Vol. 1, Annual Reviews, Palo Alto, 2010, p. 71.

[3] F. Pulizzi, Nature Materials 11 (2012) 367.

[4] I. Žutić, J. Fabian, S. Das Sarma, Reviews of Modern Physics 76 (2004) 323.

[5] B. Lojek, History of Semiconductor Engineering, Springer Berlin Heidelberg, 2007.

[6] D.C. Brock, G.E. Moore, Understanding Moore's Law: Four Decades of Innovation, Chemical Heritage Foundation, 2006.

[7] S.I. Ravelo Arias, D. Ramírez Muñoz, J. Sánchez Moreno, S. Cardoso, R. Ferreira, P.J. Peixeiro de Freitas, Sensors 13 (2013) 17516.

[8] I. Appelbaum, B. Huang, D.J. Monsma, Nature 447 (2007) 295.

[9] R. Jansen, S.P. Dash, S. Sharma, B.C. Min, Semiconductor Science and Technology 27 (2012) 083001.

[10] R. Jansen, Nature Materials 11 (2012) 400.

[11] K. Sato, E. Saitoh, A. Willoughby, P. Capper, S. Kasap, Spintronics for Next Generation Innovative Devices, Wiley, 2015.

[12] S.A. Wolf, D.D. Awschalom, R.A. Buhrman, J.M. Daughton, S. von Molnar, M.L. Roukes, A.Y. Chtchelkanova, D.M. Treger, Science 294 (2001) 1488.

[13] D.R. Talham, M.W. Meisel, Chemical Society Reviews 40 (2011) 3356.

[14] A. Fert, H. Jaffrès, Physical Review B 64 (2001) 184420.

[15] H.-K. Jeong, A. Caruso, C.N. Borca, Lecure Notes in Physics 676 (2005) 221.

[16] C.N. Borca, D. Ristoiu, H.K. Jeong, T. Komesu, A.N. Caruso, J. Pierre, L. Ranno, J.P. Nozieres, P.A. Dowben, Journal of Physics: Condensed Matter 19 (2007) 315211.

[17] S. Pramanik, C.G. Stefanita, S. Bandyopadhyay, Journal of Nanoscience and Nanotechnology 6 (2006) 1973.

[18] S. Sanvito, A.R. Rocha, Journal of Computational and Theoretical Nanoscience 3 (2006) 624.

[19] G. Szulczewski, S. Sanvito, M. Coey, Nature Materials 8 (2009) 693.

[20] V.A. Dediu, L.E. Hueso, I. Bergenti, C. Taliani, Nature Materials 8 (2009) 707.

[21] L.E. Hueso, J.M. Pruneda, V. Ferrari, G. Burnell, J.P. Valdes-Herrera, B.D. Simons, P.B. Littlewood, E. Artacho, A. Fert, N.D. Mathur, Nature 445 (2007) 410.

[22] T.S. Santos, J.S. Lee, P. Migdal, I.C. Lekshmi, B. Satpati, J.S. Moodera, Physical Review Letters 98 (2007) 016601.

[23] J.H. Shim, K.V. Raman, Y.J. Park, T.S. Santos, G.X. Miao, B. Satpati, J.S. Moodera, Physical Review Letters 100 (2008) 226603.

[24] N. Tombros, C. Jozsa, M. Popinciuc, H.T. Jonkman, B.J. van Wees, Nature 448 (2007) 571.

[25] Z.H. Xiong, D. Wu, Z.V. Vardeny, J. Shi, Nature 427 (2004) 821.

[26] J.-W. Yoo, H.W. Jang, V.N. Prigodin, C. Kao, C.B. Eom, A.J. Epstein, Physical Review B 80 (2009) 205207.

[27] J.M. Manriquez, G.T. Yee, R.S. McLean, A.J. Epstein, J.S. Miller, Science 252 (1991) 1415.

[28] V.N. Prigodin, N.P. Raju, K.I. Pokhodnya, J.S. Miller, A.J. Epstein, Advanced Materials 14 (2002) 1230.

[29] J.-W. Yoo, C.-Y. Chen, H.W. Jang, C.W. Bark, V.N. Prigodin, C.B. Eom, A.J. Epstein, Nature Materials 9 (2010) 638.

[30] K.I. Pokhodnya, A.J. Epstein, J.S. Miller, Advanced Materials 12 (2000) 410.

[31] J.S. Miller, K.I. Pokhodnya, Low Temperature Chemical Vapor Deposition Of Vanadium Tetracyanoethylene Thin Film Magnets. University of Utah Research Foundation, USA; Ohio State University Research Foundation. 2001, p. 29.

[32] B. Li, C.Y. Kao, J.W. Yoo, V.N. Prigodin, A.J. Epstein, Advanced Materials 23 (2011) 3382.

[33] L. Fang, K.D. Bozdag, C.Y. Chen, P.A. Truitt, A.J. Epstein, E. Johnston-Halperin, Physical Review Letters 106 (2011) 156602.

[34] C. Kittel, Introduction to Solid State Physics, p. 648-656, Wiley, 2004.

[35] N.W. Ashcroft, N.D. Mermin, Solid State Physics, Holt, Rinehart and Winston, 1976.

[36] G.A. Bain, J.F. Berry, Journal of Chemical Education 85 (2008) 532.

[37] F. Bitter, Physical Review 33 (1929) 389.

[38] J.M.D. Coey, Magnetism and Magnetic Materials. Cambridge University Press, Cambridge, 2011.

[39] J.M.D. Coey, Magnetism and Magnetic Materials, Cambridge University Press, 2010.

[40] G.F. Dionne, Magnetic Oxides, Springer US, 2010, p. 211.

[41] P. Weiss, Journal of Theoretical and Applied Physics 6 (1907) 661.

[42] S. Chatterjee, Reson 9 (2004) 57.

[43] J.S. Miller, Chemical Society Reviews 40 (2011) 3266.

[44] J.S. Miller, A.J. Epstein, Angewandte Chemie 106 (1994) 399.

[45] D. Khomskii, in: M. Ziese, M. Thornton (Eds.), Spin Electronics, Springer Berlin Heidelberg, 2001, p. 89.

[46] J.M.D. Coey, M. Viret, S. von Molnár, Advances in Physics 48 (1999) 167.

[47] J.S. Miller, D. Gatteschi, Chemical Society Reviews 40 (2011) 3065.

[48] P. Day, F. Herren, A. Ludi, H.U. Güdel, F. Hulliger, D. Givord, Helvetica Chimica Acta 63 (1980) 148.

[49] M. Verdaguer, G.S. Girolami, Magnetism: Molecules to Materials V, Wiley-VCH Verlag GmbH & Co. KGaA, 2005, p. 283.

[50] J.S. Miller, Materials Today 17 (2014) 224.

[51] H.U. Güdel, H. Stucki, A. Ludi, Inorganica Chimica Acta 7 (1973) 121.

[52] D. Babel, Comments on Inorganic Chemistry 5 (1986) 285.

[53] B.N. Figgis, E.S. Kucharski, M. Vrtis, Journal of the American Chemical Society 115 (1993) 176.

[54] F.H. Köhler, R. Lescouëzec, Angewandte Chemie International Edition 43 (2004) 2571.

[55] S.M. Holmes, G.S. Girolami, Journal of the American Chemical Society 121 (1999) 5593.

[56] L.G. Beauvais, J.R. Long, Journal of the American Chemical Society 124 (2002) 12096.

[57] W.R. Entley, G.S. Girolami, Inorganic Chemistry 33 (1994) 5165.

[58] W.R. Entley, C.R. Treadway, G.S. Girolami, Molecular Crystals and Liquid Crystals Science and Technology. Section A. Molecular Crystals and Liquid Crystals 273 (1995) 153.

[59] S. Ferlay, T. Mallah, R. Ouahes, P. Veillet, M. Verdaguer, Nature 378 (1995) 701.

[60] S. Ferlay, T. Mallah, R. Ouahès, P. Veillet, M. Verdaguer, Inorganic Chemistry 38 (1999) 229.

[61] D. Li, R. Clérac, O. Roubeau, E. Harté, C. Mathonière, R. Le Bris, S.M. Holmes, Journal of the American Chemical Society 130 (2008) 252.

[62] D.M. Pajerowski, M.J. Andrus, J.E. Gardner, E.S. Knowles, M.W. Meisel, D.R. Talham, Journal of the American Chemical Society 132 (2010) 4058.

[63] J.-D. Cafun, G. Champion, M.-A. Arrio, C.C. dit Moulin, A. Bleuzen, Journal of the American Chemical Society 132 (2010) 11552.

[64] D.M. Pajerowski, B. Ravel, C.H. Li, M.F. Dumont, D.R. Talham, Chemistry of Materials 26 (2014) 2586.

[65] C.R. Gros, M.K. Peprah, B.D. Hosterman, T.V. Brinzari, P.A. Quintero, M. Sendova, M.W. Meisel, D.R. Talham, Journal of the American Chemical Society 136 (2014) 9846.

[66] E.S. Koumousi, I.-R. Jeon, Q. Gao, P. Dechambenoit, D.N. Woodruff, P. Merzeau, L. Buisson, X. Jia, D. Li, F. Volatron, C. Mathonière, R. Clérac, Journal of the American Chemical Society 136 (2014) 15461.

[67] C. Gervais, M.-A. Languille, G. Moretti, S. Réguer, Langmuir 31 (2015) 8168.

[68] F.H. Köhler, O. Storcheva, Inorganic Chemistry 54 (2015) 6801.

[69] M. Presle, I. Maurin, F. Maroun, R. Cortès, L. Lu, R. Sayed Hassan, E. Larquet, J.-M. Guigner, E. Rivière, J.P. Wright, J.-P. Boilot, T. Gacoin, The Journal of Physical Chemistry C 118 (2014) 13186.

[70] D.M. Pajerowski, J.E. Gardner, F.A. Frye, M.J. Andrus, M.F. Dumont, E.S. Knowles, M.W. Meisel, D.R. Talham, Chemistry of Materials 23 (2011) 3045.

[71] M. Kivala, C. Boudon, J.-P. Gisselbrecht, B. Enko, P. Seiler, I.B. Müller, N. Langer, P.D. Jarowski, G. Gescheidt, F. Diederich, Chemistry – A European Journal 15 (2009) 4111.

[72] A. Zheludev, A. Grand, E. Ressouche, J. Schweizer, B.G. Morin, A.J. Epstein, D.A. Dixon, J.S. Miller, Journal of the American Chemical Society 116 (1994) 7243.

[73] A. Zheludev, A. Grand, E. Ressouche, J. Schweizer, B.G. Morin, A.J. Epstein, D.A. Dixon, J.S. Miller, Angewandte Chemie International Edition 33 (1994) 1397.

[74] J.S. Miller, J.C. Calabrese, H. Rommelmann, S.R. Chittipeddi, J.H. Zhang, W.M. Reiff, A.J. Epstein, Journal of the American Chemical Society 109 (1987) 769.

[75] J.S. Miller, Journal of Materials Chemistry 20 (2010) 1846.

[76] J.S. Miller, J.C. Calabrese, R.S. McLean, A.J. Epstein, Advanced Materials 4 (1992) 498.

[77] J.-H. Her, P.W. Stephens, J.D. Bagnato, J.S. Miller, The Journal of Physical Chemistry C 114 (2010) 20614.

[78] J.-H. Her, P.W. Stephens, J. Ribas-Ariño, J.J. Novoa, W.W. Shum, J.S. Miller, Inorganic Chemistry 48 (2009) 3296.

[79] J.H. Her, P.W. Stephens, K.I. Pokhodnya, M. Bonner, J.S. Miller, Angewandte Chemie 46 (2007) 1521.

[80] C.S. Olson, C.L. Heth, F.L. Alema, S.H. Lapidus, P.W. Stephens, K.I. Pokhodnya, Journal of Physics: Condensed Matter 25 (2013) 256004.

[81] K.I. Pokhodnya, M. Bonner, J.H. Her, P.W. Stephens, J.S. Miller, Journal of the American Chemical Society 128 (2006) 15592.

[82] C. Olson, C.L. Heth, S.H. Lapidus, P.W. Stephens, G.J. Halder, K. Pokhodnya, The Journal of Chemical Physics 135 (2011) 024503.

[83] K.I. Pokhodnya, M. Bonner, J.-H. Her, P.W. Stephens, J.S. Miller, Journal of the American Chemical Society 128 (2006) 15592.

[84] S.H. Lapidus, A.C. McConnell, P.W. Stephens, J.S. Miller, Chemical Communications 47 (2011) 7602.

[85] K.H. Stone, P.W. Stephens, A.C. McConnell, E. Shurdha, K.I. Pokhodnya, J.S. Miller, Advanced Materials 22 (2010) 2514.

[86] J.S. Miller, J.C. Calabrese, R.S. McLean, A.J. Epstein, Advanced Materials 4 (1992) 498.

[87] J. Ribas-Arino, J.J. Novoa, J.S. Miller, Journal of Materials Chemistry 16 (2006) 2600.

[88] C. Oprea, F. Cimpoesu, P. Panait, B. Frecuş, M. Ferbinteanu, M. Gîrţu, Theoretical Chemistry Accounts 129 (2011) 847.

[89] D. Haskel, Z. Islam, J. Lang, C. Kmety, G. Srajer, K.I. Pokhodnya, A.J. Epstein, J.S. Miller, Physical Review B 70 (2004) 054422/1.

[90] J.S. Miller, Polyhedron 28 (2009) 1596.

[91] C. Tengstedt, M.P. de Jong, A. Kanciurzewska, E. Carlegrim, M. Fahlman, Physical Review Letters 96 (2006) 057209.

[92] M.P. de Jong, C. Tengstedt, A. Kanciurzewska, E. Carlegrim, W.R. Salaneck, M. Fahlman, Physical Review B 75 (2007).

[93] J.B. Kortright, D.M. Lincoln, R.S. Edelstein, A.J. Epstein, Physical Review Letters 100 (2008).

[94] P. Bhatt, E. Carlegrim, A. Kanciurzewska, M.P. Jong, M. Fahlman, Applied Physics A 95 (2008) 131.

[95] J.S. Miller, A.J. Epstein, Chemical Communications (1998) 1319.

[96] J.S. Miller, D. Gatteschi, Chemical Society Reviews 40 (2011) 3065.

[97] K.I. Pokhodnya, V. Dokukin, J.S. Miller, Inorganic Chemistry 47 (2008) 2249.

[98] K.I. Pokhodnya, N. Petersen, J.S. Miller, Inorganic Chemistry 41 (2002) 1996.

[99] J.S. Miller, A.J. Epstein, W.M. Reiff, Chemical Reviews 88 (1988) 201.

[100] A.L. Tchougreeff, R. Hoffmann, The Journal of Physical Chemistry 97 (1993) 350.

[101] S. Erdin, Physics Letters A 372 (2008) 493.

[102] Y. Jean, Molecular Orbitals of Transition Metal Complexes, OUP Oxford, p. 43, 2005.

[103] K. Capelle, A Bird's-Eye View of Density-Functional Theory, Departamento de Física e Informática, Instituto de Física de São Carlos-USP, 2004.

[104] V.E. Van Doren, C. Van Alsenoy, P. Geerlings, Density Functional Theory and Its Application to Materials: Antwerp, Belgium, 8-10 June 2000, American Institute of Physics, 2001.

[105] H. Jiang, R.I. Gomez-Abal, P. Rinke, M. Scheffler, Physical Review B 82 (2010) 045108.

[106] C. Kollmar, M. Couty, O. Kahn, Journal of the American Chemical Society 113 (1991) 7994.

[107] J.L. Arthur, S.H. Lapidus, P.W. Stephens, J.S. Miller, Science China Chemistry 55 (2012) 987.

[108] K. Koizumi, M. Shoji, Y. Kitagawa, T. Taniguchi, T. Kawakami, M. Okumura, K. Yamaguchi, Polyhedron 24 (2005) 2720.

[109] F. Cimpoesu, M. Ferbinteanu, B. Frecuş, M.A. Gîrţu, Polyhedron 28 (2009) 2039.

[110] C. Oprea, F. Cimpoesu, P. Panait, B. Frecuş, M. Ferbinteanu, M. Gîrţu, Theoretical Chemistry Accounts 129 (2011) 847.

[111] C. Oprea, P. Panait, F. Cimpoesu, I. Humelnicu, M. Ferbinteanu, M. Gîrţu, Theoretical Chemistry Accounts 131 (2012) 1.

[112] A.N. Caruso, K.I. Pokhodnya, W.W. Shum, W.Y. Ching, B. Anderson, M.T. Bremer, E. Vescovo, P. Rulis, A.J. Epstein, J.S. Miller, Physical Review B 79 (2009).

[113] G.C. De Fusco, L. Pisani, B. Montanari, N.M. Harrison, Physical Review B 79 (2009) 085201.

[114] W.W. Shum, A.J. Epstein, J.S. Miller, Physical Review B 80 (2009) 064403.

[115] A.L. Tchougreeff, R. Dronskowski, Journal Of Computational Chemistry 29 (2008) 2220.

[116] G.C. De Fusco, B. Montanari, N.M. Harrison, Physical Review B 82 (2010) 220404.

[117] A.N. Caruso, K.I. Pokhodnya, W.W. Shum, W.Y. Ching, B. Anderson, M.T. Bremer, E. Vescovo, P. Rulis, A.J. Epstein, J.S. Miller, Physical Review B 79 (2009) 195202/1.

[118] W.W. Shum, A.J. Epstein, J.S. Miller, Physical Review B 80 (2009) 064403/1.

[119] W. Sturhahn, Geophysical Research Letters 32 (2005) L12307.

[120] V.R.S. R. Dovesi, C. Roetti, R. Orlando, C. M. Zicovich-Wilson, F. Pascale, B. Civalleri, K. Doll, N. M. Harrison, I. J. Bush, P. D'Arco, and M. Llunell. CRYSTAL06 User's Manual (University of Torino, Torino, 2006).

[121] E. Lamouroux, E. Alric, H. Casellas, L. Valade, D. de Caro, M. Etienne, D. Gatteschi, Electrochemical Society Proceedings 2003-8 (2003) 1040.

[122] A. Zheludev, A. Grand, E. Ressouche, J. Schweizer, B.G. Morin, A.J. Epstein, D.A. Dixon, J.S. Miller, Journal of the American Chemical Society 116 (1994) 7243.

[123] K.I. Pokhodnya, M. Bonner, A.G. DiPasquale, A.L. Rheingold, J.S. Miller, Chemistry – A European Journal 14 (2008) 714.

[124] K. Nakamoto, Infrared and Raman Spectra of Inorganic and Coordination Compounds, Applications in Coordination, Organometallic, and Bioinorganic Chemistry, Wiley, 1997.

[125] J. Sulé-Suso, N.R. Forsyth, V. Untereiner, G.D. Sockalingum, Trends in Biotechnology 32 (2014) 254.

[126] K. Nakamoto, Infrared and Raman Spectra of Inorganic and Coordination Compounds, Theory and Applications in Inorganic Chemistry, Wiley, 1997.

[127] K. Nakamoto, p. 46.

[128] K. Nakamoto, p. 49.

[129] K. Nakamoto, p. 355.

[130] K. Nakamoto, p. 377.

[131] Introduction to FTIR Spectroscopy Newport, http://www.newport.com/Introduction-to-FTIR-Spectroscopy/405840/1033/content.aspx.

[132] P. Griffiths, Science 222 (1983) 297.

[133] R. Petry, M. Schmitt, J. Popp, ChemPhysChem 4 (2003) 14.

[134] J. Barbillat, P. Dhamelincourt, M. Delhaye, E. Da Silva, Journal of Raman Spectroscopy 25 (1994) 3.

[135] J.M.D. Coey, Magnetism and Magnetic Materials, Cambridge University Press, 2010, p. 362-363.

[136] A. Wold, K. Dwight, Solid State Chemistry: Synthesis, Structure, and Properties of Selected Oxides and Sulfides, Springer Netherlands, 2012, p. 51.

[137] A. Wold, p. 50.

[138] B.K. Tanner, Introduction to the Physics of Electrons in Solids, Cambridge University Press, 1995, p. 175.

[139] S. Maintz, B. Eck, R. Dronskowski, Computer Physics Communications 182 (2011) 1421.

[140] G. Kresse, D. Joubert, Physical Review B 59 (1999) 1758.

[141] W. Li, C.F.J. Walther, A. Kuc, T. Heine, Journal of Chemical Theory and Computation 9 (2013) 2950.

[142] C.J. Cramer, D.G. Truhlar, Physical Chemistry Chemical Physics 11 (2009) 10757.

[143] G.C. De Fusco, B. Montanari, N.M. Harrison, Physical Review B 82 (2010) 220404.

[144] G.C. De Fusco, L. Pisani, B. Montanari, N.M. Harrison, Physical Review B 79 (2009) 085201.

[145] S. Gangopadhyay, A.E. Masunov, S. Kilina, Journal of Physical Chemistry C 118 (2014) 20605.

[146] T.M. Henderson, A.F. Izmaylov, G.E. Scuseria, A. Savin, The Journal of Chemical Physics 127 (2007) 221103.

[147] P. Rivero, I.d.P.R. Moreira, F. Illas, G.E. Scuseria, The Journal of Chemical Physics 129 (2008) 184110.

[148] E. Ruiz, P. Alemany, S. Alvarez, J. Cano, Journal of the American Chemical Society 119 (1997) 1297.

[149] B. Chan, J.-W. Song, Y. Kawashima, K. Hirao, Journal of Computational Chemistry 36 (2015) 871.

[150] J. Heyd, G.E. Scuseria, M. Ernzerhof, The Journal of Chemical Physics 118 (2003) 8207.

[151] J.S. Miller, Angewandte Chemie 45 (2006) 2508.

[152] T.H.M. Vandenberg, A. Vanderavoird, Journal of Physics: Condensed Matter 1 (1989) 4047.

[153] J.J. Hinkel, J.P. Devlin, Journal of Chemical Physics 58 (1973) 4750.

[154] F. Markel, N.S. Ferris, I.R. Gould, A.B. Myers, Journal of the American Chemical Society 114 (1992) 6208.

[155] M. Meneghetti, C. Pecile, Journal of Chemical Physics 105 (1996) 397.

[156] B.H. Loo, Journal of Molecular Structure 661-662 (2003) 451.

[157] J.W. Yoo, V.N. Prigodin, W.W. Shum, K.I. Pokhodnya, J.S. Miller, A.J. Epstein, Physical Review Letters 101 (2008) 197206.

[158] S. Liu, M.T. Bremer, J. Lovaasen, A.N. Caruso, K. O'Neill, L. Simpson, P.A. Parilla, M.J. Heben, D.L. Schulz, Inorganic Chemistry 47 (2008) 1568.

[159] A. P. Hammersley, ESRF Internal Report, 1997; ESRF97HA02T; A. P. Hammersley, S. O Svensson, M. Hanfland, A. N. Fitch, D. Hausermann, High-Pressure Research 1996, 14, 235-248.

[160] A. Zheludev, A. Grand, E. Ressouche, J. Schweizer, B.G. Morin, A.J. Epstein, D.A. Dixon, J.S. Miller, Journal of the American Chemical Society 116 (1994) 7243.

[161] R. Rao, T. Sakuntala, S.K. Deb, R. Mukhopadhyay, Journal of Physics: Condensed Matter 17 (2005) 2633.

[162] The C=C axis is the z-axis, xz is the molecular plane

[163] J.S. Chappell, A.N. Bloch, W.A. Bryden, M. Maxfield, T.O. Poehler, D.O. Cowan, Journal of the American Chemical Society 103 (1981) 2442.

[164] J.C.T. Stires, E.J. McLaurin, C.P. Kubiak, Chemical Communications (2005) 3532.

[165] K. Nakamoto, Infrared and Raman Spectra of Inorganic and Coordination Compounds, 5th ed., Part B, Wiley, New York, 1997, p. 113.

[166] G.T. Yee, J.C. Calabrese, C. Vazquez, J.S. Miller, Inorganic Chemistry 32 (1993) 377.

[167] E.L. Pace, L.J. Noe, Journal of Chemical Physics 49 (1968) 5317.

[168] P. Bruno, Physical Review B 43 (1991) 6015.

[169] M. Drillon, P. Panissod, P. Rabu, J. Souletie, V. Ksenofontov, P. Gütlich, Physical Review B 65 (2002).

[170] A.A. Coelho, Journal of Applied Crystallography 33 (2000) 899.

[171] A.A. Coelho, Journal of Applied Crystallography 36 (2003) 86.

[172] K.H. Stone, P.W. Stephens, A.C. McConnell, E. Shurdha, K.I. Pokhodnya, J.S. Miller, Advanced Materials 22 (2010) 2514.

[173] Mydosh, J. A. Spin Glasses; Taylor & Francis: London, Washington, DC, 1993; (a) p. 66-69, (b) p. 93.

[174] M.F. Hansen, S. Mørup, Journal of Magnetism and Magnetic Materials 184 (1998) L262.

[175] N. Ru, C.L. Condron, G.Y. Margulis, K.Y. Shin, J. Laverock, S.B. Dugdale, M.F. Toney, I.R. Fisher, Physical Review B 77 (2008) 035114.

[176] A.E. Midgley, C. Olson, C.L. Heth, A.N. Caruso, M.B. Kruger, G.J. Halder, J.A. Schlueter, K. Pokhodnya, The Journal of Chemical Physics 138 (2013) 014701.

[177] M. Gabay, G. Toulouse, Physical Review Letters 47 (1981) 201.

[178] V.K. Anand, D.T. Adroja, A.D. Hillier, J. Taylor, G. André, Physical Review B 84 (2011) 064440/1.

[179] B. Maji, K.G. Suresh, A.K. Nigam, Journal of Physics: Condensed Matter 23 (2011) 506002.

[180] B. Saparov, S. Calder, B. Sipos, H. Cao, S. Chi, D.J. Singh, A.D. Christianson, M.D. Lumsden, A.S. Sefat, Physical Review B 84 (2011) 245132.

[181] S.J. Etzkorn, W. Hibbs, J.S. Miller, A.J. Epstein, Physical Review Letters 89 (2002) 207201.

[182] J. Souletie, J.L. Tholence, Physical Review B 32 (1985) 516.

[183] J. Dho, W.S. Kim, N.H. Hur, Physical Review Letters 89 (2002) 027202.

[184] D.N.H. Nam, R. Mathieu, P. Nordblad, N.V. Khiem, N.X. Phuc, Physical Review B 62 (2000) 8989.

[185] T. Sudyoadsuk, R. Suryanarayanan, P. Winotai, Journal of Physics: Condensed Matter 16 (2004) 3691.

[186] C.M. Wynn, M.A. Girtu, J. Zhang, J.S. Miller, A.J. Epstein, Physical Review B 58 (1998) 8508.

[187] M. Drillon, P. Panissod, Journal of Magnetism and Magnetic Materials 188 (1998) 93.

[188] H.G. Katzgraber, L.W. Lee, Physical Review B 71 (2005) 134404.

[189] I.A. Campbell, S. Senoussi, Philosophical Magazine Part B 65 (1992) 1267.

[190] A.K. Nayak, K.G. Suresh, A.K. Nigam, Journal of Physics: Condensed Matter 23 (2011) 416004.

[191] J.S. Miller, Journal of Materials Chemistry 20 (2010) 1846.

[192] J.S. Miller, Dalton transactions (2006) 2742.

[193] G. Kresse, J. Furthmüller, Phyical Review B 54 (1996) 11169.

[194] G. Kresse, J. Hafner, Phyical Review B 47 (1993) 558.

[195] G. Kresse, J. Hafner, Phyical Review B 49 (1994) 14251.

[196] C. Olson, C.L. Heth, S.H. Lapidus, P.W. Stephens, G.J. Halder, K. Pokhodnya, Journal of Chemical Physics 135 (2011) 024503/1.

[197] K.H. Stone, P.W. Stephens, A.C. McConnell, E. Shurdha, K.I. Pokhodnya, J.S. Miller, Advanced Materials 22 (2010) 2514.

[198] H.J. Monkhorst, J.D. Pack, Phyical Review B 13 (1976) 5188.

[199] P.E. Blöchl, O. Jepsen, O.K. Andersen, Phyical Review B 49 (1994) 16223.

[200] L. Noodleman, Journal of Chemical Physics 74 (1981) 5737.

[201] L. Noodleman, E.R. Davidson, Chemical Physics 109 (1986) 131.

[202] C.S. Olson, C.L. Heth, F.L. Alema, S.H. Lapidus, P.W. Stephens, K.I. Pokhodnya, Journal of Physics: Condensed Matter 25 (2013) 256004.

[203] C. Oprea, F. Cimpoesu, P. Panait, B. Frecuş, M. Ferbinteanu, M. Gîrţu, Theoretical Chemistry Accounts 129 (2011) 847.

[204] A.C. McConnell, R.S. Fishman, J.S. Miller, The Journal of Physical Chemistry C 116 (2012) 16154.

[205] C.S. Olson, C.L. Heth, F.L. Alema, S.H. Lapidus, P.W. Stephens, K.I. Pokhodnya, Journal of Physics: Condensed Matter 25 (2013) 256004.

[206] B. Frecus, C. Oprea, P. Panait, M. Ferbinteanu, F. Cimpoesu, M. Gîrţu, Theoretical Chemistry Accounts 133 (2014) 1.

[207] J.-H. Her, P.W. Stephens, J.D. Bagnato, J.S. Miller, The Journal of Physical Chemistry C 114 (2010) 20614.

[208] C.I. Oprea, F. Cimpoesu, P. Panait, B. Frecuş, M. Ferbinteanu, M.A. Gîrţu, Theoretical Chemistry Accounts 129 (2011) 847.

[209] J. Ribas-Ario, J.J. Novoa, J.S. Miller, Journal of Materials Chemistry 16 (2006) 2600.

[210] C. Tengstedt, M. Unge, M.P. de Jong, S. Stafström, W.R. Salaneck, M. Fahlman, Physical Review B 69 (2004).

[211] E. Ruiz, J. Cirera, S. Alvarez, Coordination Chemistry Reviews 249 (2005) 2649.

[212] N. Atodiresei, J. Brede, P. Lazić, V. Caciuc, G. Hoffmann, R. Wiesendanger, S. Blügel, Physical Review Letters 105 (2010) 066601.